Università degli Studi di Ferrara

DOTTORATO DI RICERCA IN
SCIENZE CHIMICHE

CICLO XXVII

COORDINATORE Prof. Bignozzi Carlo Alberto

Biophysical mechanisms of membrane perturbation and signal transduction produced by proteins and peptides

Settore Scientifico Disciplinare BIO/09

Dottorando	**Tutore**
Dott.ssa Fasoli Anna	Prof.ssa Rampi Maria Anita

Co-Tutore
Prof. Rispoli Giorgio

Anni 2012/2014

Preface

My primary research interest is focused on the field of cellular electrical activity, ranging from the ion channels that generates it, up to the study of intracellular processes regulating it, and new generation of drugs. For this purpose, during my Ph.D. I have learnt and improved different cutting-edge techniques, i.e. the patch-clamp technique, the fluorescence imaging, and the synthesis and use of model membranes. Moreover, to explore particular aspects of these molecular mechanisms and to overcome the issues raised during the investigations, non-conventional strategies were employed, even requiring the development of specific devices not commercially available.

In summary, my Ph.D. thesis is focused on two projects: the biophysical characterization of a particular class of membrane active peptides, and the modulation of visual phototransduction in vertebrate cones.

In the first project, I investigated the mechanism of membrane perturbation of cell-penetrating and antimicrobial peptides using the patch-clamp technique. Cell-penetrating peptides (CPPs) are short peptides that are able to cross the cell membrane via energy-dependent and/or independent mechanisms, with low toxicity and without the use of specific receptors (Bechara and Sagan, 2013). This ability is preserved even when CPPs are conjugated with a large cargo, thus representing an innovative pharmacological tool for the diffusion of large and hydrophilic drugs into the cells (Stewart et al., 2008). Despite the mechanism of cellular uptake is still debated in literature, it has been proved that it can occur by either direct translocation (Derossi et al., 1996; Vivès et al., 1997) or endocytosis (Richard et al., 2003; Duchardt et al., 2007). In the latter case, though, the cargo-peptide complex often remains trapped inside the endocytic vesicles and is not able to reach its therapeutic target (Lindgren et al., 2000). A possible solution to this problem could be found in another class of small peptides, similar to CPPs, i.e. the antimicrobial peptides (AMPs). AMPs are 12-50 amino acids long peptides, which represent an essential part in the innate immune system in most organisms. Indeed, they are among the first defensive molecules released during infections and their activity is direct thorough the membrane of bacteria, causing its destruction and consequently the death of the pathogen (Reddy et al., 2004). Therefore, the ability of AMPs to disrupt biological membranes could be exploited to improve the CPPs escape from the endocytic vesicles in addition to, of course, their application as a novel class of antibiotics. The idea is to conjugate the CPP with a molecule that possess an antimicrobial activity, which can destroy the vesicle membrane, and help the complex to reach its target once it has been internalized in the cell.

On this ground, the first project I carried out regards the study of a novel chimeric peptide, CM_{18}-Tat_{11}, composed of the antimicrobial peptide CM_{18} (a cecropin-mellitin hybrid peptide) linked to the cell-penetrating peptide Tat_{11} (derived from the basic domain of HIV-1 Tat protein). In particular, I investigated the membrane perturbing activity of this peptide (and of its elements) using the patch-clamp technique and operating under strictly physiological conditions. This study has been carried out by recording the ion current flowing through the channels formed by these peptides (if any), once inserted in the membrane of Chinese hamster ovary (CHO) cells. In these experiments, the peptides were applied to (and removed from) the extracellular CHO membrane in ~50 ms with a computer-controlled microperfusion system. Therefore, besides assessing ion channel characteristics, the dynamics of pore formation and disaggregation could be precisely evaluated as well. I found that CM_{18}-Tat_{11} produces a large and irreversible plasma membrane lysis, at concentration where CM_{18} and Tat_{11} give instead a nearly reversible membrane permeabilization and no perturbation, respectively. Furthermore, using the same method, I studied the biophysical characteristic of another antimicrobial peptide, called CM_{12}, which sequence was obtained from the optimization of CM_{18} (Maccari et al., 2013). When applied on CHO, CM_{12} and CM_{18} produce voltage-independent membrane permeabilization, and no single-channel events were detected at low peptides concentration. These results indicate that both peptides form pores according to a toroidal model, in which the lipid layer bends continuously through the pore so that the core is formed by both lipid head groups and the peptides. Finally, I have studied the single channels properties generated by the pore-forming peptide alamethicin (Alm) F50/5 and its [L-Glu(OMe)[7,18,19]] analog inserted in a natural membrane and in giant unilamellar vesicles (GUVs). The possibility to compare the channel activity in the precisely controlled lipid environment of GUVs, with the one recorded in a natural membrane, will open new possibilities in the biophysical characterization of the pores.

The second project of this thesis is focused on the study of the physiological role of the calcium sensor GCAP3 (guanylate cyclase activated protein 3) in the phototransduction cascade in zebrafish. I pursued this study simulating the over expressions and the knockdown of this protein, through the delivery of zGCAP3, or of its monoclonal antibody, into zebrafish cone cytoplasm, while recording their photoresponses with the patch-clamp technique. The proteins were administered inside the cone via the patch pipette thanks to an intracellular perfusion system developed in this thesis. This system allows the delivery of exogenous molecules inside the cell with a controlled timing, by expelling them with a small teflon tube inserted into the pipette lumen controlled by a microperfusion apparatus. Results indicated that the increase in the concentration in zGCAP3 did not altered significantly the light response, while the perfusion with the antibody anti-zGCAP3 caused the progressive fall of the dark current, together with the progressive slowing down of the flash response kinetics. The surprising lack of an effect of zGCAP3 incorporation,

II

suggests that the endogenous number of zGCAP3 is saturating, therefore any further increase of this sensor is ineffective. However, the effects of the antibody can be explained as an inhibition of the target enzyme of zGCAP3, which is the guanylate cyclase (GC).

Finally, no experiments mentioned above would have been accomplished without the development of a "pressure-polishing" system, which makes it possible to modify the geometry of the patch-clamp pipette. The pipette shank (the final part of the pipette) is, in fact, very long and tapered, thus generating a high resistance to the passage of ions and molecules, and making very difficult to perfuse efficiently the cell with the internal perfusion. The pressure polishing setup I developed enlarged the patch pipette shank, using a calibrated combination of heat and air pressure. These pipettes minimized errors in membrane potential control and allowed the insertion of teflon tubes in the pipette lumen very close to its tip.

Table of Contents

Abbreviations

Aib	*α-aminoisobutyric acid*
Alm	*Alamethicin*
AMP	*Antimicrobial peptide*
ATP	*Adenosine triphosphate*
cGMP	*Guanosine 3',5'-cyclic adenosine monophosphate*
CHO	*Chinese hamster ovary*
CM	*Cecropin-melittin*
CPP	*Cell-penetrating peptide*
DMEM	*Dulbecco's Modified Eagle's Medium*
DNA	*Deoxyribonucleic acid*
GC	*Guanylate cyclase*
GCAP	*Guanylate cyclase activating protein*
GCL	*Ganglion cell layer*
GDP	*Guanosine diphosphate*
GTP	*Guanosine triphosphate*
GUV	*Giant unilamellar vesicle*
HEPES	*N-[2-hydroxyethyl]piperazine-N'-[2ethasulfonic acid]*
HIV	*Human immunodeficiency virus*
I_{max}	*Steady-state current*
INL	*Inner nuclear layer*
IPL	*Inner plexiform layer*
IS	*Inner segment*
ITO	*Indium tin oxide*
LWS	*Long wavelength sensitive*
MCPP	*Multivalent cell-penetrating peptide*
MWS	*Medium wavelength sensitive*
ONL	*Outer nuclear layer*
OPL	*Outer plexiform layer*
OS	*Outer segment*
pAnt	*Antennapedia peptide*
PBS	*Phosphate buffered saline*
PDE	*Phosphodiesterase*

R_a	*Access resistance*
R_m	*Membrane resistance*
Rh	*Rhodopsin (inactive)*
Rh*	*Rhodopsin (active)*
RPE	*Retinal pigment epithelium*
siRNA	*Small interfering ribonucleic acid*
SWS	*Short wavelength sensitive*
τ_a	*Activation time constant*
τ_d	*Deactivation time constant*
Tat	*Trans-activator of transcription*
UV	*Ultraviolet*
V_h	*Holding potential*
zGCAP	*Guanylate cyclase activating protein of zebrafish*

1. Introduction

Part I
Membrane Active Peptides:
Biophysical Characterization in Natural and Model Membranes

1.1   Cell-Penetrating Peptides

Cell-penetrating Peptides (CPPs) are short peptides that have the ability to translocate across the cell membrane in a non-disruptive way, overcoming the semipermeable nature of biological membranes. Since their discovery, more than twenty years ago, it was clear that a deeper knowledge of CPPs could have been very useful in many ways. First of all, studying these peptides can help to shed light on the prime mechanism of cellular entry across the plasma membrane; but CPPs represent also an innovative tool for the delivery of different molecules inside the cells.

Historically, the first observation that some proteins were able to pass thorough the membrane was made in 1988, when Frankel and Pabo were developing an assay to measure the activity of the Tat protein from the Human Immunodeficiency Virus 1 (HIV-1). They observed an unexpected result: purified Tat, a regulatory protein that *trans*-activate genes expressed in HIV genome, was taken up by cells in culture without using any loading method (Frankel and Pabo, 1988). In the same year, another group made the same observations (Green and Loewenstein, 1988), and both works were published simultaneously. Later, a new polypeptide, pAnt, was discovered, derived from the *Antennapedia* transcription factor of *Drosophila melanogaster*, that is able to penetrate neurons and regulate their morphological differentiation (Joliot et al., 1991).

The interesting activity of these proteins, and of their transduction domain, stimulated researchers to find the shortest amino acid sequence necessary for the uptake. This led to the identification of the first CPPs: Tat peptide, that corresponds to the basic domain of HIV-1 Tat protein (Vivès et al., 1997) and penetratin, corresponding to the third helix of the *Antennapedia* homeodomain (Derossi et al., 1994). Nowadays, several peptides showing the same penetrating activity have been discovered and studied, but this field of research is relatively young, and there are a lot of question still unanswered. In particular, the mechanism through which CPPs operates remains subject of controversy in the literature. Moreover, many efforts are made in order to exploit the ability to cross the membrane for the internalization of drugs, and more generally molecules, called cargoes, into the cell. In the following sections, a brief overview on CPPs will be given, firstly

presenting a general classification of these peptides, followed by the most accepted theories on the mechanism of internalization and their pharmaceutical use in drug delivery.

1.1.1 Classification of CPPs

Despite their low number of amino acids, usually less than 30, CPPs differ considerably in terms of composition and 3D structure. According to the physical-chemical properties of their sequences, it is possible to identify three main classes of CPPs: hydrophobic, amphipathic and cationic peptides. Most of CPPs have a net positive charge, but also anionic and neutral peptides are present in this large family.

Recently, several groups have proposed a clearer overview, based not only on the primary sequence of the CPP, but also on the conformation arranged by the peptide when is in contact with the cell membrane (Fernández-Carneado et al., 2004; Deshayes et al., 2005). Here, amphipathic peptides are also subdivided in primary and secondary amphipathic peptides. Primary amphipathic peptides, such as trasportan (Pooga et al., 1998) and Pep-1 (Morris et al., 2001), contain typically more than 20 amino acids, and alternate hydrophobic and cationic domains in their primary sequence. On the other hand, peptides that exhibit their amphipathic characteristic only through a change in their secondary structure are called secondary amphipathic CPPs. They are usually smaller, and upon interaction with lipids assume the classic α-helical or β-sheet conformations, which allow the positioning of hydrophobic and hydrophilic residues in separate faces of the molecule and are essential for the penetrating activity. In this group are present penetratin (Derossi et al., 1996), proline-rich CPPs, and the model amphipathic peptide (Oehlke et al., 1998). Finally, there are non-amphipathic CPPs whose sequence is very hydrophobic or presents mostly cationic amino acid. This class includes Tat peptide (Vivès et al., 1997) and polyarginine peptides (e.g. R_9) (Futaki et al., 2001; Tünnemann et al., 2008), and they do not require a specific 3D-structure for uptake (Eiríksdóttir et al., 2010).

Another simple classification is based on the origin of the peptide (Table 1.1), and in this case we can distinguish protein-derived peptides, chimeric peptides (formed by the fusion of two natural sequences), and synthetic peptides rationally designed starting from natural sequences (especially antimicrobial peptides).

1.1.2 Mechanism of Action of CPPs

A common feature of CPPs is that they are able to penetrate the cell membrane at low micromolar concentrations, both *in vivo* and *in vitro*, with very low toxicity (Mäe and Langel, 2006; Järver et al., 2010). However, as previously mentioned, in literature there is no consensus about the mechanism of cellular internalization. Of course, the wide structural diversity among these

peptides results in different modes and levels of uptake, but also the type of cargo carried by the CPPs, cell type, and the experimental conditions can affect profoundly their uptake mechanism. The first studies on penetratin, Tat, and R_9 indicated that the internalization of these peptides is receptor-independent and not significantly suppressed by depletion of the intracellular ATP, by inhibitors of endocytosis, or by low temperatures (Derossi et al., 1996; Vivès et al., 1997; Futaki et al., 2001; Suzuki et al., 2002). Based on these results, it was commonly accepted that these peptides were entering the cells via direct translocation through the membrane lipid bilayer. Not long after, though, Lebleu and colleagues discovered that most of the methods used in those experiment, especially the cell fixation with methanol prior to fluorescence assays, led to artifactual results (Richard et al., 2003). In this way, they re-evaluated the mechanism of uptake based on endocytosis and, from then, the research was mainly directed on that field. Pharmacologically, in fact, endocytosis is the most interesting mechanism of internalization, since applications of CPPs focused on import of macromolecular cargo, and endocytosis is the preferred route for cargo uptake (Tünnemann et al., 2006). Nowadays, both energy-independent translocation and endocytosis are commonly accepted, even for the same CPP, with the latter believed to be the most common mechanism at low peptide concentrations (Holm and Langel, 2005; Nakase et al., 2009).

Direct Translocation

Direct translocation via energy-independent mechanisms may include different pathways such as inverted micelle formation (Derossi et al., 1996), pore formation (Herce et al., 2009), carpet-like perturbation (Piantavigna et al., 2011), and the membrane thinning model (Herce and Garcia, 2007). In any case, the first step in all these mechanisms is the interaction of the CPP's positive charge with the membrane components that are negatively charged. The subsequent destabilization of the membrane is often associated with peptide folding, and vary a lot depending on the peptide sequence and concentration, as well as the lipid/protein composition of the membrane.

In the "inverted micelle" model (Figure 1.1), initially proposed for pAnt (Berlose et al., 1996), the interaction of the peptides with the membrane slightly disrupts the lipid bilayer, leading to the formation of hexagonal structures (inverted
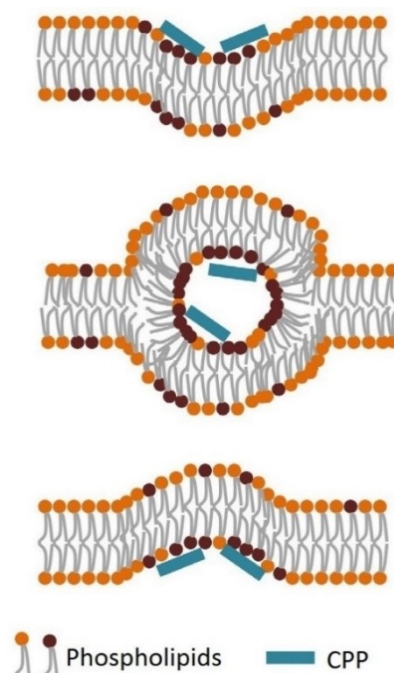
Figure 1.1 Inverted micelle formation (modified from Bechara and Sagan, 2013).

micelles). The CPPs remain confined in the hydrophilic core of the micelles, until the inverse process occurs and the peptides are released in the intracellular environment.

However, given the limited space inside the micelles, this mechanism is not likely to occur for macromolecular complexes (e.g. CPP-cargo conjugates), but admits only the uptake of small hydrophilic peptides. The "pore formation" and the "carpet-like" model are analogue to those mechanisms of membrane perturbation used to explain the activity of AMPs, and will be further described in detail in this thesis (see *Mechanisms of Action of AMPs*).

Finally, since direct translocation occurs only when the CPPs reach a threshold concentration on the membrane, all these mechanisms requires the cell membrane to face high concentration of the peptides and extensive destabilization. These results are in conflict with the features of many CPPs, i.e. low cytotoxicity and low-concentration efficacy; therefore, none of the models described above can give a complete explanation of the data experimentally obtained, suggesting that alternative pathways should participate in peptide translocation.

Endocytosis

Endocytosis is an energy-dependent process that triggers the uptake of molecules (or even other cells) of different type and weight (Conner and Schmid, 2003). This is not a single mechanism; in fact, two different pathways can be recognized: phagocytosis and pinocytosis. The first one occurs only in specialized cells (e.g. macrophages) and, of course, is not involved in CPPs mechanism of action. On the contrary, pinocytosis is common among many eukaryotic cells and seems to play an important role in the internalization of CPPs, especially when they are conjugated with large cargoes (Lundin et al., 2008). There are four basic modes of pinocytosis: macropinocytosis, clathrin-dependent endocytosis (CDE), endocytosis mediated by caveolae, and clathrin and caveolae-independent endocytosis (Figure 1.2). Macropinocytosis is a non-specific process that leads to the formation of large vesicles, called macropinosomes (> 1 μm), generated by a membrane ruffling that surrounds and gradually internalizes part of the extracellular fluid and all the molecules dissolved inside it (Swanson and Watts, 1995). In CDE, the formation of the vesicle is preceded by the interaction of a ligand with specific transmembrane receptors, which cause invagination of a clathrin-coated piece of membrane. A receptor binding is also required in the endocytosis mediated by caveolae, but while the clathrin-coated vesicles are about 120 nm in diameter, caveolin-coated do not exceed 50-60 nm (Mayor and Pagano, 2007). Finally, clathrin and caveolae-independent endocytosis group several mechanisms that are related to the internalization of microdomains present on the cell surface, called 'rafts' (Conner and Schmid, 2003).

It is now evident that CPPs do not enter the cells via a single favorite method; indeed, the mechanism used strongly depends on their attached cargo (Maiolo et al., 2005). For instance, Tat

peptide uses a clathrin and caveole-independent endocytosis when conjugated to a protein (Fittipaldi et al., 2003), but clathrin-dependent endocytosis when conjugated to a fluorophore (Richard et al., 2005). Furthermore, it is important to emphasize that all endocytic processes end with the enclosure of the CPP and its linked cargo into lipid vesicles, where they can remain for extended periods of time and undergo degradation. In order to exploit CPPs for clinical applications, an efficient vesicular escape is therefore needed. At the present, several studies have the primary goal to overcome this problem, and some of them will be introduced in the next section, dedicated to the therapeutic applications of CPPs.
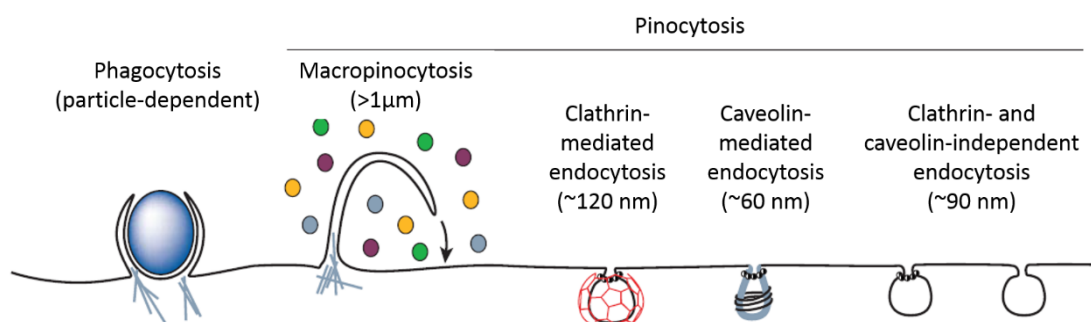
Figure 1.2 Different endocytic pathways. Phagocytosis is limited to specialized cells (e.g. macrophages); CPPs can enter the cells by using all pinocytosis mechanisms (Conner and Schmid, 2003).

1.1.3 Applications in Drug Delivery

As mentioned before, the ability of CPPs to translocate across the cellular membrane represents a major breakthrough for the introduction of drugs and large molecules into the cells for therapeutic purposes. At the moment, we are witnessing a dramatic acceleration in the development of novel therapeutic molecules such as proteins, peptides, nanoparticles and numerous nucleic acids: oligonucleotides, small interfering RNA (siRNA), plasmid and viral genes. Unfortunately, due to their physicochemical properties, these compounds exhibit several issues like poor stability *in vivo* and lack of cellular uptake and specificity. Therefore, the optimization of their intracellular delivery is one of the major priorities, and CPPs seems to be excellent candidates for this goal, offering several advantages over other tested vectors like liposomes or nanotubes (Veldhoen et al., 2006; Cirillo et al., 2014; Mallick and Choi, 2014).

Indeed, many studies present promising results in CPP-mediated intracellular delivery of many drugs, both *in vitro* and *in* vivo, including antisense oligonucleotides (Astriab-Fisher et al., 2002), antibodies (Morris et al., 2001), peptides and proteins (Snyder and Dowdy, 2005; Gros et al., 2006), and even contrast agents for *in vivo* imaging (Kersemans et al., 2008). The most representative applications of CPPs are reported in Table 1.1.

Table 1.1

Most representative CPPs: origins and applications.

CPP	Origin	Cargo types
Protein-derived		
Tat_{11}	HIV-Tat protein (48-58)	protein/peptide/siRNA/liposome/nanoparticles
Penetratin	Antennapedia (43-58)	peptide/siRNA/liposome
Chimeric-peptides		
Pep-1	Trp-rich motif/SV40 T-antigen	protein/peptide
MPG	HIV-gp41/SV40 T-antigen	siRNA/ODN/plasmid
Transportan	Galanin/Mastoparan	protein/PNA/siRNA
Synthetic-peptides		
Polyarginine	Based on Tat peptide	protein/peptide/siRNa/ODN
MAP		small molecule/plasmid

ODN, oligodeoxynucleotide; PNA, peptide-nucleic acid.

Covalent or Non-Covalent?

Among the numerous attempts in using CPPs as drug carriers, we can distinguish two principal strategies. The first one is the covalent strategy, which requires the formation of a covalent bond between the CPP and the cargo, achieved by either chemical cross-linking (Zorko and Langel, 2005; Lundin et al., 2008) or by cloning and expression of recombinant conjugates (Münst et al., 2009; Heffernan et al., 2012). Despite all the advantages offered by covalent technology (high reproducibility and stoichiometry control), the synthetic covalent bond can alter the biological activity of the cargo, thus resulting in a loss of its function. This problem especially concern siRNA and oligonucleotides conjugates (Meade and Dowdy, 2007; Juliano et al., 2008), for which non-covalent strategies appear to be a better solution (Simeoni et al., 2003). In this case, in fact, the cargo molecules do not undergo any chemical modifications, since they are associated with the CPPs only through electrostatic and hydrophobic interactions (Morris et al., 2001; Simeoni et al., 2003; Gros et al., 2006).

Overcoming Endosomal Entrapment

In order to exert its pharmacological activity, it is important for the cargo to reach its specific target. To ensure this, the passage through the cellular membrane is not the only limiting step. Indeed, CPP-cargo conjugates that enter the cell following one of the endocytic pathways are often sequestered into vesicles, keeping them from reaching their intracellular target. In addition, along with the endosomal membrane barrier, trapped macromolecules have to face a pH decrease and the attack by hydrolytic enzymes (Lee et al., 2008).

In recent years, many research groups proposed several solution to enhance endosomal escape (Erazo-Oliveras et al., 2012). One approach suggests the use of multivalent CPPs (MCPPs), which consist of creating an oligomer with multiple copies of the same CPP, in order to increase its local concentration when it interacts with membranes (Kawamura et al., 2006; Hassane et al., 2009).

MCPPs can be obtained by attaching two or more CPP monomers with protein highly branched molecules (Juliano et al., 2008), scaffolds (Sheldon et al., 1995) or simple disulphide bridges (Rudolph et al., 2004). Despite their encouraging increase in activity, the complex and expensive methods for the synthesis of MCPPs is an important limitation. Moreover, it is possible that similar compounds could act as immunogens, producing an unpleasant immune response (Schwarze et al., 1999).

Another approach that has been proposed to increase endosomal escape is based on the addition of chromophores that, upon activation with an appropriate light stimulus, are able to disrupt the vesicle membrane. Here, CPPs are linked to fluorophores (Maiolo et al., 2004) as well as to photosensitizers (Choi et al., 2006; Zhao et al., 2011), but in several experiments a significant phototoxic activity is observed, causing cell damage and apoptosis (Choi et al., 2006; Oliveira et al., 2007).

The endosomal entrapment of CPP-cargo complexes can be overcome also with the help of other specific peptides. For instance, pH-dependent membrane-active peptides (PMAPs) are pH-sensitive peptides that become active only in acid environment (El-Sayed et al., 2009). This activity is extremely advantageous in this context, since the pH in the endosome lumen gradually drops as maturation occurs (Schmid et al., 1989; Serresi et al., 2009). An example of PMAP is the HA2 fusion peptide, which has been proved to increase endosomal escape of several cargoes when associated with CPPs such as Tat peptide (Kumar et al., 2007; Lee et al., 2011) and penetratin (Lundberg et al., 2007). Another class of peptides that received researchers' attention is the antimicrobial peptides (AMPs) family. These small peptides possess membrane-perturbing activity (see Section 1.2, dedicated to AMPs); therefore, they might be able to permeabilize the endosome membrane leading to the release of its contents.

The work of this thesis is in part dedicated to the study of an AMP-CPP hybrid, called CM_{18}-Tat_{11}, synthetized by the group of prof. Beltram of NEST laboratory (*Scuola Normale Superiore* and *Istituto Nanoscienze-CNR*, Pisa): the characteristics of this novel peptide will be described in details in Section 1.3.1.

1.2   Antimicrobial Peptides

The first discovery of substances that possess antimicrobial activity dates back to the first half of the nineteenth century, when many compounds isolated from normal tissues and body fluids were found to kill both Gram-positive and Gram-negative bacteria (Skarnes and Watson, 1957). Nowadays, we know that those molecules are evolutionally conserved oligopeptides that play an important role in the innate immune response. To date, the antimicrobial peptide (AMP) database contains 2480 peptides (http://aps.unmc.edu/AP/main.html, last update: Dec 2014) which have been identified in several species ranging from bacteria to mammals, including humans and plants (Wang and Wang, 2004).

AMPs are typically short sequences (between 12 and 50 amino acids), with a net positive charge that range from +2 to +9. In addition to their broad spectrum activity against both Gram-positive and Gram-negative bacteria, some AMPs are also lethal for parasites, fungi, yeasts, and viruses (Zasloff, 2002). Furthermore, a promising anti-tumorigenic activity of some AMPs has also been observed (Papo and Shai, 2005; Hoskin and Ramamoorthy, 2008; Schweizer, 2009). Some early observations also suggest that AMP function is not exclusively limited to innate immunity. Some peptides, e.g. defensins, seem to modulate angiogenesis, promote inflammatory response and stimulate adaptive immune system by inducing cytokine secretions, recruiting dendritic cells and macrophages (Suarez-Carmona et al., 2014). All these properties make AMPs a promising resource in the development of new drugs, not only as new antibiotics, but also against tumors and many other diseases (Reddy et al., 2004).

The mechanism of action used by several AMPs in their antimicrobial activity is based on the formation of transmembrane pores on the bacterial membrane, altering its permeability and leading to bacteria's death (Figure 1.3). For this reason, and given their evolutionary conserved sequences, AMPs provide a simple model in understanding the molecular basis of peptide-lipid interactions in membranes, as well as the structure-function relationships of ion channels, ion pumps and exchangers (Marsh, 1996). A better knowledge of such mechanisms could then be exploited to build custom molecules with a wide range of applications in biotechnology, like ion channel modulators (Hille, 2001), biosensors for several analytes (Aili and Stevens, 2010), and may provide also a pharmacological approach for the treatment of channelopathies (Wilde, 2008). In the latter case, a synthetic channel could incorporated in cells expressing an aberrant ion channel and restore the physiological ion flow. Encouraging results have been obtained in human epithelia of the cystic fibrosis patients with a defective chloride channel (Wallace et al., 2000).
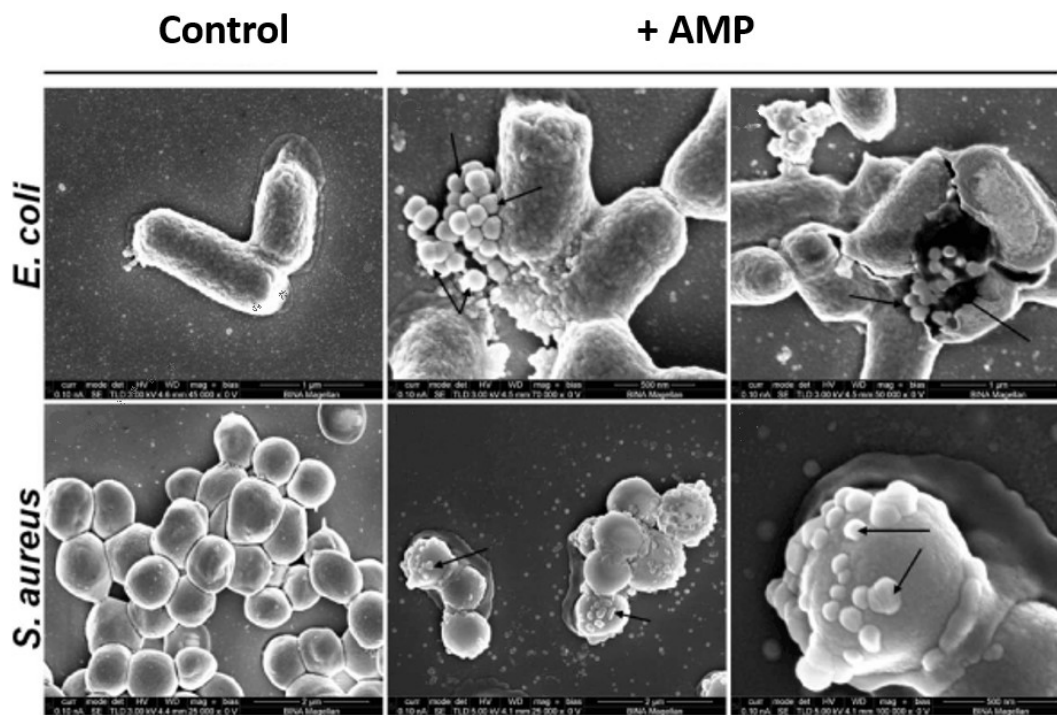
Figure 1.3 Scanning electron microscopy of two different bacterial strains untreated (*control*), and treated with AMPs (*+ AMP*). Upon peptide interaction, bacterial membranes appear corrugated and show small protruding blebs (*arrows*) (modified from Bi et al., 2014).

1.2.1 Classification of AMPs

As for CPPs, AMPs can also be classified in different ways according to their origin, amino acid sequence and structure. From a structural point of view, we can distinguish two major groups: α-helical peptides and β-sheet peptides. The first group includes cecropins (the first AMP identified) and magainins, and more in general linear cationic peptides, with less than 40 amino acids, that lack cysteine residues (Brogden, 2005). They are disordered in aqueous solutions, but have the tendency to form highly amphipathic helix in organic solvents and lipid vesicles (Marion et al., 1988; Bechinger, 1999). In this case, the folded peptide exhibits its hydrophilic amino acids residues along one side of the helix and its hydrophobic amino acids residues along the opposite side, thus allowing the contact with both the lipids and the aqueous environment. In the second group are present anionic and cationic AMPs with cysteine in their sequence and form one or more disulfide bridge that maintain the β-sheet structure of the peptide (Dhople et al., 2006). The most representative AMPs in this group are defensins, derived from humans and several mammals, and protegrin. Other peptides not included in this simple classification are cyclic AMPs and cationic peptides enriched for specific amino acids like proline, arginine or tryptophan (Reddy et al., 2004).

1.2.2 Mechanisms of Action of AMPs

In literature, two different strategies are proposed for the antimicrobial activity of AMPs. The most validate mechanism is the previously mentioned formation of transmembrane pore, which cause an extensive membrane rupture leading to the lysis and death of the microbial cells. However, recent studies revealed that AMPs might have also intracellular targets, including DNA, RNA, and protein synthesis, as well as enzymatic processes essential for bacteria metabolism (Lee and Lee, 2014; Choi et al., 2015). These mechanisms are not fully understand yet, thus more researches are required on this argument. On the other hand, the membrane-disrupting activity of AMPs has been deeply investigated in the last years. By now, there are three main models able to describe the AMPs modes of membrane perturbation (Figure 1.4): "barrel-stave", "toroidal" and "carpet" model (Brogden, 2005).

Barrel-stave Model

In the barrel-stave model, the peptides initially bind in parallel on the membrane surface due to an electrostatic interaction (Figure 1.4 *A*). As the peptide monomers accumulates on the membrane, they insert perpendicularly in the membrane and bind together around a central pore, arranging like the staves of a barrel (Figure 1.4 *B*). In this structure, the peptide helices are organized in a way that the hydrophobic residues interact with the lipid core of the membrane, while the hydrophilic segments face the aqueous lumen of the pore. According to this mechanism, when a peptide monomer inserts in the bilayer, it recruits other peptides to form the aggregates, acting in a cooperative way. One of the most representative peptide acting with this mechanism is alamethicin (Baumann and Mueller, 1974).

Toroidal Model

The toroidal pore differs from the barrel-stave one in that the peptide monomers do not aggregate with each other, but rather interact with the polar head groups of the lipids, even when the peptides are arranged vertically in the membrane. The interaction between the peptides and the phospholipid head groups is stronger than in the case of the barrel-stave model, so that the lipid monolayer is forced to bend back on itself, connecting one side to the other of the membrane, in a toroidal shape manner. Therefore, the pore walls are formed by lipids and peptides, and not by peptides only as in the barrel-stave model (Figure 1.4 *C*). This particular model was first proposed to describe the pores formed by the peptide magainin (Ludtke et al., 1996; Matsuzaki et al., 1996).

Carpet Model

In the carpet mechanism, the strong electrostatic interaction between the peptides and the phospholipid head groups leads to a peptide-induce membrane 'carpeting' effect. Once the peptides have reach a threshold concentration on the membrane, they assemble to form

transiently toroidal pores, allowing more and more peptides to cross the membrane and eventually cover the other membrane leaflet, so that the bilayer is rapidly and extremely perturbed and disintegrated. It is also possible that entire fragments of the membrane, called micelles, are detached from the membrane itself in a detergent-like manner (Figure 1.4 *D*).

Of course, similarly to the case of CPPs, the same AMP do not act following exclusively one of the models described above. Indeed, it has been demonstrated that temperature, peptide concentration, the presence of metal ions and other environmental conditions might change the activity of the same AMP from one mechanism of action to another (Brogden, 2005; Noshiro et al., 2010).
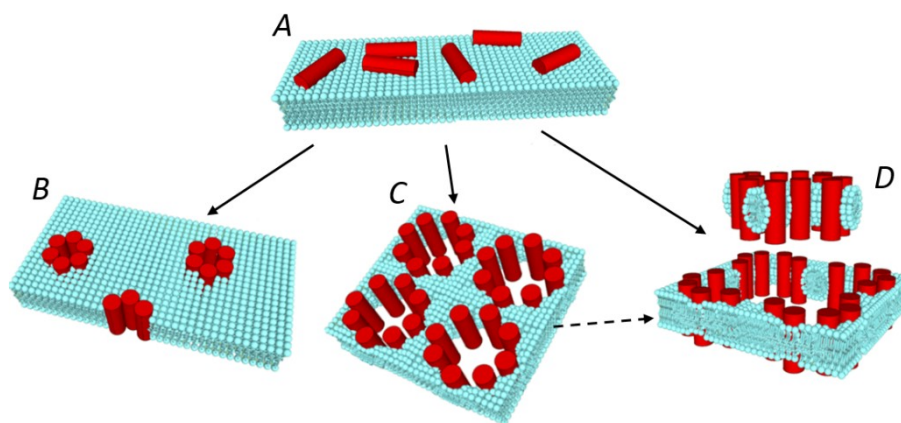
Figure 1.4 Mechanisms of peptide-induced membrane permeabilization. After adhering on the external face of the membrane (*A*), the peptide could insert in the membrane according to a barrel stave (*B*), toroidal (*C*), or carpet mechanism (*D*).

1.2.3 AMPs vs Multidrug-Resistant Bacteria

Since the discovery of penicillin, antibiotics are considered one of the major discoveries of modern medicine. Unfortunately, the dramatic increase in antibiotic-resistant bacterial strains causes a loss of efficacy of these broadly used drugs, with negative consequences in the healthcare system along with social and economic implications (Huttner et al., 2013; Rossolini et al., 2014). Furthermore, the multidrug-resistant infections that in the past years were limited to hospital or large communities, are now spreading all over the world. Thus, innovative strategies for the development of new treatments are urgently needed.

Among all the ongoing attempts to find a solution to the so called "antibiotic resistance crisis", AMPs represent an encouraging resource for future drug development. The reason is that all the strategies developed by microorganisms in order to overwhelm antibiotics are entirely intracellular mechanisms: 1) alteration of the antibiotic target (Wilson, 2014); 2) antibiotic

12

degradation by specific enzymes (Wright, 2005); 3) antibiotic expulsion thorough membrane pumps (Li and Nikaido, 2004). On the other hand, the effect of the AMPs against the bacterial membrane is driven by an aspecific interaction with the peptides and the double layer. Since modifications in the physical structure of the membrane are very difficult to occur, the development of an AMP resistance is very unlikely.

1.3 Aim of This Work (pt. I): Mechanism of Action of Membrane Active Peptides

In literature, several strategies are described to assess the mechanism of AMPs activity. A simple and direct method is the observation via microscopy techniques of the microbial cell integrity after the application of AMPs (Kalfa et al., 2001; Yenugu et al., 2004). To study the biophysical interactions between peptides and membrane, a large variety of techniques are also employed, such as nuclear magnetic resonance, surface plasmon resonance (Aquila et al., 2013), circular dichroism and electron paramagnetic spectroscopy (Pistolesi et al., 2007). The long-term goal of these researches is the investigation at a molecular level of the lipid-peptide interaction, from orientation to conformational changes. Moreover, since pore formation is the AMPs favorite mechanism of action, a widely used experiment to assess their membrane permeabilization is the measure of the leakage of a fluorescent molecule previously confined into phospholipid vesicles (Orioni et al., 2009). However, none of these studies addresses directly the problem of the kinetics of pore formation when peptides assemble on the plasma membrane of a living cell.

The dynamics of the formation of the AMP pore and its biophysical characteristics are investigated in this thesis under strict physiological conditions. For this purpose, the peptides are applied on the membrane of a living cell, and the ionic current that flows through the pore formed by these peptides is simultaneously recorded by using the patch-clamp technique (described in *Materials and Methods*). The first part of my Ph.D. work was focused on membrane active peptides is dedicated to the biophysical study of the mechanism of membrane perturbation of two peptides: the novel chimeric peptide CM_{18}-Tat_{11} (and its isolated parts) and the rational designed AMP CM_{12}.

1.3.1 CM_{18}-Tat_{11}: a Chimeric CPP with Membrane-Disruptive Properties

The arginine-rich Tat peptide (Tat_{11}, residues 47-57 of HIV-1 Tat protein) is able to stimulate an efficient endocytosis of a large variety of cargoes into a wide range of target cells (Brooks et al., 2005). These properties, plus the low toxicity for eukaryotic cells, make this peptide an excellent resource in drug delivery. Unfortunately, all reports show that molecules taken up by Tat_{11}-mediated endocytosis undergo endosomal entrapment, limiting their intracellular availability. To overcome this problem, it was proposed to link Tat_{11} with a sequence that possess membrane-disruptive properties. An attempt was made with the fusogenic peptide HA2, derived from the influenza-virus hemagglutinin protein (Skehel et al., 2001). In this case, despite a slight enhancement of endosomal entrapment was observed (Wadia et al., 2004), still more than 99% of the Tat-cargo complexes remains sequestered into vesicles (Kaplan et al., 2005).

Another resource of molecules that are able to disrupt the phospholipid barrier comes from the AMPs. In this thesis, the biophysical characteristics of a novel hybrid peptide formed by the CPP

Tat$_{11}$ and the hybrid AMP, called CM$_{18}$, are studied. Among all the AMPs included in this large class of peptides, Cecropin-A/Melittin (CM) hybrids raised particular interest because they are among the shortest and most effective peptides with membrane-permeabilization properties. Cecropin-A is a linear, naturally occurring, cationic peptide initially isolated from the hemolymph of the silk moth *Hyalophora cecropia* (Steiner et al., 1981). Its 37 amino acids sequence can be divided in two segments: a cationic, amphipathic N-terminal domain and a hydrophobic C-terminal domain. Cecropin has shown to be active against both Gram-negative and Gram-positive bacteria, as well as against some fungi and tumor cell lines (Andreu et al., 1985). Moreover, cecropin-A possess a relatively slight hemolytic activity and exhibit low toxicity toward normal eukaryotic cells (Boman et al., 1989; Wade et al., 1992). Melittin, in contrast, is extremely hemolytic and has a stronger, broad-spectrum antimicrobial activity. This 26-residue peptide is isolated from the venom of the honey bee *Apis mellifera*, and contains, as cecropin-A, two distinct cationic and hydrophobic domains but in reverse order (Boman et al., 1989; Andreu et al., 1992). The cecropin-melittin hybrid are constructed combining different domains of these two peptides, with the intent to find the shortest sequence that display a remarkable antimicrobial activity, yet lacking the melittin-associated hemolytic properties. In particular, CM$_{18}$ hybrid (sequence: KWKLFKKIGAVLKVLTTG) is synthesized by combining the first seven residues of cecropin-A with residues 2-12 of melittin.

Despite the recent results that indicate an efficient uptake and endosomal escape of cargoes associated with the chimeric CM$_{18}$-Tat$_{11}$ (Salomone et al., 2012), its mechanisms of membrane permeabilization are still unknown. In this thesis, a biophysical characterization of the membrane activity of CM$_{18}$-Tat$_{11}$ and its isolated domains is given, providing some suggestions about their mechanism of action.

1.3.2 The Rational Designed Peptide CM$_{12}$

Despite their promising properties, the use of some natural AMPs for therapeutic applications turned out to be problematic, especially due to their high toxicity and vulnerability to proteolytic enzymes (Aoki and Ueda, 2013). For this reason, in recent years several AMP sequences have been improved thanks to a computer-aided optimization (Fjell et al., 2012). Along with the enhancement of the activity of preexisting peptides, the computational approach is exploited also for the identification and design of new sequences that possess an antimicrobial activity and at the same time lack all the unfavorable properties of natural peptides (Kaltofen et al., 2014; Maccari et al., 2015). Part of this thesis work is dedicated to the study of the mechanism of action of a rational designed AMP, called CM$_{12}$, selected and synthetized by Maccari at the Center of Nanotechnology Innovation of NEST, in Pisa (Maccari et al., 2013).

1.3.3 Alamethicin F50/5 and its Analogue [L- Glu(OMe)[7,18,19]]

Alamethicins (Alm) are a family of pore-forming peptides produced by the fungus *Trichoderma viride* (Meyer and Reusser, 1967; Reusser, 1967). Since their sequences contain the non-proteogenic amino acid α-aminoisobutyric acid (Aib), they are called peptaibolic peptides. Alamethicins exhibit broad biological activities, including antibacterial effects against both Gram-positive and Gram-negative bacteria (Meyer and Reusser, 1967; Jen et al., 1987; Béven et al., 1998). It was demonstrated that these peptides are able to form voltage-dependent pores into biological membranes (Fox and Richards, 1982); and different mechanisms of pore formation were proposed to describe alamethicin mode of action. Currently, the most accepted one is the barrel-stave model, firstly proposed by Fox and Richards (Fox and Richards, 1982; Mathew and Balaram, 1983).

Part of this thesis work is focused on the study of the single channel properties formed in natural and model membranes by the synthesized Alm F50/5 peptaibol, which is the major component of the neutral fraction of the alamethicin, and its synthetic analog [L- Glu(OMe)[7,18,19]]. The latter peptide was obtained by substitution of specific amino acids from the primary sequence of Alm F50/5. Specifically, glutamine residues at positions 7, 18, and 19 have been replaced with side-chain esterified glutamic acid residues, since glutamine was found to play a major role in pore formation (Fox and Richards, 1982; Molle et al., 1996). Both peptides were inserted in a cell plasma membrane (of the rod outer segment of the frog retina, recorded in whole-cell) and in membrane-patches excised from giant unilamellar vesicles (GUVs). The possibility to compare the channel activity in the precisely controlled lipid environment of GUVs, with the channel activity recorded in a natural membrane with the same ionic electrochemical gradients, will open new possibilities in the biophysical characterization of the pores.

Part II
# Real-Time Modulation of zGCAP in Zebrafish Green Cones

1.4 Visual Perception

Light perception is one of the most important environmental stimuli for all organisms. Other than being fundamental for the generation and preservation of life on Earth, light is, in most animal, the responsible of many physiological functions including circadian rhythms, defense, food-hunting and other important behavioral reactions. Even though simple life form as Protozoa are sensible to light stimuli, the first draft of the vision function occurred in animals only with the appearance of particular photosensitive cells: the photoreceptors. Initially spread all over the body surface, as in many Invertebrates nowadays, the photoreceptors organized later in small formations called *ocelli*, which represent the first form of a specialized structure dedicated to vision. A crucial step in evolution that allowed the transition from the simple detection of light to real vision is the development of the eye. This organ is composed of transparent accessory structures, with converging lens characteristics, which allow the detection of a highly detailed final image. The image (real, reduced, and inverted) is focused on a layer of neuronal cells, including photoreceptors, arranged like a mosaic to form the retina. Here, the photoreceptors, and other retinal neurons connected with them, translate the light signal into an electrical signal that travel to the brain via axons in the optic nerve (for a complete review, see Masland, 2012).

1.5 Retina

The retina is a thin layer of cells lining the inner surface of the optic bulb (Figure 1.5*A*), and it is actually considered a part of the central nervous system. On the inner side of the eye, the retina is in direct contact with the vitreous humor, while on the other side lies in front of the retinal pigment epithelium (RPE) and the underlying choroid. The RPE is a layer composed of cells that synthetize melanin, a black pigment that captures all the light not absorbed by the retina. This prevents the backscattering of the light towards the receptors and avoids any image detriment.

All vertebrate retinae are composed of five types of neurons: photoreceptors, bipolar cells, ganglion cells, horizontal cells, and amacrine cells. The cell bodies and their processes (long branches that arise from the cell body) are organized in distinct layers, clearly visible at a microscopic examination of a vertical section of the retina (Figure 1.5*B*) (Cajal, 1893; Dowling and

Boycott, 1966). The cell bodies of the photoreceptors are contained in the outer nuclear layer (ONL) while in the inner nuclear layer (INL) there are cell bodies of the bipolar, horizontal and amacrine cells. Ganglion cells bodies are located in the ganglion cell layer (GCL), where also some displaced amacrine cells can be found (Dowling, 1970). In other two different layers, called inner plexiform and outer plexiform layers (IPL and OPL, respectively), are positioned the neuron processes, and these are the areas where synaptic contacts between cells occur. Contrary to what can be expected, photoreceptors are not facing directly the interior of the eye, but lie in the deepest layer against the RPE. As a result, light must pass through the other non-light-sensitive layers of cells as well as the retina vasculature before reaching the photoreceptors. The reason for this counterintuitive organization of the retina lies in the special relationship that exist among the photoreceptors and the RPE. Other than absorbing the excess light, RPE is also essential for the preservation and turnover of photoreceptors and for the restoration of the light-sensitive molecules after they have been exposed to light (Young, 1967, 1971; Bok and Young, 1972; Anderson et al., 1978).
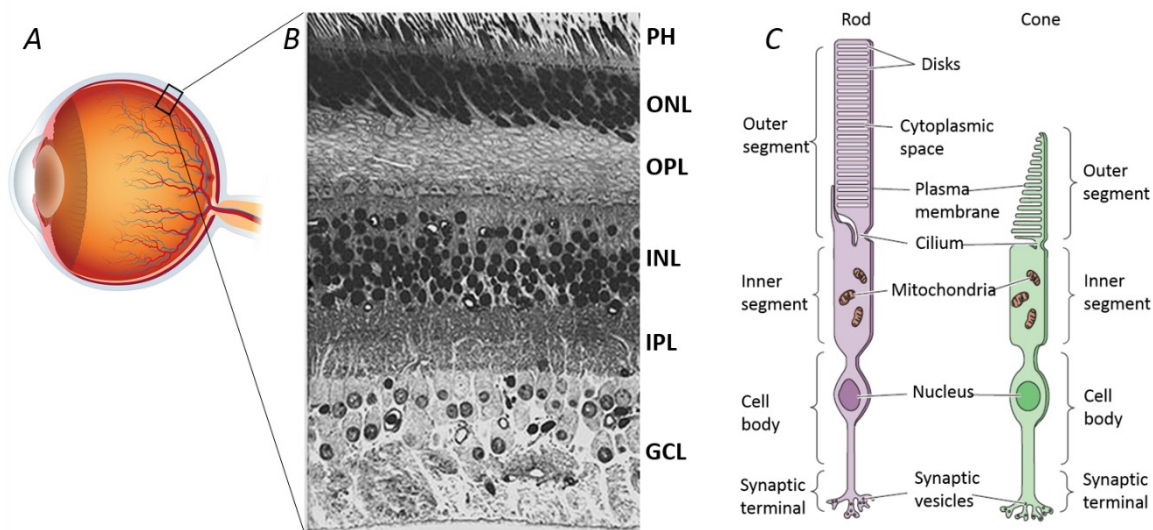
Figure 1.5 Structure of the retina and photoreceptor cell types. (*A*) Eye picture; (*B*) Cross section of the retina (400x), PH: photoreceptors layer, ONL: outer nuclear layer, OPL: outer plexiform layer, INL: inner nuclear layer, IPL: inner plexiform layer, GCL, ganglion cell layer; (*C*) Rod and cone structure.

1.5.1 Functional Architecture of Photoreceptors

Photoreceptors are a class of highly specialized cells responsible for the transformation of a light stimulus into an electrical stimulus, which can reach the brain through the optic nerve. There are two basic types of photoreceptors, distinguished by shape: rods and cones (Figure 1.5*C*). In addition to their different morphology, they also carry out different vision functions (better explained in the following paragraphs); nonetheless, they share several characteristics. Both rods and cones have an outer segment (OS), slim rod-shaped for the former, and robust conical-shaped

for the latter, separated from the inner segment (IS) by a thin cilium (Anderson and Fisher, 1976). Notably, the OS of both types of photoreceptors are entirely filled with a succession of hundreds of flattened discs, disposed one on the other, that originate from invaginations of the plasma membrane (Cohen, 1960, 1964; Besharse and Pfenninger, 1980). The discs are continuously produced from the base of the OS, in the region of the cilium, and while in cones they remain attached to one side of the OS membrane, they completely separate in rods, becoming free-floating discs inside the OS membrane (Steinberg et al., 1980). In these membrane discs are embedded many (thousands) of photosensitive molecules, also called photopigments, which are different in rods and cones, and consists of two parts: a protein called opsin and a chromophore, called retinal (Bowmaker et al., 1978; Bowmaker and Dartnall, 1980). The opsin molecule is synthetized in the IS and binds to the membrane discs at the cilium, whereas the retinal (derived from the vitamin A) is synthetized in the RPE and delivered to the discs via specific carrier molecules (Adler and Martin, 1982; Chader, 1989). The IS is almost entirely occupied with mitochondria, and contains also ribosomes and other cytoplasmic organelles, except for the nucleus that takes place below the IS, in the cell body. Finally, at the lower extremity of the photoreceptor there is an enlargement of the membrane, rich in synaptic vesicles, that forms synapse in contact with second order neurons.

Rods and Dim-Light Vision

The rods are photoreceptor cells that contain only one type of visual pigment, rhodopsin. They are extremely sensitive, up to the single-photon level, with a peak at ~500 nm (Brown and Wald, 1964) and are therefore responsible for scotopic vision, i.e. in dim light conditions, as at night. In order to maximize quantum catch, a very high number of visual pigments is needed, thus explaining the dense packing of the discs in the rod OS. Nevertheless, the price for this high is the much slower photoresponse compared with the one of cones (Baylor, 1987), a poor resolution of the image and no perception of colors (MacLeod, 1972). As a result, rod function provides vision at light conditions even below the level of starlight, but uncolored and with very low spatial resolution.

Cones: Acuity and Color Vision

As illumination increases, the participation of cones in the vision function become more and more important. The cone system is in fact responsible for the perception of higher intensities of light, the so-called photopic vision, and also possess a high spatial resolution due to the high cone density that provides a better visual acuity. Furthermore, cones are responsible for color perception, and can be divided in different classes depending on the type of opsin (the visual pigment of cones) they express. Each of these opsins differ from the others in the sensitivity to light of different wavelengths, and for this reason are referred to as short, medium, and long wavelength sensitive cones (SWS, MWS, and LWS, respectively). More precisely, SWS-cones are

known to peak around 420 nm (blue region of the spectra), MWS-cones peak around 530 nm (green), while LWS-cones are maximally sensitive to wavelength of about 560 nm (red) (Bowmaker and Dartnall, 1980; Bowmaker et al., 1980). Cones are therefore known as blue-, green-, and red-sensitive cones and it has been shown that are morphologically different from each other, allowing their identification simply by optical microscopy (Sherry et al., 1998). Even though the most notorious color identification is based on trichromatic vision (as in humans), most mammalian species are merely dichromatic, while many other vertebrates are tetrachromatic, as they possess a fourth type of cone sensitive to ultraviolet light (UV-cones) (Bowmaker et al., 1980; Branchek and Bremiller, 1984). UV-cones were found among several species of reptiles (Liebman and Granda, 1971), amphibians (Sherry et al., 1998), birds (Bowmaker, 1980), and fishes, including zebrafish (Robinson et al., 1993).

1.6 Phototransduction

Despite the different physiological function of rods and cones (because of their different morphology, response times, wavelength sensitivity, and adaptation mechanism), several phototransduction proteins are similar, or even the same, in any type of photoreceptors. Indeed, it has been proved that they evolve from common ancestors (Hisatomi and Tokunaga, 2002). For this reason, the cascade of intracellular events following light absorption by the visual pigments, named phototransduction, is comparable in all vertebrates (Lamb, 2013). Contrary to what happens in most sensory systems, the stimulation of a photoreceptor do not elicit action potentials; rather, light absorption causes only a graded change in membrane potential, corresponding in a change in the rate of neurotransmitter release onto postsynaptic neurons. Another surprising element is that the light-induced activation of the photoreceptor leads to a hyperpolarization of its membrane potential, rather than a depolarization, as it occurs in many other sensory neurons. All the biochemical events involved in the phototransduction have been deeply studied in the last four decades, and many of them are now well-characterized (for a complete review, see Kawamura and Tachibanaki, 2008). In the following sections, an overall picture of the most important steps in the phototransduction pathway will be given.
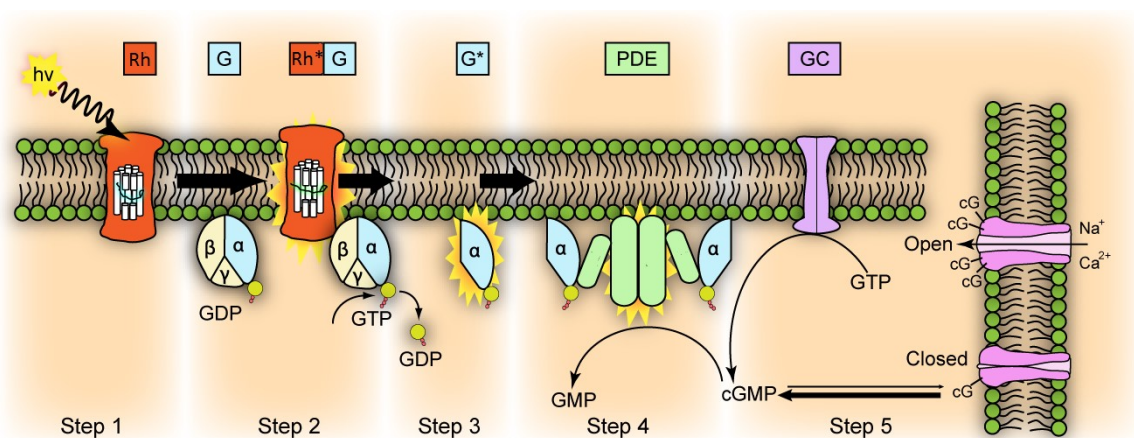
1.6.1 The Dark Current

In the dark-adapted state, the photoreceptors are maintained in a depolarized state by a flux of Na^+ and Ca^{2+} ions that enter into the cells through specific ligand gated channels located in the OS membrane (Hagins et al., 1970). The open- or closed-states of these channels are regulated by the intracellular level of the nucleotide cyclic guanosine monophosphate (cGMP) (Fesenko et al., 1985; Yau and Nakatani, 1985b). In particular, in darkness, the high cytoplasmic concentration of cGMP keeps the channels open, and Na^+ and Ca^{2+} ions are free to enter into the OS. This steady inward current is balanced by an outward K^+ current that flows through non-gated K^+-selective channels that are confined in the IS membrane (Bader et al., 1982; Barnes and Hille, 1989). Furthermore, in the IS membrane are confined several Na^+/K^+-ATPase pumps that are responsible for the maintenance of stable intracellular concentration of Na^+ and K^+ by pumping out Na^+ ions and pumping in K^+ ions (Zuckerman, 1973). The resulting circulating current stabilizes around -40 mV and is called "dark current" (Hagins et al., 1970). In the synaptic terminals, this relatively depolarized membrane potential generates the opening of voltage-sensitive Ca^{2+} channels, to which corresponds the release of glutamate (the photoreceptor neurotransmitter) toward the postsynaptic cell (Sarantis et al., 1988; Copenhagen and Jahr, 1989; Ayoub and Copenhagen, 1991). Light activates an enzymatic cascade which ends with the hydrolysis of cGMP. This causes

the closure of the cGMP-gated channels, and in turn the reduction of the influx of Na^+ and Ca^{2+} ions, the hyperpolarization of the cell, and finally the reduction of glutamate release at the synaptic terminal.

1.6.2 Enzymatic Cascade Activation

Since rod cells are easier to purify compared to cones, the best-characterized phototransduction pathway is so far the one occurring in rods (Figure 1.6), in which the visual pigment is the rhodopsin. Upon photon absorption, the 11-*cis* retinal, which is the light-sensitive moiety of inactivated rhodopsin (*Rh*), isomerizes to a more stable all-*trans* configuration in less than 20 ps, and triggers a conformational change of the entire molecule, that becomes enzymatically active (*Rh**). In this state, *Rh** catalyzes the activation of a G-protein, also known as transducing (G). Transducin is a heterotrimer whose α subunit bounds non-covalently to a molecule of GDP (guanosine diphosphate) when inactive. Upon interaction with *Rh**, α subunit exchanges GDP with GTP, dissociates from transducin, and activates the cGMP phosphodiesterase (PDE). This enzyme causes the hydrolysis of cGMP into 5'-GMP: the fall of the cytoplasmic concentration of cGMP causes the closure of a number of cGMP-gated channels proportional to the amount of light initially absorbed.


Figure 1.6 Phototransduction cascade activation by light.

The dark current sustained in the OS by the entrance of Na^+ and Ca^{2+} ions is therefore reduced, and the change in membrane potential can be detected by electrophysiological recordings performed on single isolated cells (Figure 1.7). This membrane hyperpolarization leads to the closure of the voltage-gated Ca^{2+} channels, and the intracellular Ca^{2+} concentration drops, due to continuous Ca^{2+} extrusion from the cell via the Ca^{2+} pumps (Yau and Nakatani, 1984, 1985a). The

22

decrease in Ca^{2+} concentration reduces or terminates the glutamate release at the synaptic terminal, which is detected by the postsynaptic neuron. The signal is further processed by other neurons present in the higher layers of the retina, and subsequently sent to the brain.

This first step of the phototransduction cascade is characterized by an enormous level of amplification. A single rhodopsin molecule, when activated, can diffuse within the disc membrane and activate hundreds of transducin, each one of which stimulates one PDE enzyme. Each PDE in turn is able to hydrolyze over a thousand of cGMP molecules per second, leading to a final hydrolyzation of more than 10^5 cGMP molecules per second for a single *Rh** (Leskov et al., 2000).
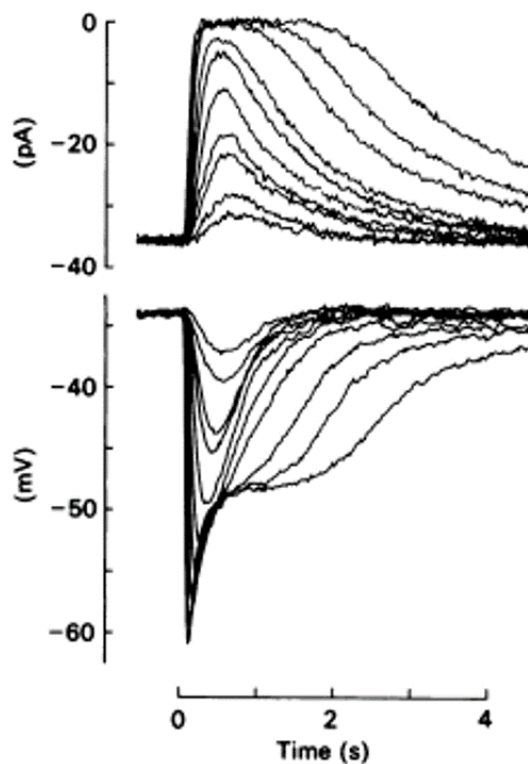
Figure 1.7 Electrical response of an isolated rod photoreceptor**.**
Upper panel: The transient suppression of the current entering the outer segment in response to 20 ms flashes of light of progressively increasing intensity, is recorded with a suction pipette;
Lower panel: simultaneous voltage recording with an intracellular microelectrode impaling the inner segment.

1.6.3 Enzymatic Cascade Inactivation

In order to maintain enough light sensitivity to respond to subsequent stimuli, it is essential for the photoreceptor to recover from its active state. This implies that all the molecules activated during the cascade need to be inactivated, and the cGMP concentration has to be restored. Transducin possess GTPase activity and is able to inactivate itself by hydrolyzing the bound GTP molecule into GDP, thus switching off also the PDE activity. At the same time *Rh** becomes a target for phosphorylation by a rhodopsin kinase, which phosphorylates the C-terminus of *Rh**. The phosphorylated Rh* then interacts with the protein arrestin, leading to its rapid inactivation and causing the dissociation of the all-*trans* retinal from the rhodopsin. In order to be restored into its 11-*cis* active form, the all-*trans* retinal is reduced to all-*trans* retinol, transported out of the OS and converted in the RPE by appropriate enzymes (Lamb and Pugh, 2004).

Theoretically, once the PDE activity has been reduced, the restoration of the dark levels of cGMP would occur thanks to the basal activity of GC. In this case, however, the recovery rate would be too slow compare with the photoresponse kinetics: indeed, more mechanisms that regulate the transduction cascade must be involved. It is now well established that the responsible for the modulation of the photoresponse cascade is primarily, if not exclusively, the change of Ca^{2+} intracellular free concentration (Rispoli, 1998; Fain et al., 2001; Nakatani et al., 2002).

## 1.6.4 Ca^{2+}-Mediated Light Adaptation

In order to adjust their sensitivity to different light intensities, photoreceptors are endowed with several mechanisms of light adaptation. In particular, these processes operate to increase the sensitivity of the transduction cascade in low-light conditions; whereas at higher levels of illumination the sensitivity decreases, preventing the receptors from saturating. The concentration of Ca^{2+} ions in the OS appears to play a key role in the light adaptation of photoreceptors, and it is also involved in the shut-off mechanisms described above (Fain et al., 2001; Nakatani et al., 2002). The most important Ca^{2+}-sensor proteins involved in these mechanisms are recoverin (Rec), calmodulin, and guanylate cyclase-activating proteins (GCAPs). Recoverin plays a role in the inactivation of Rh*, since it activates the rhodopsin kinase when Ca^{2+} concentration decreases. Calmodulin, on the other hand, modulates the cGMP-gated channels. In darkness, when OS free-Ca^{2+} is high, Ca^{2+}-calmodulin is bound to the channels, and their affinity for cGMP is relatively low. As Ca^{2+} concentration decreases in light, calmodulin unbind Ca^{2+} and dissociates from the channels increasing their sensitivity to cGMP. Low Ca^{2+} concentration induces also the GCAPs to activate another enzyme, the guanylate cyclase (GC), thus promoting the cGMP recovery when the light stimulation is ceased. The regulation mediated by GCAP is the most powerful negative-feedback mechanisms triggered by Ca^{2+} in photoreceptors, since it has an effect on the photoresponse amplitude, on the recovery phase of the photoresponse, and also improve the signal-to-noise characteristics of the rod.

Guanylate Cyclase-Activating Proteins (GCAPs)

GCAPs are members of the neuronal calcium sensor protein family, a group of Ca^{2+}-binding proteins that are mainly expressed in neurons, where they mediate a wide range of Ca^{2+}-dependent physiological responses (Burgoyne, 2007). The first observation that low Ca^{2+} concentrations in the OS stimulate the synthesis of cGMP was made in 1982 by Lolley and Racz, who conclude that Ca^{2+} has an inhibitory effect on GC (Lolley and Racz, 1982). Later, Koch and Stryer discovered that the activation of GC is not directly controlled by Ca^{2+} ions, rather is mediated by a specific Ca^{2+}-sensitive protein (Koch and Stryer, 1988). This protein had been finally isolated

after several years of efforts by Gorczyca et al., and was called guanylate cyclase-activated protein, or GCAP (Gorczyca et al., 1994).

From a structural point of view, GCAP are small proteins of approximately 200 amino acids, and contain four Ca^{2+}-binding domains (of which the first is non-functional) which are termed EF-hand motifs (Figure 1.8) (Ermilov et al., 2001). GCAPs are expressed in photoreceptors of several vertebrates, and many isoforms have been specifically found in human, bovine, mice, chicken, fish, and amphibians (Palczewski et al., 1994; Subbaraya et al., 1994; Frins et al., 1996; Imanishi et al., 2004).
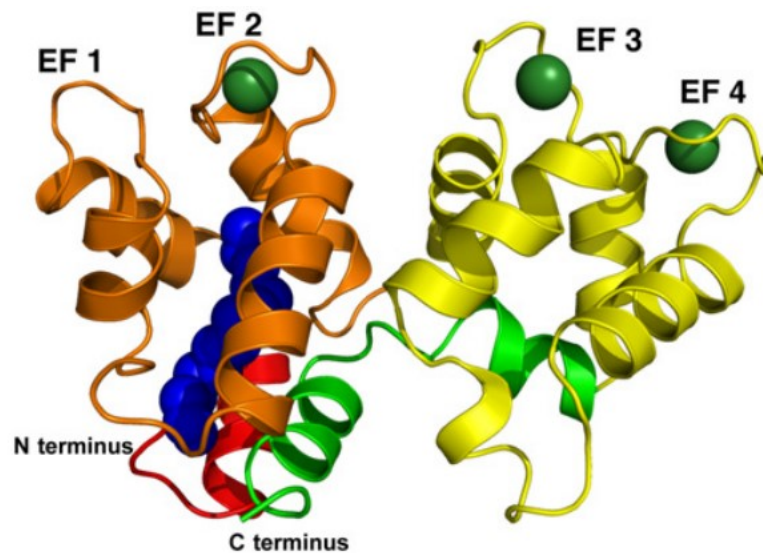
Figure 1.8
Cartoon representation of GCAP1 with three Ca^{2+} bound. The N-terminal helix is red, N-terminal domain (EF-1 and EF-2) is orange, C-terminal domain (EF-3 and EF-4) is yellow, kinked C-terminal helix is green, and the Ca^{2+} ions are shown as dark green space-filling spheres (modified from Stephen et al., 2007).

The physiological role of GCAPs in the modulation of the photoresponse has been deeply studied during the last years. Mendez and Chen generated a transgenic mouse strain having the genes of the isoforms GCAP1 and GCAP2 knocked-out (GCAPs^{-/-}) (Mendez and Chen, 2002). By comparing the flash responses recorded from rods of normal mice (GCAPs^{+/+}) with the ones in GCAPs^{-/-}, they discovered that responses triggered by flashes of same intensity were larger and slower in GCAPs^{-/-}. This indicates that the prevention of GCAP regulation in photoreceptors makes them more sensitive to light and unable to quickly recover their dark state following light stimuli, and adapt to background illumination.

Zebrafish GCAP

Within the last decade, the zebrafish (*Danio rerio*) has become a common and valuable vertebrate model in many branches of neuroscience, including embryology (Kimmel, 1993), developmental neuroscience (Barinaga, 1990), genetic analysis (Driever et al., 1994), and, of course, visual neuroscience (Bilotta and Saszik, 2001). The zebrafish retina is endowed with one type of rod cell

and four types of cone cells: short single cones (UV-sensitive), long single cones (blue-sensitive), and double cones (green- and red-sensitive). An interesting feature of zebrafish photoreceptors is the presence of six GCAPs isoforms, zGCAP1-6, which are expressed differently in rods and cones (Figure 1.9). Isoforms of zGCAP differ in their Ca^{2+} sensitivity and Ca^{2+}-activating properties (Scholten and Koch, 2011). Compared with mammals, which express only two types of GCAP, the abundance of these proteins in zebrafish photoreceptors suggests a more intricate mechanism for the regulation of GC and for the photoresponse in general that is not understood yet (Koch, 2013).

Level of expression	zGCAP isoforms		
HIGH	zGCAP3 zGCAP4 zGCAP5	zGCAP3 zGCAP4 zGCAP5	zGCAP1 zGCAP2 zGCAP3 zGCAP5
LOW	/	/	zGCAP4
FAINT	zGCAP7	zGCAP7	zGCAP7

double cones   long single cones   short single cones
(red/green-sensitive) (blue-sensitive)   (UV-sensitive)

Figure 1.9 Schematic summary of zGCAP expression in different type of cones.
Upper table: comparison of the expression profiles of zGCAP isoforms among the different type of cones.
Lower part: schematic design of double cones (LWS and MWS), long single cones (SWS) and short single cones (UV-sensitive).

1.7 Aim of This Work (pt. II): Role of zGCAP3 in Green-Sensitive Cones

Among all the GCAP isoforms expressed in zebrafish cone cells, the zGCAP3 is a major regulator of GC activity (Rätscho et al., 2009). For this reason, its physiological function have been investigated in the last years, by using different approaches. Expression pattern and localization analysis revealed that zGCAP3 is expressed only in cone cells, and prominently expressed in the larval retina (Imanishi et al., 2004; Fries et al., 2013). Furthermore, phylogenetic analysis have shown that this isoform has a strong relationship with human GCAPs, while biochemical assays were carried out in order to study zGCAP3 affinity with GC (Imanishi et al., 2004; Fries et al., 2012).

In the second part of this thesis work I investigated the role of zGCAP3 in the photoresponse cascade, employing a novel technique developed during my Ph.D. (Aquila et al., 2014). This technique allows the simulation of an over expression and a knock-down of this protein, by delivering it, or its monoclonal antibody, respectively, into an isolated zebrafish cone, while recording their photoresponses with the patch-clamp technique. The intracellular delivery of zGCAP3 and of its antibody was attained by ejecting them out of a tube inserted in the patch pipette lumen. A custom microperfusion system (see *Materials and Methods*) was employed to apply the exogenous molecules with a precise timing. However, the long tapered shape of the final part of the patch pipette, called shank, makes it very difficult to perfuse efficiently the cell with this strategy. For this reason, a pressure polishing setup has been assembled to enlarge the patch pipette shank, through the calibrated combination of heat and air pressure, that allowed to insert teflon tubes in the pipette lumen very close to its tip.

2. Materials and Methods

2.1 Peptides and Proteins

2.1.1 AMPs and CPPs

The primary structure of all peptides studied in this thesis is reported in Table 2.1.

CM_{18}-Tat_{11}, CM_{18}, and Tat_{11} peptides were synthesized and purified by the group of prof. Beltram of NEST laboratory (*Scuola Normale Superiore* and *Istituto Nanoscienze-CNR*, Pisa). CM_{12} was designed, synthesized and purified by Maccari et al. at NEST and IIT (*Istituto Italiano di Tecnologia*) laboratory in Pisa. These peptides were dissolved in bidistilled water to get a 500 µM stock solution and stored at −80 °C. Alm F50/5 and its analog [L-Glu(OMe)[7,18,19]] were dissolved in methanol to get different stock solutions and stored at −80 °C. For the experiments, an aliquot of the stock solution was dissolved in the perfusion solution to get a specific final concentration, and used within 30 minutes. Control experiments proved that the methanol contamination of the perfusion solution was no larger than 10 µl/ml and did not cause any non-specific membrane permeabilization (data not shown).

Table 2.1
Primary sequence of the peptides studied.

Peptide	Sequence
CM_{18}-Tat_{11}	Ac-KWKLFKKIGAVLKVLTTGYGRKKRRQRRRC-CONH2
CM_{18}	Ac-KWKLFKKIGAVLKVLTTG-CONH2
CM_{12}	Ac-WKLFLKAVKKLL-CONH2
Tat_{11}	Ac-YGRKKRRQRRR-CONH2
Alm F50/5	Ac-UPUAUAQUVUGLUPVUUQQ-Phol
[L-Glu(OMe)[7,18,19]]	Ac-UPUAUAEUVUGLUPVUUEE-Phol

2.1.2 zGCAP3 and IgG1 Monoclonal Antibodies

Recombinant zGCAP3 (and its dansylated version) was purified from BL21 *Escherichia coli* cells overexpressing the protein, following known protocols (Behnen et al., 2009; Scholten and Koch, 2011; Fries et al., 2012). IgG1 monoclonal antibodies (zG3 7E6-1-1; zG3 6G9-14; zG3 4C12-1-1; zG3 6B9-11) directed against purified recombinant zGCAP3, were produced in the laboratory of Dr. Elisabeth Kremmer (Institute of Molecular Immunology, Helmholtz Zentrum München, Munich,Germany) using rabbits for immunization. IgG1 antibodies were raised against a synthetic peptide corresponding to the last 20 amino acids (168-188) of the C-terminus of zGCAP3 (C-KMMDLTHVLEIIVNGQKKKKE).

2.2 Solutions

All chemicals, medium, and buffers were purchased from Sigma-Aldrich (St. Louis, MO, USA).

Rod outer segments from *Rana esculenta* and cone cells from zebrafish were bathed in a Ringer's solution having the following composition (in mM): 115 NaCl, 3 KCl, 10 HEPES (N-[2-hydroxyethyl]piperazine-N'-[2ethasulfonic acid]), 0.6 $MgCl_2$, 0.6 $MgSO_4$, 1.5 $CaCl_2$, and 10 glucose. Osmolality of all solutions was ≈ 265 mOsm/Kg and checked before experiment with an osmometer (Hermann Roebling, Messtechnik, Berlin, Germany). All solution were buffered to pH ≈ 7.6 (for *Rana esculenta*) and to pH ≈ 7.4 (for zebrafish) with NaOH or KOH.

In the experiments with AMPs and CPPs, the control solution, as well as the solution in which the peptides were dissolved, had the following composition (in mM): 130 KCl, 1 $CaCl_2$, and 10 HEPES; buffered to pH ≈ 7.6 with KOH. The osmolality was corrected with sucrose to ≈ 260 mOsm/Kg in whole-cell recordings from OS, to ≈ 290 mOsm/Kg in whole-cell recordings from CHO-K1, and ≈ 300 mOsm in excised-patch recordings from GUVs.

For the whole-cell recordings from zebrafish cone cells, patch pipette were filled with an intracellular solution containing (in mM): 40 KCl, 70 K-Aspartate, 5 $MgCl_2$, 1 GTP, 5 ATP, 5 HEPES; buffered to pH ≈ 7.4 with KOH. zGCAP3 and its specific antibodies were dissolved in the intracellular solution at a concentration of 40 μM and 6 μM, respectively.

2.3 Cell Preparation

2.3.1 CHO Culture

Chinese Hamster Ovary (CHO-K1) cells were purchased from the American Type Culture Collection (CCL-61 ATCC). CHO-K1 were grown in 25 ml flask (Falcon, Becton Dickinson and Company; Franklin Lakes, NJ) in DMEM/F-12 medium (Dulbecco's Modified Eagle's Medium; Gibco® by Life Technologies) supplemented with 10% fetal bovine serum and 1% penicillin/streptomicin (PenStrep, Bio Whittaker Europe, Cambrex Company, Verviers Belgium). Cell cultures were stored in humidified environment at 37 °C and in 5% CO_2, according to manufacturer's instructions. For patch-clamp experiments, cells were washed three times in phosphate buffered saline buffer (PBS, Gibco® by Life Technologies) to remove medium residues and detached from plate by trypsination for 5 min in 0.25% trypsin-EDTA solution (Gibco® by Life Technologies). Subsequently, 1-2 ml of DMEM/F-12 were added in order to inactivate trypsin enzyme and the cell suspension obtained is transferred in a 15 ml tube with others 2-3 ml of medium. Approximately 1 ml of the suspension was then centrifuged at 6,000 rpm for 30-40 sec, and cell pellet dissolved in PBS for patch-clamp experiment.

2.3.2 Photoreceptor Isolation

All experiments using animals were performed in accordance with the European Communities Council Directive for animal use in science (86/609/EEC) and approved by a local ethical committee. The experimental processes were designed to minimize animal number and suffering of the animals used.

Rod outer segments used in the single channel studies with Alm and [L-Glu(OMe)[7,18,19]] were mechanically isolated from the retina of *Rana esculenta*. Animals were kept in filtered, running tap water in small tanks at room temperature (20-23 °C).

Cone cells used in the study of zGCAP3 were mechanically isolated from the retina of *Danio rerio* (zebrafish). Adult zebrafish were kept in groups of 8-10 individuals in 50 liters aquaria with dechlorinated fresh water, continuously filtered and aerated, at constant temperature (28 °C) and maintained in a natural dark-light cycle.

Before dissection, both frogs and zebrafish were dark adapted for ~2 hour at room temperature, deeply anaesthetized by immersion in tricaine methane sulphonate solution (1 g/l in water) and decapitated in dim red light generated by LEDs of wavelengths of 660 nm. The eyeballs of *Rana esculenta* were removed from the head and hemisected in a Petri dish containing Ringer solution (see *Solutions*). The back half of the eyeball was cut into four pieces that were stored in the same oxygenated Ringer solution. The retina was peeled from an eyecup piece and gently triturated in 1-2 ml of Ringer solution, using a fire-polished Pasteur pipette to separate the rod outer segments. Since zebrafish eyes are smaller than the ones of *Rana esculenta* and in order to operate in completely dark conditions, cone cells of zebrafish were collected using a different method. After decapitation, the head was swiftly immersed in a Petri dish containing Ringer solution and transferred in a fully darkened box equipped with an infrared light (LEDs wavelength: 940 nm) and an HD webcam that had its infrared filter removed, connected to an external laptop. After inserting the hands through two light-tight holes of the box, the cornea of each eye was focused on the laptop computer screen and it was cut with small scissors. The retina was then gently sucked using a 200 µl precision pipette, by displacing the crystalline with the pipette tip. The two retinae were then ejected directly in the recording chamber and mechanically triturated with the same pipette.

2.3.3 Cell Viewing

An aliquot of ~2 ml of the appropriate solution containing the cells was transferred to the recording chamber placed on the microscope (TE 300, Nikon, Tokyo, Japan) stage. The preparation was illuminated with an ultra-bright infrared LED (900 nm) and focused on a fast digital camera (C6790-81, Hamamatsu Photonics, Tokyo, Japan) coupled to the microscope. The preparation was then viewed on a pc-monitor using the AquaCosmos software package (version 2.5.3.0,

Hamamatsu Photonics), which controls also all the camera parameters (like gain, exposition time, binning, etc.).

2.4   GUVs Electroformation

All phospholipids and cholesterol were purchased from Avanti Polar Lipids (Alabaster, AL, USA); chloroform and methanol were purchased from Sigma-Aldrich (St. Louis, MO, USA).

Giant unilamellar vesicles (GUVs) were prepared using the electroformation method (Angelova and Dimitrov, 1986; Estes and Mayer, 2005).

The composition of the lipid mix was: 60% egg-phosphatidylcholine, 10% egg-phosphatidylglycerol, 30% cholesterol, and 0.2% NBD-labeled phosphatidylethanolamine. The lipids were dissolved in a chloroform/methanol (95:5) mixture to obtain a final lipid density of 1 mg/ml. A 10 μl droplet of this lipid mix was spread on the charged side of an indium tin oxide (ITO) coated glass slide, using a Hamilton syringe and under a light stream of argon. The solvent was then completely evaporated under vacuum for at least 2 h. After this time, a thin lipid film was formed on the surface of the glass slide. A silicon spacer is then placed on the slide around the lipid film, and the electroformation chamber was closed using a second ITO-coated glass slide. The chamber was then closed with rubber bands or Parafilm and filled with a 300 mM sucrose solution. For the electroformation, a 1.5 V, 10 Hz potential was applied for 1 h, and then switched to 4 V, 4 Hz for 15 min to promote detachment of GUVs from the glass surface. The solution containing GUVs (~500 μl) was gently removed with a syringe from the electroformation chamber, diluted in a solution containing 130 mM KCl and 1 mM $CaCl_2$, and placed in the recording chamber under the microscope to check their formation and unilamellarity.

2.5   The Patch-Clamp Technique

The patch-clamp is a technique used for the first time by Neher and Sakmann (for which they received the Nobel Prize in 1991) that allows high-resolution recording of the ionic currents flowing through a cell membrane (Neher and Sakmann, 1976; Neher et al., 1978). The principle of this method, specifically of the voltage-clamp mode, is to electrically isolate a small part of the membrane (patch) and to measure the current necessary to maintain the membrane potential equal to that of the command circuit (Hamill et al., 1981). The membrane patch isolation is achieved by pressing the clean, smooth tip of a glass micropipette, which is filled with an isotonic saline solution, on the surface of the cell membrane and applying light suction (Figure 2.1). Under such conditions, the adhesion between the pipette and the membrane (called seal) is so tight that

the electrical resistance is greater than 1 GΩ. This high seal resistance reduces the current noise of the recording and allows a good resolution of single channel currents, whose amplitude is in the order of pA.
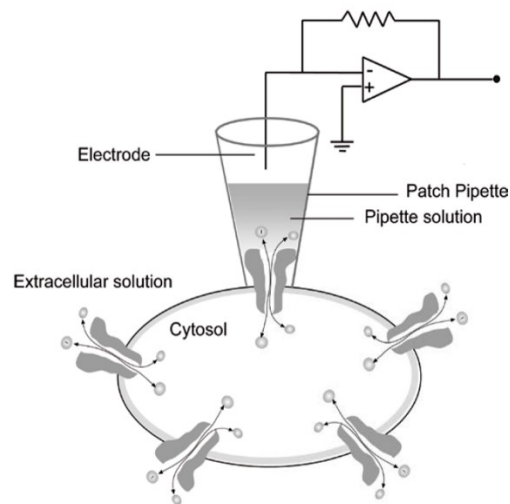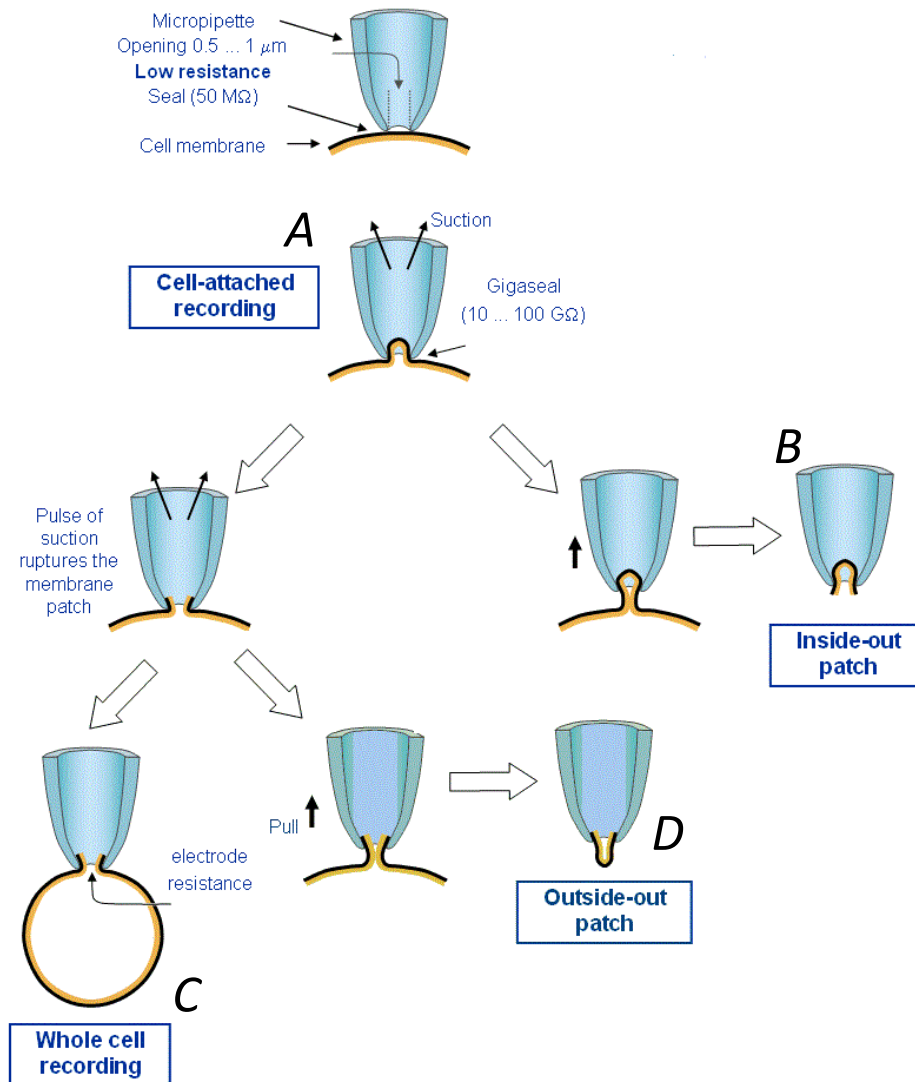

Figure 2.1
Schematic diagram of the patch-clamp technique.

2.5.1 Patch-Clamp Configurations

Depending on the type of experiment needed, different configurations of the patch-clamp technique can be used (Figure 2.2). The cell-attached configuration is simply achieved once the seal is formed, and allows recording of currents flowing through single ion channels enclosed by the pipette tip of the intact cell (Figure 2.2*A*). Once the cell-attached configuration is obtained, the micropipette can be quickly detached from the cell, thus breaking a patch of membrane that remains attached to the tip of the pipette. In this case, called inside-out configuration (Figure 2.2*B*), the intracellular side of the membrane is exposed to the external solution, which can be manipulated by the experimenter. The whole-cell configuration (Figure 2.2*C*) is achieved from the cell-attached by perforating the membrane patch through the application of negative pressure. Under this condition, the solution of the pipette enters into the cytoplasm, and the current flowing through the entire cell surface can be recorded. The whole-cell configuration has been used in experiments with OS, CHO-K1, and cone cells, but could not be used for recordings from GUVs, too fragile, for which was used the inside-out excised-patch configuration.

In the outside-out configuration (Figure 2.2*D*), once the whole-cell is obtained, the pipette is slowly withdrawn from the cell so that the patch of the membrane detaches from the cell and turns into a convex membrane, with the original outside of the membrane expose to the bath solution. Outside-out patch-clamp allows to examine the properties of an ion channel exposed to different analytes on the extracellular side.

Figure 2.2 Different patch-clamp configurations. *A*, cell-attached; *B*, inside-out; *C,* whole-cell; *D*, outside-out.

2.5.2 Patch-Clamp Setup and Data Analysis

The current was recorded employing a patch-clamp amplifier (Axopatch 200B; Molecular Devices, Sunnyvale, CA, USA). Recordings were usually filtered at 2 kHz via an eight-pole Butterworth filter (VBF/8 Kemo, Beckenham, UK), sampled on-line at 5 kHz by a Digidata 1322A (Molecular Devices) connected to the SCSI port of a Pentium computer running the pClamp 10.0 software package (Molecular Devices), and stored on disk. Data were further low-pass filtered off-line at 100, 200 or 500 Hz using a Gaussian filter, or by using the running average routine of SigmaPlot (version 8.0; Jandel Scientific, San Rafael, CA, USA), and analyzed using Clampfit (version 10.0; Molecular Devices). Figures and statistics were performed using SigmaPlot; results are given as means ± SEM.

2.6 Pressure Polish Technique

When performing whole-cell experiments, the patch pipette tapered shank (i.e. the final part of the pipette) and the small tip opening give high resistance to the passage of ions and molecules and preclude efficient exchange between pipette solution and cell cytosol. This resistance can be measured electrically, and it is called access resistance (R_a). Moreover, to faithfully record large currents (elicited by high concentrations of peptides and/or highly membrane permeabilizing ones), it is necessary to minimize R_a, in order to reduce errors in membrane potential control and time constant of charging the cell membrane capacitance.

During my Ph.D. a new method to enlarge the pipette shank without affecting the tip-opening diameter has been improved, using the calibrated combination of heat and air pressure (Aquila et al., 2014). These pipettes, called "pressure-polished" pipettes, gave small access resistances, and allowed the accommodation of plastic perfusion tubes very close to the pipette tip (see *Intracellular Perfusion* section).

2.6.1 Pressure Polish Setup

Patch pipettes were pulled from 50 or 100 μl borosilicate glass capillary (Drummond, Broomall, PA, USA) using a vertical puller (Narishige PP-830, Tokyo, Japan). The pipettes obtained were tightened into a modified pipette holder connected to a pressurized air line (set to 4 atm and filtered with a 0.2 μm filter) through a three way valve (Figure 2.3).
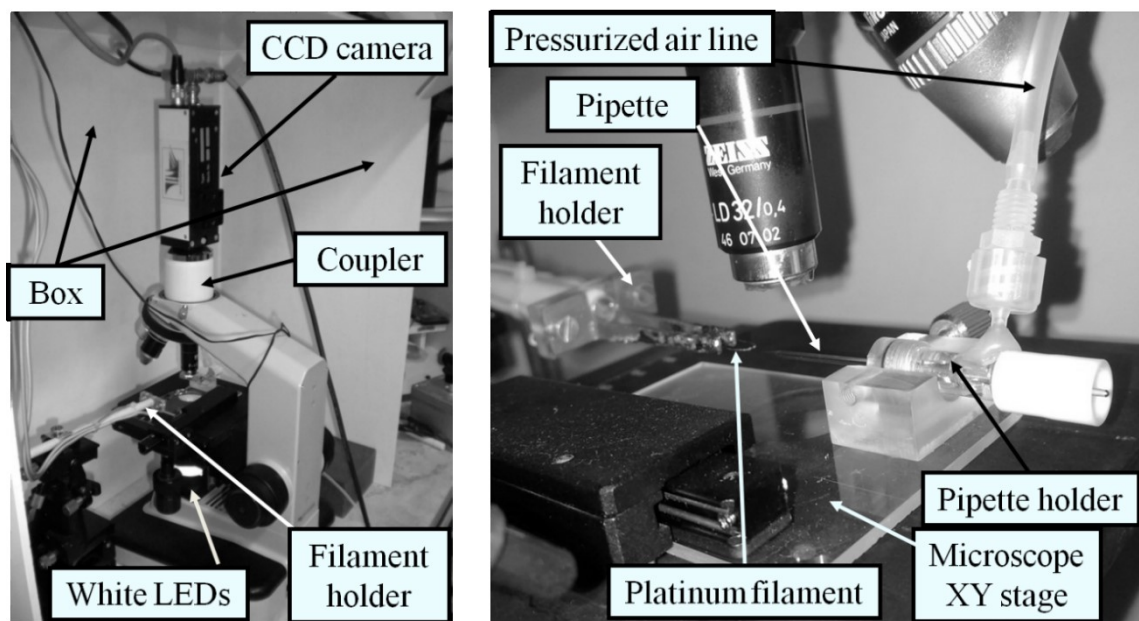
Figure 2.3 Setup to fabricate pressure-polished pipettes. *Left*, view of the microscope, the camera coupled to the objective nosepiece, the microscope stage, the filament holder, the LED illuminator, and the box; *right*, closer view of the microscope stage, the pressurized pipette holder, and the platinum filament.

The holder was clamped to a microscope stage and moved using the XY manipulator to center the pipette tip into the central bend of a platinum filament shaped in the form of an omega (Figure 2.4) by using a needle of a 1 ml syringe and fine forceps. Thanks to this particular shape, the pipette shank was homogeneous softened when a constant current pass through the filament heating it. To avoid metal evaporation onto the pipette, the filament (50 μm of diameter) was previously uniformly glass-coated by dipping it in borosilicate glass powder while it was heated to red color. The filament was then tin soldered to two copper bars connected to form a holder (Figure 2.4), and mechanically coupled to a micromanipulator that allowed a precise positioning of the filament under the microscope. Finally, a variable high-current generator was remotely connected (or not) to the filament by a "push-to-make" switch.

To follow the pressure polish process, it was necessary to view it on a LCD monitor: to this aim, the eyepiece of the microscope (YS2-T, Nikon) was removed, and a contrast-intensified CCD camera (VX 44, Till Photonics, Gräfelfing, Germany) was coupled to the objective nosepiece through an ocular, a 0.6 neutral density filter and an infrared filter. The video signal could be recorded by digitizing it on-line (by Pinnacle Studio MovieBox DV, Avid, Burlington, MA, USA), stored on a computer, and further processed off-line. The pressure polish setup was enclosed in a box to avoid
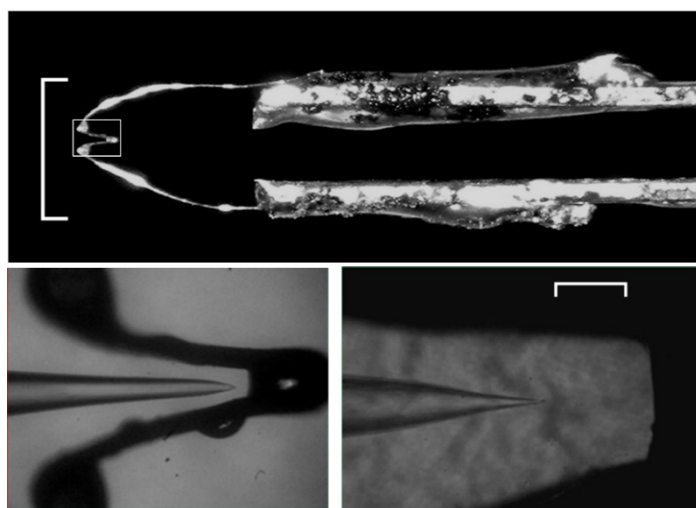
Figure 2.4 Filament shape and pipette alignment. *Top*, Shape of the glass-coated platinum filament tin-soldered to the holder; *scale bar* 5 mm. The region within the *white box* is enlarged at *bottom left*. The omega-shaped region of the filament is enlarged at *bottom right*, pipette correctly aligned with the filament before pressure polishing; scale bar: 100 μm.

any changes in the filament temperature caused by air currents (which could strongly affect its temperature), and to protect the entire setup from dust.

2.6.2 Pressure Polish Procedure

Once the pipette is properly aligned with the filament, the three-way valve was set to connect the pipette lumen to the pressurized air line. The current generator was then turn on using the "push-to-make" switch and keep it on, while following the shaping process of the pipette shank on the LCD monitor, until the desired shape is attain (Figure 2.5).

The pressure procedure was controlled by five parameters listed below:

a) the position of the pipette relatively to the omega-shaped, glass-coated platinum filament;

b) the intensity of the current flowing in the filament (typically set to ~1.2 A);

c) the duration of this current flow;

d) the intensity of the pressure applied in the pipette lumen (~4 atm);

e) the duration of this pressure application as the current is flowing in the filament.
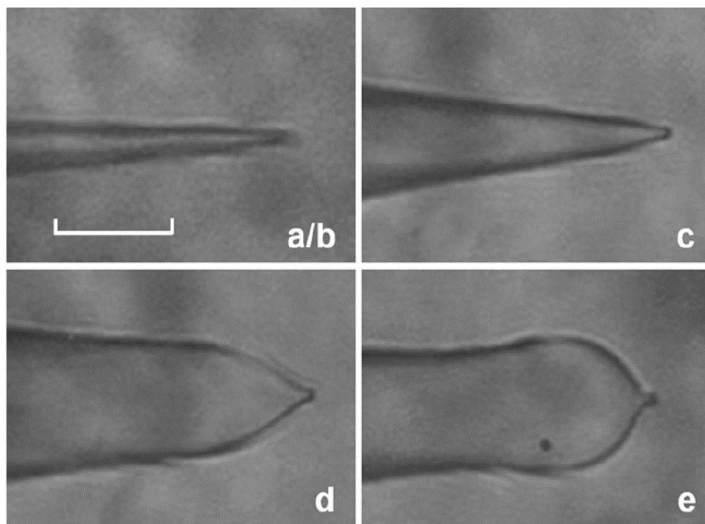
Figure 2.5
Different pipette shanks obtained with the pressure fire polishing. *a,* pulled pipette; *b,* the same pipette fire polished without pressure (indistinguishable from the pulled one at this magnification); *c–e,* pulled pipettes similar to *a*, fire polished with progressively longer pressure durations. Scale bar: 20 μm.

The most simple and efficient strategy to finely shape the shank profile and the tip opening section was to optimize and keep fixed the parameters a, b, and d while the c and e ones were adjusted each time in order to obtain the desired pipette geometry (Figure 2.5) and tip-opening diameter. Anyway, the fixed parameters had to be controlled every time the filament was changed (about every two/three months, or when the filament was compromised), because the correct positioning, as well as the intensity of current and air pressure could vary according to the length and shape of the filament.

2.6.3 Intracellular Perfusion

In respect to conventional pipettes, the pressure-polished ones provided a dramatic improvement of the electrical recordings, given by the huge access resistance decrease, and they doubled the rate of molecular diffusion between the pipette and the cell interior. This substantial improvement in cell dialysis allowed the perfusion of small molecules in the cytosol, permitting the modulation of a multitude of intracellular processes during the whole-cell recording. However, many substances that had to be delivered in the cell (especially proteogenic ones) cannot be added

directly into the pipette solution because they may stick to the glass tip and reduce the probability or even prevent the seal formation (Mathias et al., 1990). In these cases, it is required to add these molecules to the pipette solution at a desired time, at least any time after attaining the seal. It is anyway extremely important to control the intracellular delivery even of these molecules not affecting the seal formation, for instance when some control experiments need to be performed on the same cell before the delivery. This task can be accomplished by inserting a teflon tube inside the pipette lumen, filled with a solution containing the molecule under test that can thus be ejected into the pipette solution with a pulse of pressure applied to the tube lumen. Pressure-polished pipette resulted to be very advantageous for this goal. The tubes could in fact be accommodated very close to the tip of these pipettes fabricated with a particularly enlarged shank: this would minimize the delay between the time when molecules were expelled out of the tube, and the time when they were in fact incorporated in the cell cytosol. Indeed, the enlarged pipette shank allowed the smallest teflon tubes to advance x ≈ 95 μm further than the conventional pulled pipette (Figure 2.6).
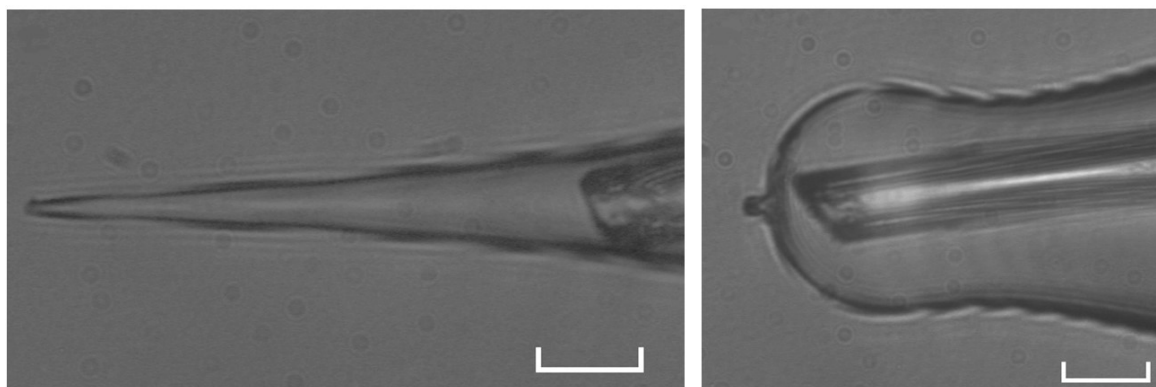

Figure 2.6 A teflon tube positioned inside the lumen of a conventional pipette as close as possible to its tip (*left*); the same tube is inserted in a pressure polished pipette (*right*). Scale bar : 20 μm.

In this way the perfusion delay (t) for a small protein (for instance with a diffusion coefficient D = 10^{-6} cm^2 s^{-1}) is reduced by about 15 s, according to the three-dimensional diffusion equation in the absence of pressure:

$$t = \frac{x^2}{6 \cdot D}$$

The other end of the teflon tube comes out of the pipette, and then out of the holder through a side-port. The expulsion of the solution from the tube to the pipette, and subsequently to the cell, is performed by applying a positive pressure inside the teflon tube (previously filled with the solution under test) using a precision pressure generator connected with a "three-way" valve with

low dead volume. This valve is also connected to a syringe containing the test solution, in order to guarantee a constant supply of the solution (Figure 2.7*C*).
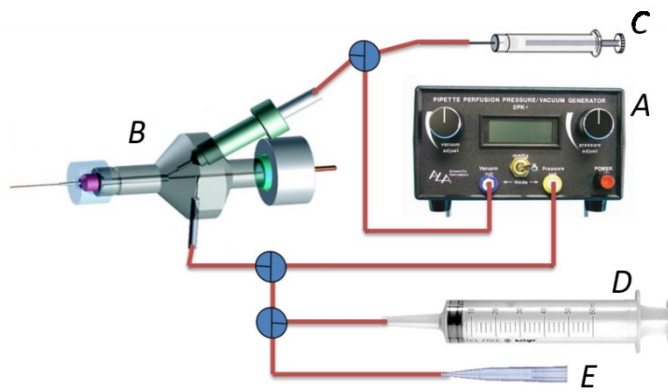
Figure 2.7 Intracellular perfusion apparatus. *A,* Pressure generator; *B,* pipette holder; *C,* precision syringe; *D,* 50 ml syringe used to apply strong positive pressure to clean the pipette; *E,* mouth piece used to gain the seal.

To test the efficacy of the perfusion system, the kinetics of lucifer yellow (40 μM, dissolved in intracellular solution) loading into a cone cell was recorded in whole-cell configuration with the pressure-polished pipette sealed on the outer segment (Figure 2.8*A*) or on the inner segment (Figure 2.8*C, upper panel*). The fluorescence intensity was integrated in three different regions of the cone (upper extremity of the OS, at the pipette level, and in the IS; *black*, *red*, and *green* dots, respectively), plotted vs time and then normalized. The fluorescence rose in all three regions with roughly similar kinetics, regardless the pipette was sealed on the inner or on the outer segment of the cone. In Figure 2.8*C*, lower left panel, is shown a fluorescence image after 50 s of injection in the outer segment of dansylated zGCAP3; the same cell is shown in bright field in the right panel.
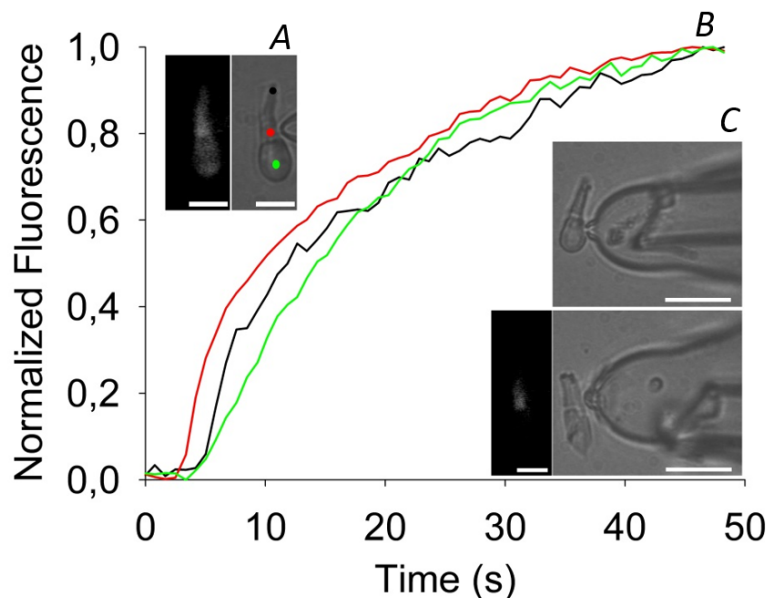
Figure 2.8 Kinetics of lucifer yellow 40 μM loading into a whole-cell recorded cone with the pressure-polished pipette. *A, left panel*, fluorescence image after 50 s of lucifer yellow perfusion of the cell shown in bright field on the right (seal on the OS). *B*, normalized fluorescence intensity integrated in the *black*, *green*, and *red* regions of *A* vs time; Lucifer yellow was injected at t = 0. *C, lower left panel*, fluorescence image after 50 s of injection in the OS of dansylated zGCAP3 of the cell shown in bright field in the right panel. Short white scale bars are 10 μm; long scale bars are 20 μm.

2.7 Fast Extracellular Perfusion

In order to quickly apply the peptides on the cell or GUV membranes, a fast extracellular perfusion system is used (Vedovato and Rispoli, 2007). After the desired patch-clamp configuration is obtained (whole-cell for CHO-K1 and OS frog, excised-patch for GUVs), the patch pipette is aligned in front of a fast microperfusion system (Figure 2.9). The perfusion pipette was created by gluing together six-barrels made with precision, square glass capillaries of 500 μm of side. This pipette can be moved horizontally in front of the patch-pipette with a precision step motor, controlled by a user-friendly interface running in a computer connected to the microperfusion system via a serial port. Peptides are applied and removed in ~50 ms (see below) by moving the perfusion pipette in front of the patch pipette. This enables us to rapidly switch recorded cell, or GUV patch, back and forth from a stream of control perfusion solution to a stream of control perfusion solution to a stream containing the tested peptide dissolved in the same perfusion solution. Such an experimental strategy allows to quantitatively describe membrane activity by measuring the kinetics of current change following both peptide application and withdrawal. Patch pipette are filled with the perfusion solution to ensure that current is entirely driven by the holding potential (V_h). In the control solution, repetitive 10 mV pulses are routinely applied to check access resistance (R_a) and membrane resistance (R_m) stability.
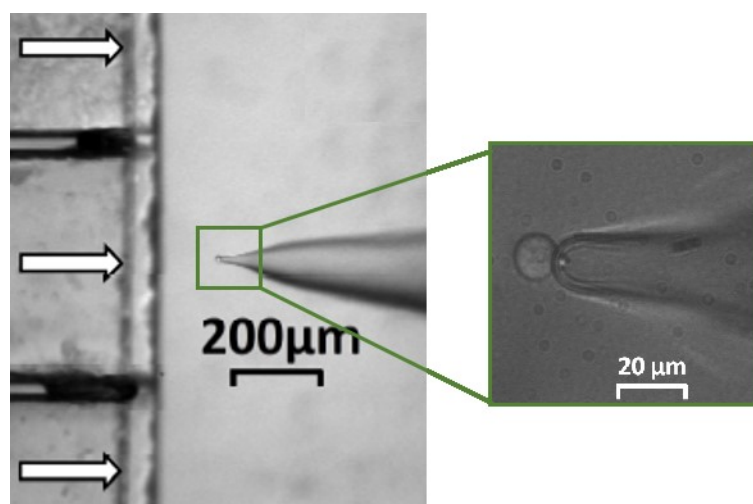
Figure 2.9 CHO-K1 cell recorded in whole-cell mode (shown enlarged in the *inset*) aligned in front of the multibarreled perfusion pipette (horizontal white arrows denote perfusion flows).

The solutions flowing in the perfusion pipette are fed by means of 1 ml precision syringes (Hamilton, Reno, NV, USA), whose piston is moved by a DC motor controlled via the computer interface. The typical perfusion speed is 15 μl/min, therefore minimal amounts of peptide solution

(<500 µl) are required to perform peptide applications lasting more than half an hour. Once the syringes are emptied, an end-position switch stop the motor, and the syringes can be refilled by clicking on the *Refill* button. This command moves the six three-way valves in the cylinder position and backs up the DC motor at full speed until the syringes are filled: the motor is then stopped by a second end-position switch.

When using particularly precious solutions (such as AMPs and CPPs), all the perfusion lines are filled with control solution and the connectors to the perfusion pipette were detached, connected to a needle and immersed in the vials containing the peptide solutions. The syringe motor is then set to *Reverse Mode* and the solutions fill just the terminal portion of the tube between the valve and the perfusion pipette. The connectors are then replaced and the motor is set to *Forward Mode* to apply the solution to the cell. At the end of the experiment, all the perfusion lines can be washed by dipping all the tubes previously dipped in the cylinders, into a container filled with distilled water (or other washing solution, such as ethanol, DMSO, sodium hypochlorite), and clicking the *Wash* button. This command activated the valves and moved the motor back and forth at full speed, so that the syringes are firstly emptied through the perfusion pipette and refilled with the wash solution, a number of times set by the user in a sub-window opened by the *Wash* button.

2.8 Light Stimulation and Calibration

Light stimuli (flashes in the dark and flashes on a background of light) were delivered on zebrafish cones using voltage protocols loaded on pClamp software (Molecular Devices, Sunnyvale, CA, USA). One of the two analogical outputs of the Digidata 1322A (Molecular Devices) was connected to a calibrated voltage-to-current converter driving an ultra-bright LED of a wavelength of 550 nm. The LED was mounted on a miniaturized *xyz* micromanipulator, coupled to the binocular port of the inverted microscope and aligned so to have its light spot automatically centred and in focus on the zebrafish cone. Contemporarily the cone was viewed in sharp focus through a 60x objective on the microscope camera using an ultra-bright infrared LED replacing the microscope illuminator. Enough space was left between the LED and the binocular port to host neutral density filters, when required; the LED positioning and the measure of its spot size, were performed with the following procedure. First, a particular subdivision of the grid of a calibrated microscope slide was focused and centered on the inverted microscope 60x objective, by using the microscope infrared LED. Then a straight microscope, mounted on a second *xyz* micromanipulator, was aligned to the inverted one, and it was moved so to have its 60x objective focused and centered on the same grid subdivision, by using the LED as a light source. The LED spot, observed with the straight microscope, was finally focused and centered with its *xyz* manipulator on the grid subdivision, and its geometry measured (it resulted a uniform disk of 300 µm of diameter). The microscope slide

42

was then replaced by the sensor (OP-2/LM-2 VIS, Coherent, Santa Clara, CA, USA) of a power/energy meter (Fieldmaster, Coherent), and the light power produced by the LED at all the voltages used in the experiments was measured. Voltages, neutral density filters and light stimulus duration were matched so to have a wide range of light intensities spanning more than 5 order of magnitude, with currents always falling in the LED linear range (1-10 mA).

To estimate the physical collecting area of the zebrafish cone outer segment (the functional collecting area cannot be estimated since cones do not detect single photons) it is necessary to know the quantum efficiency of photoisomerization and the specific axial rhodopsin density (Baylor et al., 1979). Moreover, it is difficult to have a reasonable estimate of the cone rod outer segment volume, since it is strongly invaginated, its geometry cannot be simply assimilated to a truncated cone, and its small dimension make it difficult to precisely measure the diameter of its base and of its tip. The geometrical area of the cone OS was measured on digital micrograph obtained with the camera (494x674 pixels, 0.2 µm per pixel), by using a freeware image analysis software (ImageJ, http://imagej.nih.gov/ij/) and it resulted 15.3 ± 3.9 µm^2 (n = 20). Using the ratio between the geometrical rod outer segment area and the collecting area of ~0.062 calculated by Baylor et al. in 1979, it can be roughly estimated that the zebrafish cone collecting area is ~1 µm^2 (Baylor et al., 1979). If this line of reasoning proves to be correct, then the numerical values of the flash intensities reported throughout the paper (in photons/µm^2) are also the number of photons absorbed by the cone.

2.9   Fluorescence Imaging

Besides bright field viewing of the cells, the camera and the AquaCosmos software were employed for fluorescence imaging experiments as well. The excitation light was generated by a monochromator (Polychrome II, Till Photonics) coupled to the epifluorescence port of the microscope via an optical fiber. Solution and protein loading in the cell was checked by using zGCAP3 labeled with dansyl chloride (concentration: ~20 µM; excitation: 280 nm, emission: 400 to 600 nm) and with lucifer yellow (CH, dilithium salt; concentration 40 µM; excitation: 425 nm, emission: 528 nm), once the whole-cell configuration was gained. Dansylation of zGCAP3 (degree of dansylation: 16-22%) was performed as described in Fries et al., 2012. Incorporation of fluorescent zGCAP3 into the zebrafish cone cytosol (Figure 2.7) was rapid and sufficient to measure possible modifications of the photoresponse waveform induced by application of either purified zGCAP3 or an anti-zGCAP3 antibody.

3. Results and Discussions

Part I
Membrane Active Peptides:
Biophysical Characterization in Natural and Model Membranes

3.1   Electrical Properties of CHO-K1 Membrane

The mechanism of membrane permeabilization induced by the chimeric peptide CM_{18}-Tat_{11} are studied by perfusing this peptide (and its isolated moieties) on the membrane of the CHO-K1 cells (see *Materials and Methods*). This goal is achieved by recording the ion current through the channels formed by these peptides, once inserted in a cell plasma membrane. To avoid contamination by the cell membrane currents, all the endogenous current sources must be blocked, possibly without using any drug (such as tetrodotoxin, tetraethlylammonium, dihydropyridines, etc.) that could obstruct the peptide pores or interfere with the pore formation. In line with previous reports on CM_{18}-Tat_{11} (Salomone et al., 2012, 2013), we choose the CHO-K1 cell line as case study. Nicely, we find that, in symmetric ionic conditions, CHO-K1 cells have no voltage- and/or calcium- and/or time-dependent conductances, but only a very small background one.

Indeed, the current amplitude is time-independent and very small for any physiological voltage value (Figure 3.1*A*). We observed a linear (ohmic) current-to-voltage behavior (Figure 3.1*B*) and a membrane resistance (R_m) > 5 GΩ. Such high R_m values make it possible to measure current amplitudes as small as 1 pA in a bandwidth of at least 1 kHz (i.e., any exogenous peptide-induced current can be detected down to the single-channel level). Thanks to this high recording resolution, we set the holding potential (V_h) = −20 mV in order to limit the current amplitude induced by the strongly permeabilizing peptides while ensuring a detectable current through the weaker ones.
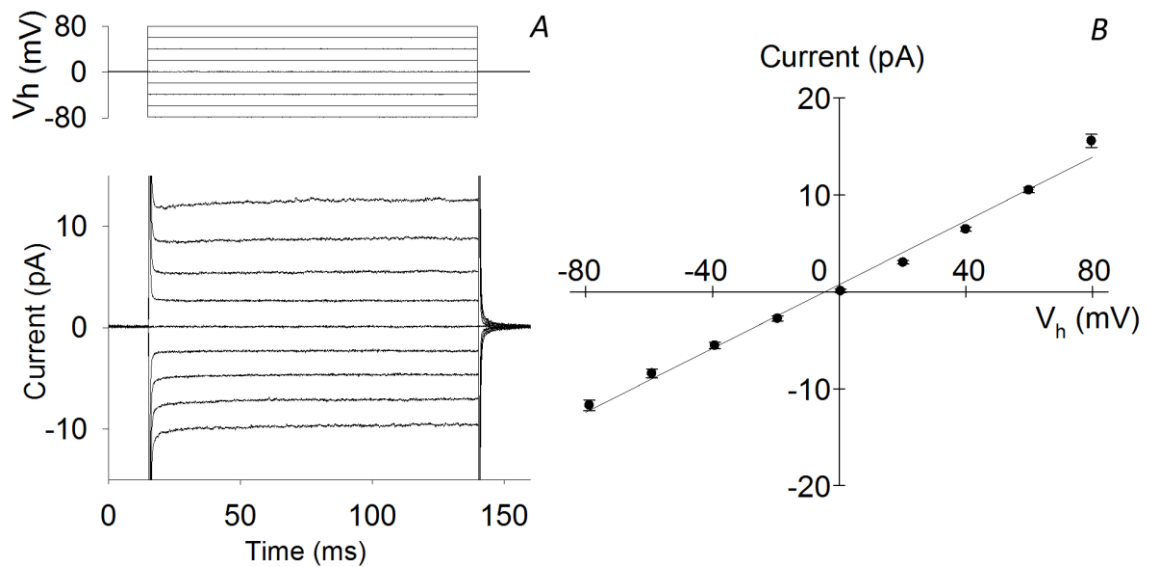
Figure 3.1 Biophysical characteristics of CHO.K1 membrane.
(*A*) Average whole-cell current recorded from representative cells (*lower panel*; pipette and external solution: 130 mM K^+ + 1 mM Ca^{2+})' subjected to 125 ms voltage steps from -80 mV to +80 mV in 20 mV increments (*top panel*) starting from V_h = 0 mV (traces are the average of n = 6 cells); (*B*) the average current evoked by each voltage step of *A* is plotted against the voltage step amplitude; the points are well fitted by a straight line (correlation coefficient ~0.99), whose angular coefficient gave R_m ~6.1 GΩ.

3.2   Peptide Activity Properties

My goal here is to employ the patch-clamp technique to study the mechanism of membrane permeabilization induced by the chimeric peptide CM_{18}-Tat_{11}, under strict physiological conditions. The patch-clamp technique allows to record the currents flowing through the pores formed by these peptides once they are inserted in a plasma membrane. With an appropriate analysis of these currents, it is possible to distinguish the mechanism of action used by the peptide under study.

In general, the waveform of the current induced by peptide application and removal can be described quantitatively using the following kinetics parameters:

a)   the *delay* of the activation, which represent the time lag between peptide application and the time in which the current deviates from its baseline more than three times the noise average fluctuation;

b)   the activation time constant (τ_a), defined as the time constant of the single exponential fit to current activation;

c)   the current amplitude at steady-state (I_{max});

d)   the deactivation time constant (τ_d), defined as the time constant of the single exponential fit to current deactivation (upon peptide removal).

To avoid any error produced by the noise, the above parameters were measured on low-pass filtered traces.

Since CM_{18}-Tat_{11} does contain a functional antimicrobial peptide (CM_{18}), it is conceivable that it may act by one of the three recognized mechanisms of membrane permeabilization proposed for this class of peptides, which are the "barrel-stave", the "toroidal", and the "carpet" model (see *Introduction, part I*).

The barrel-stave model requires that a certain number of monomers bind together once they get in contact with the plasma membrane and assemble to form an ion conductive pore. If the number of monomers inserted in the membrane is small, as it occurs at low concentrations of a peptide like gramicidin (Killian, 1992), it is expected that the pores form and disaggregate frequently, producing sustained single channel events. The application of larger peptide concentrations is likely to produce macroscopic currents that recover to zero after extracellular peptide removal, because the interaction between the membrane and the peptide monomers is not strong enough to keep the peptides stably inserted once the extracellular supply is ceased. Consequently, the kinetics of current activation and deactivation and its amplitude are expected to be constant at each peptide application.

In the case of the toroidal model, the molecular attractive forces between the polar head groups of the lipids and the peptides are so strong that the lipids are forced to tilt up and form pores whose walls are constituted by both lipids and peptide monomers. Such a strong interaction, however, is not expected to produce rapid pore formation and disaggregation at low peptide concentrations (i.e. sustained single-channels events), while larger peptide concentrations are expected to produce macroscopic currents with a *delay*, τ_a, and τ_d larger than in the case of the barrel-stave process. This is because of the longer time needed to form pores whose walls are not composed just by peptide monomers but by tilted lipids and peptides, and because of the longer time to disassemble this stable structure when extracellular peptide supply is ceased. If the peptide application is short and at low concentration, the monomers left on the membrane after peptide removal do not have a concentration large enough to give rise to conductive pores: these peptides may yet contribute to form additional pores once the peptide is applied again to the extracellular side. Therefore, repeated peptide applications are expected to elicit currents that only initially recover to the zero level upon peptide removal, and then produce a progressive acceleration of the current-activation kinetics (i.e., decrease of *delay* and τ_a), and a progressive increase of the steady-state current amplitude. This would eventually lead to the formation of stable conductive channels, which would produce progressively larger background currents upon peptide removal. All these features were previously observed with CM_{15}, a peptide well-known to form pores according to the toroidal model (Milani et al., 2009), and are therefore considered in the following as a "signature" of this particular permeabilization process.

48

Finally, the "signature" of the carpet mechanism is given by two main observables. The first one is a larger delay with respect to the one characterizing current activation in the toroidal and barrel-stave mechanisms, due to the expected slow process of micelle formation. The second one is the substantial irreversibility of the permeabilization process, caused by the membrane disruption in a detergent-like fashion, as observed in the case of viroporins (Madan et al., 2007).

In a characteristics measurement, isolated CHO-K1 were held at V_h, and R_m was checked before peptide delivery by means of a brief −10 mV step (Figures 3.2, 3.3, 3.5, *asterisks*). Furthermore, to simplify the interpretation of the experiments, patch pipettes were filled with the same perfusion solution (that typically contained 130 mM of KCl and 1 mM of $CaCl_2$) to ensure that the current was only driven by the holding potential (usually set to -20 mV). Various concentrations of CM_{18}-Tat_{11} (or CM_{18}, or Tat_{11}) were then delivered in ~50 ms using the fast-perfusion system. Once the peptide current was stable, the cell was quickly returned to the control solution (without peptide) to assess the possible current level recovery, and R_m was again measured. In the control solution, repetitive 10 mV pulses were routinely applied to check access resistance (R_a) stability (Figure 3.3, *triangles*), otherwise the recording was terminated.

3.3   Membrane-Disruptive Properties of CM_{18}-Tat_{11}

CM_{18}-Tat_{11} continuously applied for more than 1 min at various concentrations (0.5 µM, n = 2; 1.0 µM, n = 3; 2.0 µM, n = 4; 3.0 µM, n = 5) on the CHO-K1 membrane failed to elicit detectable currents down to single-channel events. A typical example is shown in Figure 3.2, *inset*, in which the current did not significantly deviate from the zero level following a ~100 s application of 3 µM CM_{18}-Tat_{11}. On the contrary, application of 4 µM CM_{18}-Tat_{11} elicited a current that developed in a roughly exponential trend ($\tau_a = 1.5 \pm 0.4$ s) up to a steady-state amplitude of 1.0 ± 0.2 nA (n = 15 cells) with a *delay* of 2.6 ± 0.5 s. As shown by the representative curve in Figure 3.2, the induced membrane permeabilization was extensive, as the evoked current did not fully recover to the baseline even after several seconds from peptide removal (see Figure 3.5 for more details). These recordings were very similar to the ones obtained with a viroporin-derived peptide (Madan et al., 2007), acting in a carpet-like fashion.
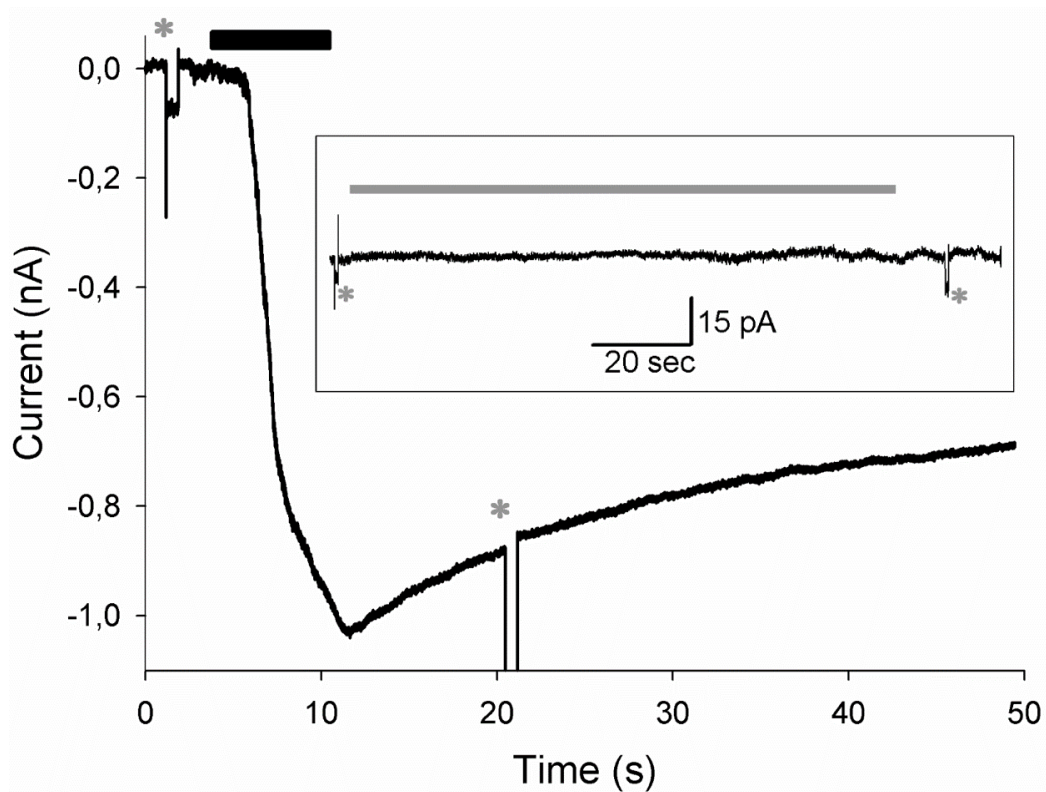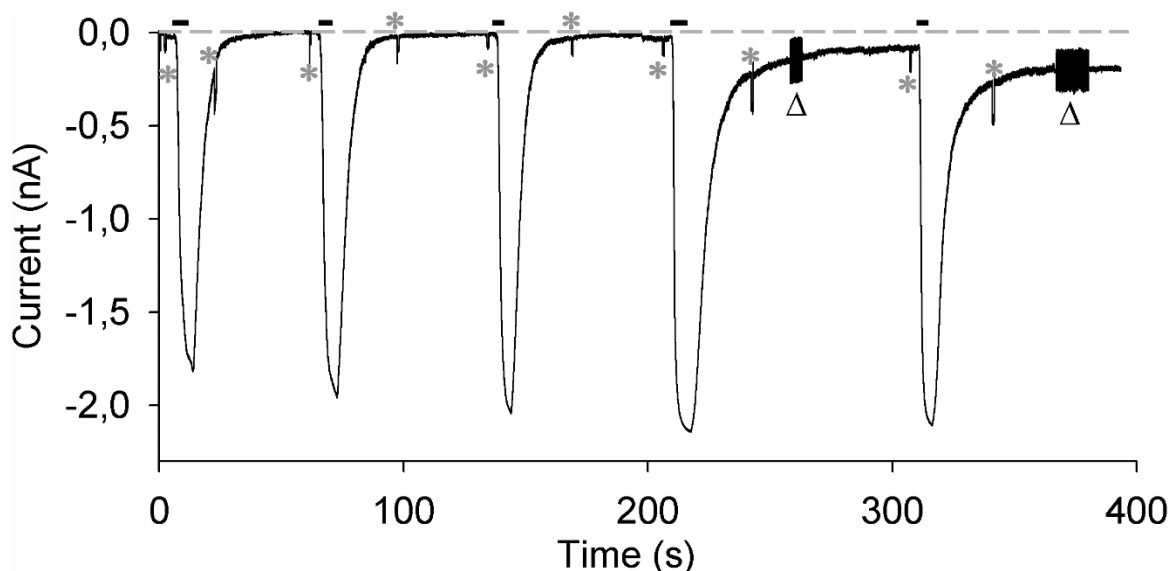

Figure 3.2 Whole-cell current recording elicited by the application of 4 µM CM_{18}-Tat_{11}.
Black bar: duration of peptide delivery (6.7 s).
Inset: 113 s (*grey bar*) application of 3 µM of CM_{18}-Tat_{11}; R_m was 1.3 GΩ before and 1.0 GΩ after CM_{18}-Tat_{11} application.
Asterisks: -10 mV pulse delivery to measure R_m.

3.3.1 Isolated CM_{18} and Tat_{11} Peptides

Given the structural/functional modularity of CM_{18}-Tat_{11}, we used the two isolated CM_{18} and Tat_{11} peptides as controls for the observed behavior. CHO-K1 cells exposed to CM_{18} concentrations from 0.5 to 4 µM always showed detectable membrane currents, i.e. membrane destabilization. In particular, the application of 4 µM CM_{18} elicited a current with a *delay* = 0.9 ± 0.2 s up to an I_{max} = 1.0 ± 0.1 nA; with a τ_a, and τ_d equal to 2.1 ± 0.7 s and 3.7 ± 1.0 s, respectively (n = 7 cells). Application of 2 µM CM_{18} elicited a smaller current (I_{max} = 0.36 ± 0.07 nA) with a *delay* = 3.6 ± 1.1 s, τ_a = 4.0 ± 1.1 s, and τ_d = 3.2 ± 1.0 s (n = 6 cells). However, concentrations < 2 µM yielded activation and deactivation currents that could not be simply fitted with a single exponential and statistics are therefore not reported.

Contrary to what was found for CM_{18}-Tat_{11}, when the isolated CM_{18} was applied on CHO-K1 membrane, the permeabilization was fully reversible, upon peptide removal, for all tested concentration. This means that the current returned roughly exponentially to zero, and R_m fully recovered to its initial level (representative curve in Figure 3.6, *dark grey* trace). However, as shown in a typical recording in Figure 3.3, for repetitive CM_{18} applications at 4 µM, the recovery of current and of R_m was progressively more incomplete.

Figure 3.3 Whole-cell current recording elicited by five consecutive applications and withdrawals of 4 µM CM_{18} on CHO-K1 cells lasting, in sequence, 6.1, 5.2, 4.7, 6.2, and 4.1 s (*black bars*). The parameters characterizing each current were respectively: *delay*: 1.7, 1.0, 0.9, 0.9, 0.9 s; τ_a: 1.5, 1.2, 0.8, 0.7, 0.7 s; I_{max}: 1.8, 1.9, 2.0, 2.1, 2.0 nA; τ_d: 4.3, 4.4, 4.3, 6.0, 5.2 s. R_m and R_a were checked before and after each peptide application by means of a single −10 mV pulse (*asterisks*), and sometimes by repeated 10 mV pulses (*triangles*); *grey dotted line*: zero current; V_h = −20 mV.

Moreover, the current-to-voltage relationship was found to be linear (Figure 3.4), meaning that the peptide insertion in the membrane and the pore formation were not facilitated or hindered by the membrane voltages (unlike other pore-forming peptides, as alamethicin). This relationship

was obtained by applying voltage ramps (from -50 mV to +50 mV, slope = 0.25 mV/ms) during constant CM_{18} perfusion. To avoid the loss of voltage control due to R_a at extreme voltages (-50 mV and +50 mV, were the currents may become very large), CM_{18} was applied at 2 µM concentration, corresponding to a current not exceeding 2 nA at extreme voltages. The responses to three consecutive voltage ramps during CM_{18} perfusion were averaged and corrected by subtracting the average of the responses obtained from three voltage ramps recorded in control conditions.
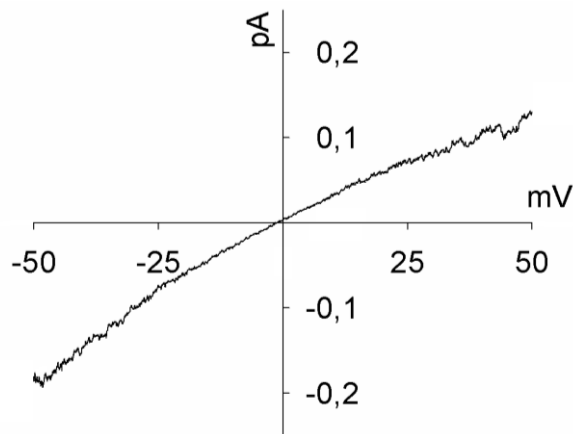
Figure 3.4 Voltage dependence of the current elicited by 2 µM CM_{18} applied on CHO-K1 cell, corrected for the leakage.

The resulting current-to-voltage relationship was almost perfectly ohmic at physiological voltages (Figure 3.4), and in all the cells examined (n = 4). Notably, all the recordings obtained with CM_{18} were very similar to the ones obtained with the analogous CM_{15} hybrid peptide (Milani et al., 2009). Previous investigation on CM_{15} activity performed by patch-clamp analysis and site-directed spin-labeling electron-paramagnetic-resonance studies (Pistolesi et al., 2007) indicated that it forms transient toroidal pores in the membrane. This suggests that CM_{15} and CM_{18} share the same membrane-destabilization mechanism.

Finally, continuous application of Tat_{11} (up to 5 min) at concentrations from 0.5 to 8 µM failed to elicit any current for all voltage values tested (from -80 mV to +80 mV), thus demonstrating that this module alone is not able to significantly permeabilize the membrane (Figure 3.6, *light grey trace*).

3.3.2 Comparison between CM_{18}-Tat_{11}, CM_{18}, and Tat_{11}

In order to provide a direct comparison between membrane-destabilization properties of CM_{18}-Tat_{11} and CM_{18}, we recorded data during sequential administration of these peptides to the same cell at 4 µM (*Figure 3.5A*). As expected, CM_{18} produced a reversible current, while CM_{18}-Tat_{11} leaded to irreversible membrane destabilization of the same cell. Increasing the peptide concentration to 8 µM still produced a reversible effect in the case of CM_{18} (although with an incomplete recovery, Figure 3.5*B*) while cell lysis and death were observed in the case of CM_{18}-Tat_{11} (Figure 3.5*B*, and 3.5*B inset*, experiment performed on the same cell).

In order to give an overall comparison of the three peptides, in Figure 3.6 are gathered whole-cell currents recording elicited by the application (in three different cells), of CM_{18}-Tat_{11} (6.7 s, 4 µM; *black bar* and *black trace*), CM_{18} (7.0 s, *grey bar* and *grey trace*), and Tat_{11} (71 s, 8 µM; *white bar* and *light grey trace*).
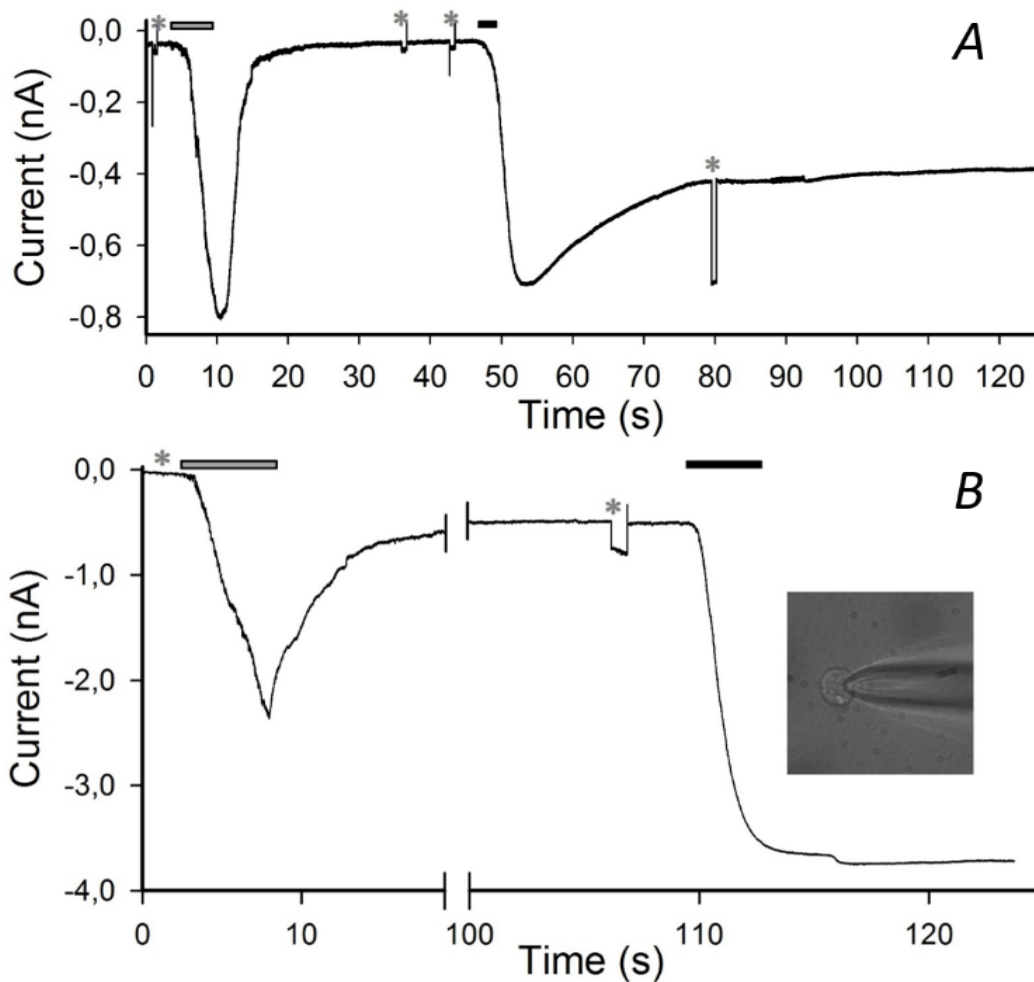
Figure 3.5 (*A*) Current elicited by application (7 s) and withdrawal of 4 µM CM_{18} (*grey bar*) and of 4 µM CM_{18}-Tat_{11} (3 s, *black bar*) on the same cell. (*B*) Current elicited by application and withdrawal of CM_{18} (9 s, 8 µM; *grey bar*) and of CM_{18}-Tat_{11} (7 s, 8 µM, *black bar*) on the same cell; *inset*, lysis and death of cell following >10 min application of CM_{18}-Tat_{11}. R_m was checked using -10 mV pulses (*asterisks*); Vh = -20 mV.
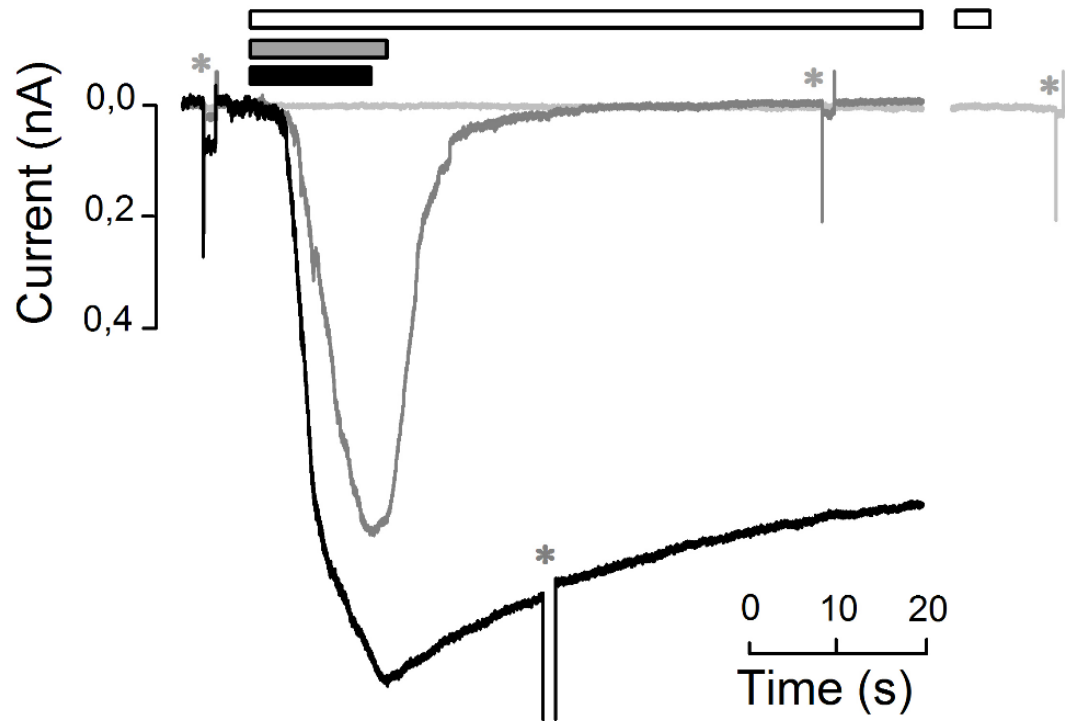
**Figure 3.6** Kinetics of peptide-induced membrane permeabilization of CHO-K1 cells. Currents elicited by application (on 3 different cells), of CM_{18}-Tat_{11} (6.7 s, 4 µM; *black bar* and *trace*), CM_{18} (7.0 s, *grey bar* and *trace*), and Tat_{11} (71 s, 8 µM; *white bar* and *light grey trace*; trace break: 33 s of uninterrupted Tat_{11} perfusion); V_h = −20 mV. *Asterisks*: -10 mV pulse.

3.4 Membrane-Disruptive Properties of CM_{12}

CM_{12} sequence was selected by Maccari after optimization and reduction of CM_{18} sequence, performed using a new introduced algorithm: the *Minimum and Maximum of auto- and cross-covariances* descriptor (for more information, see Maccari et al., 2013).

In order to study the mechanism of membrane permeabilization induced by the rational designed peptide CM_{12}, the same experimental conditions used for CM_{18}-Tat_{11} were maintained. Concentrations of CM_{12} < 1 µM gave no detectable macroscopic currents nor single channel events, while applications of CM_{12} ranging from 1 to 3 µM elicited currents with a *delay* = 9.1 ± 1.7 s up to an I_{max} = 0.6 ± 0.2 nA (n = 5; Figure 3.7A). Similarly to CM_{18}, the current did not return to the zero level following peptide removal; rather, the current recovered to a plateau level and the R_m measured on this plateau was consequently smaller in respect to the one measured before the CM_{12} application. When peptide concentration was raised up to 4 µM, CM_{12} elicited larger currents (I_{max} = 1.9 ± 0.6 nA) with a shorter *delay* (1.1 ± 0.2 s, n = 7). Moreover, after peptide removal in this case we did not see any recover of the current, suggesting an extensive membrane permeabilization as the one observed with CM_{18}-Tat_{11} (Figure 3.7B). To assess the potential voltage dependency of the current elicits by CM_{12}, we applied the same rapid voltage ramps used with CM_{18} (from -50 mV to +50 mV, slope: 0.25 mV/ms) during continuous peptide perfusion and in control conditions. As in the case of CM_{18} peptide, the resulting current-to-voltage relationship (after averaging and control subtraction) was almost perfectly ohmic for physiological voltages (Figure 3.8) in all cells examined (n = 4).
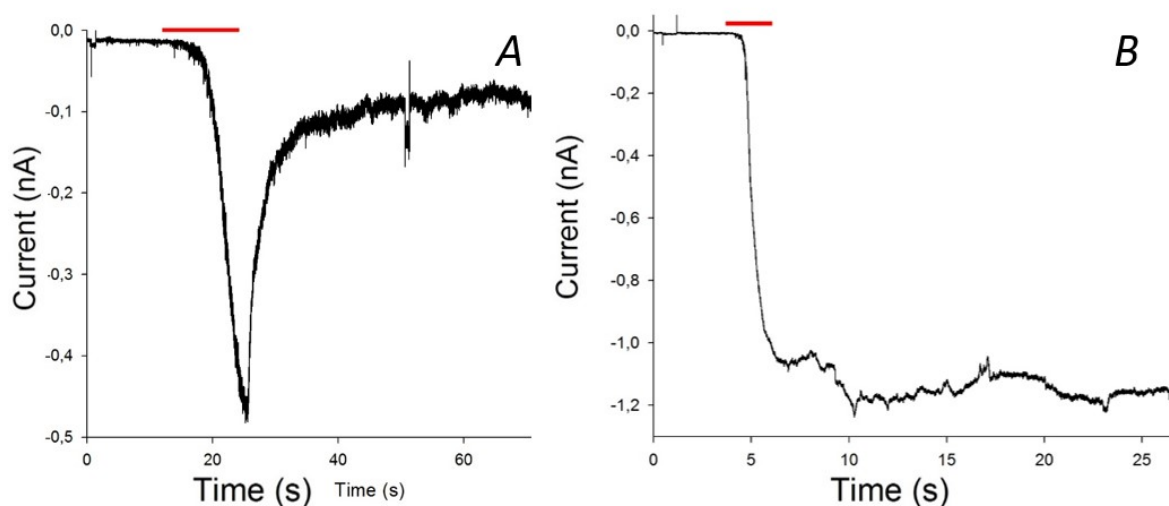
Figure 3.7 Currents elicited by application (on 2 different cells) of CM_{12} with a concentration of (*A*) 1 µM (6.7 s), and (*B*) 4 µM (7.0 s). *Red bars* indicate peptide application.
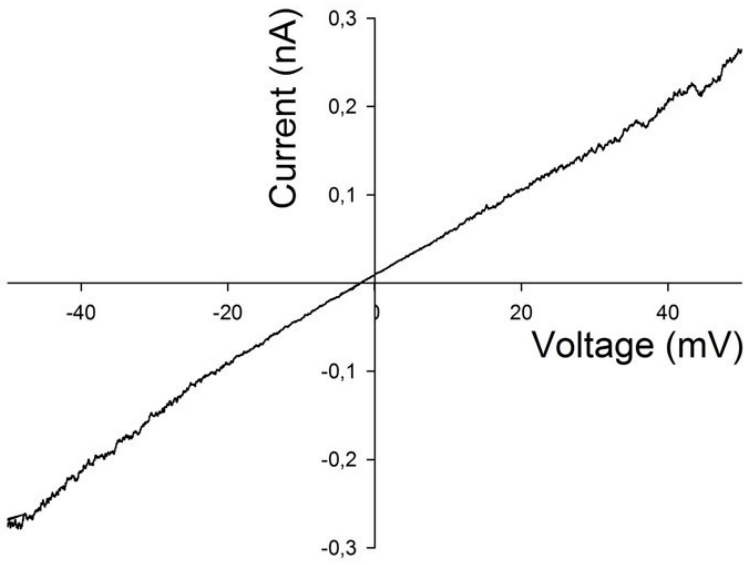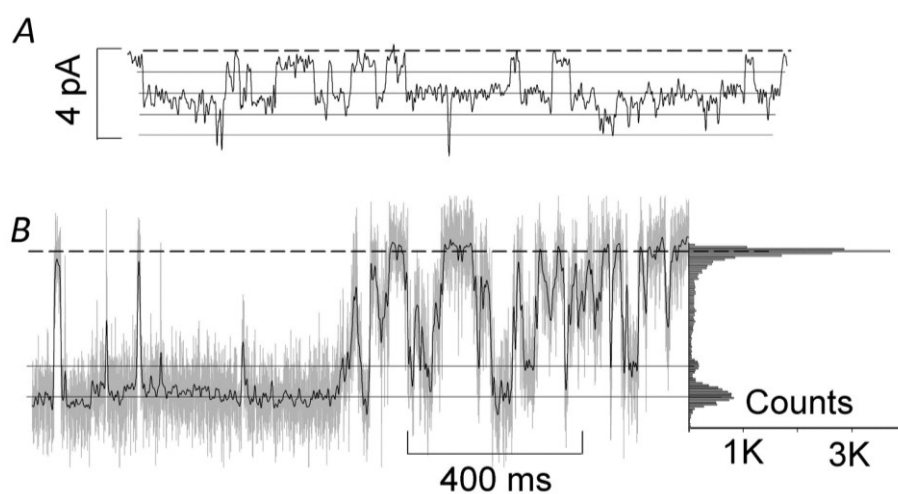
Figure 3.8
Voltage dependence of the current elicited by 1 µM CM_{12} applied on CHO-K1 cell, corrected for the leakage.

3.5 Single-Channel Properties of F50/5 and [L- Glu(OMe)[7,18,19]]

In order to study the single channel properties of F50/5 Alm and [L-Glu(OMe)[7,18,19]] Alm, and to assess their possible dependence on membrane composition, the peptides were inserted in the plasma membrane of an isolated frog rod outer segment (OS; recorded in whole-cell configuration), and in patches excised from GUVs. The peptides were applied to the membrane at concentrations low enough to give single-channels events, avoiding the development of macroscopic currents. Isolated OS was previously been proven to be an ideal preparation to study pore-forming peptides under strict physiological conditions (Vedovato and Rispoli, 2007). GUVs had a diameter > 10 μm, and were prepared by using the electroformation method (see *Materials and Methods*).

F50/5 Alm produced single-channel events of repetitive amplitude both in OS (Figure 3.9) and in GUVs (Figure 3.10). The larger events were usually an integer multiple of a fixed size. Since the events recorded in the OS were smaller than in GUVs, in the former case the traces were low-pass filtered at 100 Hz (Figure 3.9) which would otherwise cover most of these events. In the OS, single-channel events produced by F50/5 Alm at concentrations ranging between 0.25 and 0.5 μM manifested within 5 s from peptide application. The current amplitude of single-channels resulted of ~50 ± 8 pS at -20 mV (3500 events; n = 3 cells). In GUVs, under the same ionic and voltage conditions, it was necessary to raise the peptide concentration to 1-2.5 μM to obtain single-channel events, which again manifested within 5 s from peptide application. Since the single-channel events were about 5-fold larger than the OS, the recordings were filtered at 2 KHz, instead of 100 Hz.

Figure 3.9 Single-channel properties of Alm inserted in an OS.
A: single-channels recorded during application of F50/5 Alm
B, left: channel activity produced by [L-Glu(OMe)7,18,19] Alm, low-pass filtered at 2 KHz (*grey trace*) and at 100 Hz (superimposed *black trace*). *Right*: cumulative current amplitude distribution. V_h=-20 mV, same scales; continuous and dotted lines indicate the most probable single-channel amplitudes and 0 pA, respectively.

Although larger events were occasionally recorded not being an integer multiple of a fixed size, the cumulative distribution of current amplitudes in 3 GUVs (6500 events) gave at least 5 peaks equally separated by about 5 pA, corresponding to a single-channel amplitude of 250 ± 20 pS. [L-Glu(OMe)[7,18,19]] Alm produced larger events than F50/5 Alm in both OS and GUVs. Many different amplitudes were observed, but some were so fast that they were cut by the patch-clamp amplifier, even when filtering as high as 2 KHz (Figure 3.9B, *left*, *grey trace*). Since the majority of the events were anyway much slower, in order to compare the single-channel amplitude for [L-Glu(OMe)[7,18,19]] Alm in the two lipid environments, these very fast events were usually cancelled out upon low-pass filtering the traces at 100 Hz (Figure 3.9B, *left*, *black trace*; Figure 3.10B, *left*).
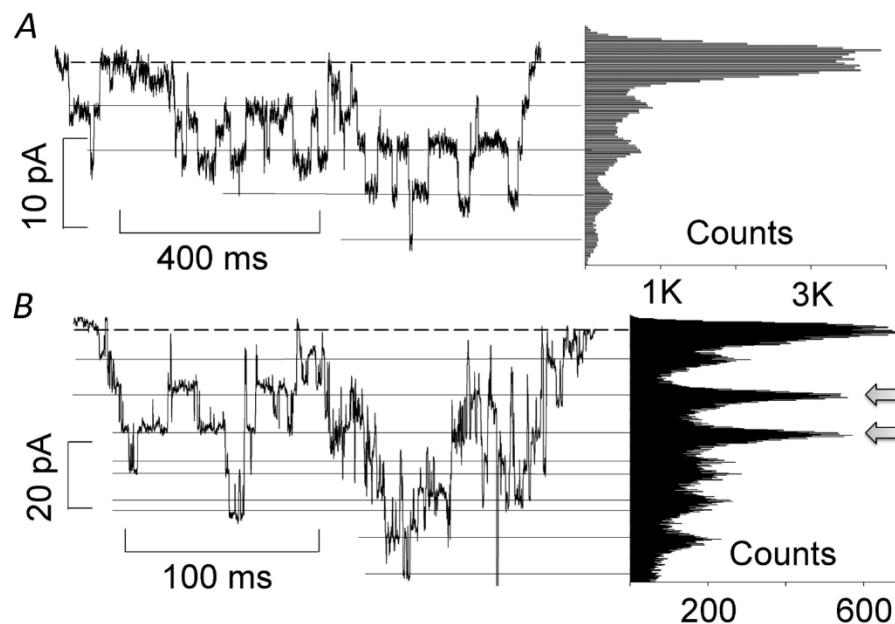

Figure 3.10 Single-channel properties of Alm inserted in GUVs.
A, left: single-channels recorded during application of F50/5 Alm (V_h = -20 mV). *Right*: cumulative distribution of the current amplitudes.
B, left: single-channels recorded during application of [L-Glu(OMe)7,18,19] Alm (V_h = -56 mV). *Right*: cumulative distribution of the current amplitudes. *Arrows* indicates the most frequent conductances, of ~250 and ~470 pS.

In the OS, current activated ~20 s after peptide application at V_h = -20 mV, due to the very low probability of pore formation by this peptide (Vedovato et al., 2007). The distribution of current amplitudes showed that the most probable amplitude was 310 ± 30 pS (820 events, n = 3; Figure 1B, right), but events of smaller sizes (as 260 pS) were recorded as well. In GUVs, the events at V_h = -20 mV were very scarce; therefore, V_h was raised to more negative voltages to obtain a sustained channel activity. Many different channel amplitudes were recorded: the two major peaks of their cumulative distribution gave the most frequent conductances of ~250 and ~470 pS (Figure 3.10B, arrows; 1400 events, n = 3).

3.6 Discussion

The data collected from the study of CM_{18}-Tat_{11} indicated that this peptide possess a stronger membrane activity compare with the single CM_{18} peptide. Indeed, an irreversible membrane destabilization is observed when concentrations ≥ 4 µM of CM_{18}-Tat_{11} are delivered on the CHO-K1 membrane, while same concentrations of CM_{18} gave reversible permeabilization. This could originates from the high positive charge density of Tat_{11} (rich in arginine residues), which leads to a stronger interaction of the peptide with the phospholipid head groups and to consequent membrane carpeting effect (Figure 3.11). However, it cannot be excluded that Tat_{11} may strongly promote membrane partitioning of CM_{18} up to a point that some of the resulting toroidal pores (characteristic of CM_{18} action) group together to delimit the contour of a micelle, that may eventually separate from the membrane and pass in solution.
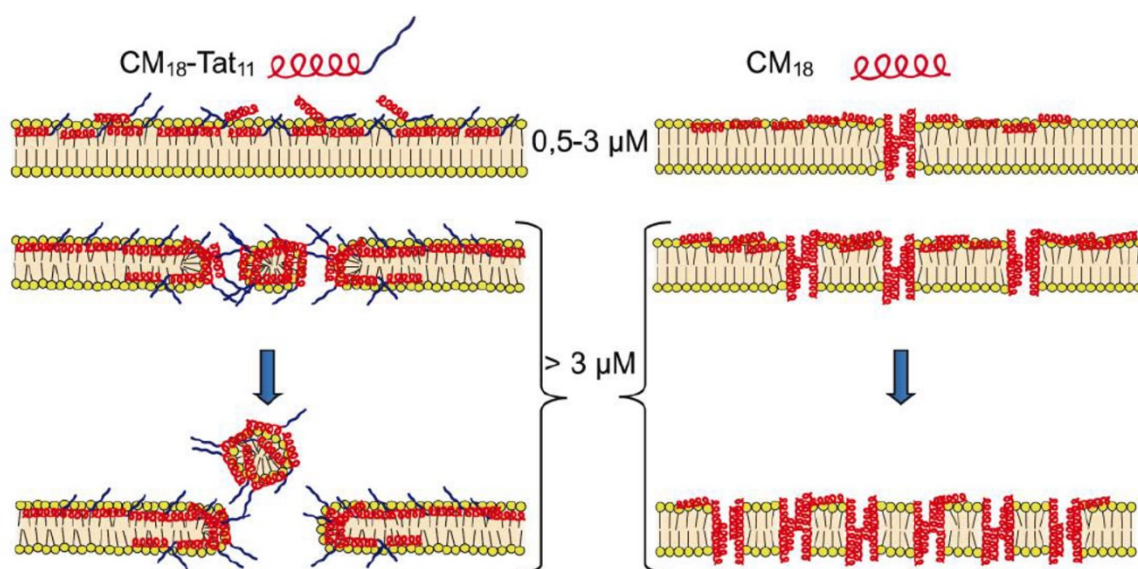
Figure 3.11 Schematic representation of the membrane destabilization mechanism proposed for CM_{18}-Tat_{11} (*left*) and CM_{18} (*right*) peptides. CM_{18} moiety is pictured as a red helix, while Tat_{11} moiety is represented as an unstructured blue segment. The upper part describes for each peptide its hypothetical membrane distribution when it is administered in the range between 0.5–3 µM. Instead the lower section represents the membrane distribution at concentrations higher than 4 µM.

This observations allow us to readily explain the reported results on this peptide as a delivery vector (Salomone et al., 2012, 2013). It can be argued that CM_{18}-Tat_{11} enters the cell with no membrane perturbing effects at low (i.e., nanomolar) concentrations by means of the endocytic pathway, as already demonstrated (Salomone et al., 2012). Then, during the physiological vesicular trafficking, the peptide eventually reaches its critical membrane-perturbing concentration (≥ 4 µM), dissolves the bilayer integrity by a carpet mechanism, and promotes the release of the co-administered macromolecules that specifically target the same route.

The strong effect observed with the rational designed peptide CM_{12} demonstrates that natural-derived peptides, as CM_{18}, can be optimized in order to maintain, or even improve, their antimicrobial activity, while at the same time reducing their length and thus lowering synthesis requirements. Despite a nearly 30% decrease in the chain length, application of CM_{12} on CHO-K1 membrane elicited reversible macroscopic currents that were comparable with the one observed with CM_{18}. This data confirmed previously studied where the peptides activity has been validated *in vitro* by testing the minimum bactericidal concentration against *S. aureus* and *P. aeruginosa* strains, representative of Gram-positive and Gram-negative bacteria, respectively (Maccari et al., 2013). Moreover, similarly with CM_{18}, the insertion of CM_{12} into the cellular membrane was found to be voltage-independent, suggesting that they act with the same mechanism of permeabilization, i.e. toroidal mode. However, for concentration of $CM_{12} \geq 4$, it was observed an irreversible destabilization of the membrane that could be due to a stronger activity of this peptide, which forms larger toroidal pores that at some point can fuse together and promote the detachment of membrane fragments.

Finally, the comparison between F50/5 Alm and [L- Glu(OMe)[7,18,19]] Alm inserted in both OS and GUVs, demonstrated that the latter peptide has a lower probability to form channels, but produces larger events than F50/5. These results are in line with the studies of the macroscopic currents elicited in frog OS and recorded using the whole-cell configuration (Vedovato et al., 2007). Despite both peptides generated larger events in GUVs than in OS, the overall similarity of the results obtained with these peptides in both lipid environments confirm that unilamellar vesicles represent a reliable model for preliminary studies of AMPs. However, the cellular model is still the best choice to precisely assess their *in-situ* properties.

Part II
Real-Time Modulation of zGCAP in Zebrafish Green Cones

3.7 Recording Stability and Response Waveform

The final objective of this section is to record with the patch-clamp technique the response waveform of an isolated zebrafish cone to controlled light stimuli, and provide new data to better understand the strong Ca^{2+} regulation on excitation and adaptation mediated by the Ca^{2+} sensor and GC activator zGCAP3. To this aim, experiments were performed to simulate the over-expression and down-regulation of this protein, by delivering it or its monoclonal antibody in a whole-cell recorded cone cell. Light responses of zebrafish cones were recorded using the whole-cell configuration of the patch-clamp technique under dark-adapted condition at room temperature (20-22°C); the holding potential was always -40 mV. Light stimuli were delivered using an ultra-bright LED (see *Materials and Methods*).

Before delivering the proteins in the zebrafish cone cytosol, it was essential to assess first that the photoresponse waveform remains stable for several minutes, at least for the time required to complete a perfusion experiment protocol.

We found that stable whole-cell recordings were obtained more often from isolated green cones; therefore, this study was limited to this cell type only. In Figure 3.12 is shown a typical recording using pressure-polished pipettes, lasting more than 20 min: since the time scale is very slow, the waveform of photoresponses are compressed and seen as thin vertical bars. Light flashes of increasing intensity (ranging from $1.14 \cdot 10^2$ to $3.76 \cdot 10^6$ photons/μm^2) were delivered in triplets and the entire sequence (with occasionally single light steps) was repeated over and over again.
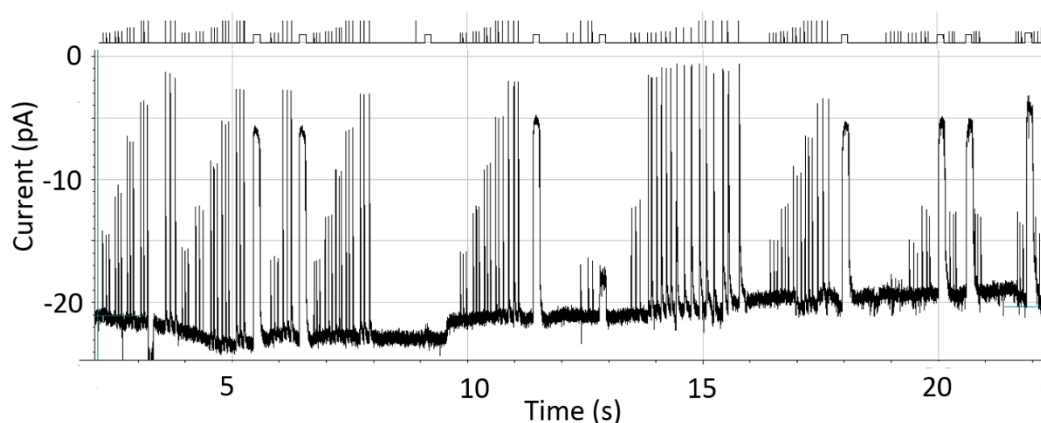
Figure 3.12 Typical whole-cell recording from a zebrafish cone. *Upper panel*: flash delivery time; *lower panel*, whole-cell recording of the current.

These recordings were terminated when the cone R_m, and/or its light sensitivity, decreased significantly. The small drift in the baseline was due to small changes in the current flowing through the inner segment channels rather than in changes in the light sensitive (or dark) current flowing through the cGMP channels. This is demonstrated by the fact that the amount of current suppressed by saturating flashes (with intensities $\geq 1.8 \cdot 10^4$ photons/μm^2) was the same from the beginning to the end of these recordings (average: 18.7 ± 1.8 pA; n=25).

To reject as much as possible the background noise, each photoresponse shown in the following figures is the average of three or more responses to the same flash; this average response is further smoothed (Figure 3.13*D*) by using the local smoothing routine implemented in SigmaPlot. This routine uses polynomial regression with weights computed from the Gaussian density function; the smoother function chosen as the negative exponential, with a sampling proportion of 0.01, a polynomial degree 1, and a number of interval that was 1/10 of the total number of samples constituting each trace (19220 samples for a 1 s trace). The smoothed and averaged responses to same flash intensities resulted very reproducible over a recording time of more than 20 min. Indeed, consecutive flashes of same intensities delivered within ~2, ~5, ~10, and ~15 min from the beginning of whole-cell recording revealed no significant differences with respect to dark current amplitude and response kinetics (Figure 3.13*A-C*).
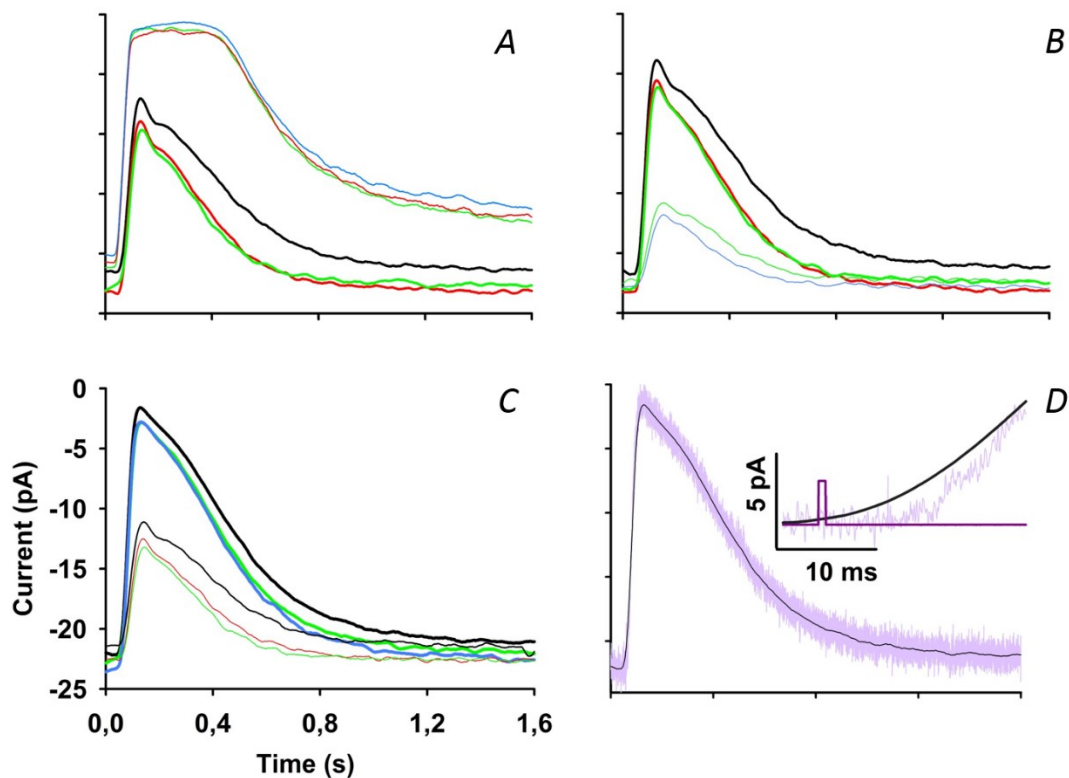
Figure 3.13 Stability of the flash responses. (*A*), (*B*), (*C*), averaged and smoothed response of 3 consecutive flashes of same intensity delivered within ~2, ~5, ~10, ~15 min from the beginning of recording (black, green, red, and blue traces) of six different intensities (in photons/ μm^2), grouped in two intensities in each panel: $4.49 \cdot 10^3$ and $3.76 \cdot 10^5$ (*A*), $1.14 \cdot 10^3$ and $8.68 \cdot 10^3$ (*B*), $2.32 \cdot 10^3$ and $1.77 \cdot 10^4$ (*C*). (*D*) unsmoothed average of three consecutive responses to a nearly saturating flash ($1.77 \cdot 10^4$ photons/μm^2, black trace) is compared to the smoothed one (purple trace), enlarged in the *inset*; the flash timing is indicated in dark purple.

In Figure 3.14*A-B-D* are reported the same photoresponses that have been averaged, aligned, and normalized. The superimposed flash responses in Figure 3*A* recovered from the maximum amplitude in a characteristic biphasic manner, that was particularly evident for flash intensities ranging from $2 \cdot 10^3$ to 10^4 photons/μm^2. This feature was observed clearly in ~40% of the recordings (n = 25), while other ones had a faster and monotonic recovery phase, as shown in Figure 3.14*B* (*red traces*, compared with the corresponding four biphasic responses of Figure 3.14*A*, on an expanded time scale), or a recovery in between these two kinds (Figure 3.14*B*, *thick blue trace*, corresponding to the blue trace of Figure 3.14*C*).
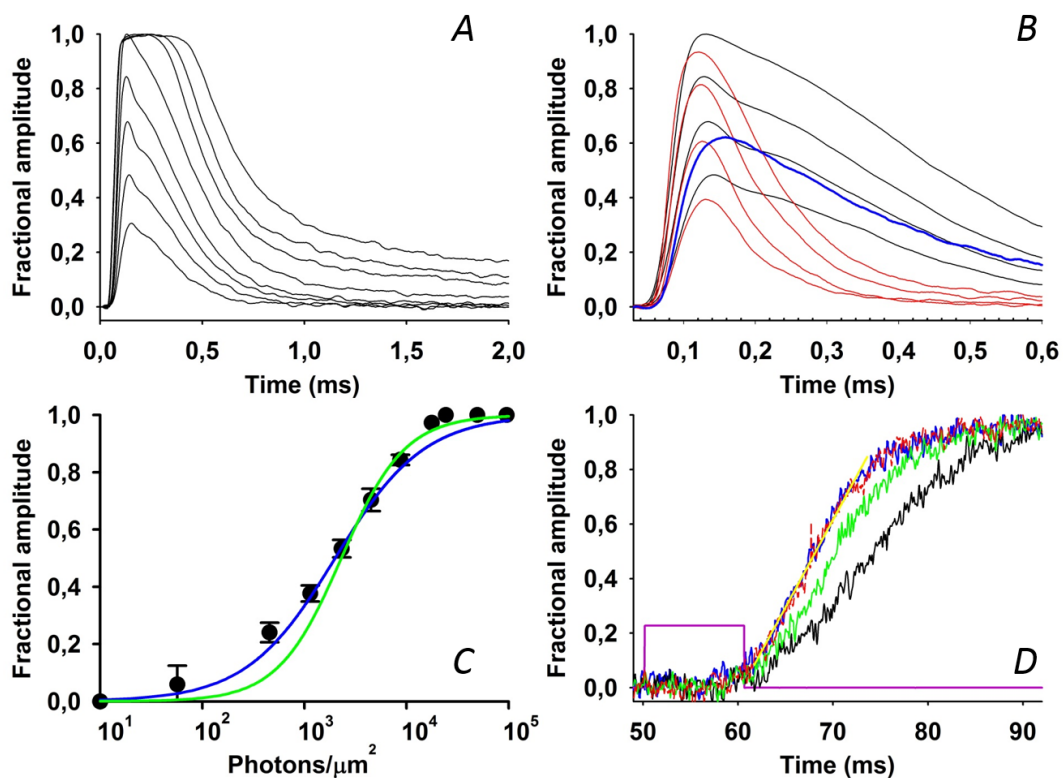
Figure 3.14 Waveform of the flash responses. (*A*) Flash responses of Figure 2 (*A*, *B,* and *C*) are averaged together and the corresponding six traces are aligned and normalized, other two photoresponses are added (flashes of $9.55 \cdot 10^4$ and $1.85 \cdot 10^5$ photons/μm^2). (*B*) Comparison of different response waveforms resulting from the same flash intensities. Traces had either a prominent biphasic response (*black traces*: $2.32 \cdot 10^3$, $4.49 \cdot 10^3$, $8.68 \cdot 10^3$, and $1.77 \cdot 10^4$ photons/μm^2) or showed monotonic recovery (*red traces*; each trace is the average of 9-16 responses). (*C*) Response amplitude vs light intensity (*n*=25 cells, each data point is the average of at least 75 responses to the same flash, *black dots* and *black line*) and Hill equation fit to the data points with *n*=1, I_0=2000 photons/μm^2 (*blue trace*) and n=1.4, I_0=2300 photons/μm^2 (*green trace*). (*D*) *Black*, *green*, *red*, and *blue* traces (flashes of $1.77 \cdot 10^4$, $9.55 \cdot 10^4$, $1.85 \cdot 10^5$, and $3.76 \cdot 10^5$ photons/μm^2, respectively), unsmoothed; *yellow trace*: linear fit to the rising phase of the two fastest responses (flashes of $1.85 \cdot 10^5$ and $3.76 \cdot 10^5$ photons/μm^2) having an angular coefficient of 64 s^{-1} (correlation coefficient: 0.97); *purple trace*: flash timing.

However, beside differences in the recovery phase, all green-sensitive cones had an almost identical response rising time and similar sensitivity, with a threshold of ~10^2 photons/µm^2 (the average response to this flash intensity had always a monotonic recovery; Figure 3.13A). Therefore, all response amplitudes were collectively analysed as a function of the light intensity in Figure 3.13*C*.

Data were fitted by the Hill equation:

$$R(I) = \frac{I^n}{I^n + I_0^n}$$

I_0 is the half-saturating intenstity, which was set to $2 \cdot 10^3$ photons/µm^2 in the fit giving the blue curve (n = 1). Changing both I_0 and *n* to higher values ($2.3 \cdot 10^3$ photons/µm^2 and n = 1.4) gave a better fit for higher light intensities, but the fit was worse at lower intensities (*green curve*).

3.8 Rising Phase Kinetics

In order to reduce the background noise, photoresponses were averaged and further processed with the smoothing routine described above. This operation did not alter the entire waveform of the photoresponse to dim up to just saturating flashes (i.e. delivering less than ~10^4 photons/µm^2), but it slightly altered the rising phase of stronger flashes at early times. Since this caused an underestimation of the delay between the flash delivery time and the response beginning (Figure 3.12*D*), the analysis of the responses to strong flashes were performed on unfiltered traces (Figure 3.12*D*; Figure 3.13*D*). It resulted that the rising phase kinetics accelerated by flashes up to an intensity of $1.85 \cdot 10^5$ photons/µm^2, but above this value no further acceleration was observed (Figure 3.13*D*). The linear fit to the normalized rising phase gave an angular coefficient of 48.6 ± 5.7 s^{-1} (n = 5 responses in 5 cells to flashes delivering $1.85 \cdot 10^5$ or $3.76 \cdot 10^5$ photons/µm^2).

3.9 Light Adaptation

Characteristic features of light adaptation in single green-sensitive cones were measured by applying an illumination protocol as indicated in Figure 3.15*A*, top row. Flashes of light were delivered to green-sensitive cones in the absence and presence of a light adapting background. A step of light elicited a fast current fall, followed by a much slower recovery to a steady-state level as the background light stimulus remained (Figure 3.15*A*). The average of step response amplitudes became slightly smaller at the second and third step response (Figure 3.15*A*), because the intermediate time of the cell in darkness was not sufficient to reach a full recovery to the dark state. Despite the large amount of light absorbed by the cone, the recordings were quite stable.

Indeed, the waveform of the average response to three consecutive flashes delivered in the dark and during the step of light were almost identical at the beginning (responses under the *black bars*, Figure 3.15*A*; *black traces*, Figure 3.15*B*), in the middle (*green*) and at the end (*red*) of the recording. By comparing the average response to flashes delivered in the presence of a background of light with the average response to flashes delivered in the dark, we found that the former was smaller and faster (Figure 3.15*C* and *D*). The background of $1.3 \cdot 10^5$ photons/($\mu m^2 \cdot s$) suppressed 63±9% of the dark current (10 steps averaged, n=3) and reduced the sensitivity as follows: a flash delivering $4.89 \cdot 10^3$ photons/μm^2 in the dark suppressed ~70±4% of the current (274 responses averaged, n=25), while a flash twice as strong delivered on the background suppressed ~45±12% (27 responses averaged, n=3) of the current (Figure 3.15*C*). Due to the extent of the desensitization, it was possible to compare only the response to saturating flashes delivered in the dark and on a background of light, as illustrated in Figure 3.15*D*.
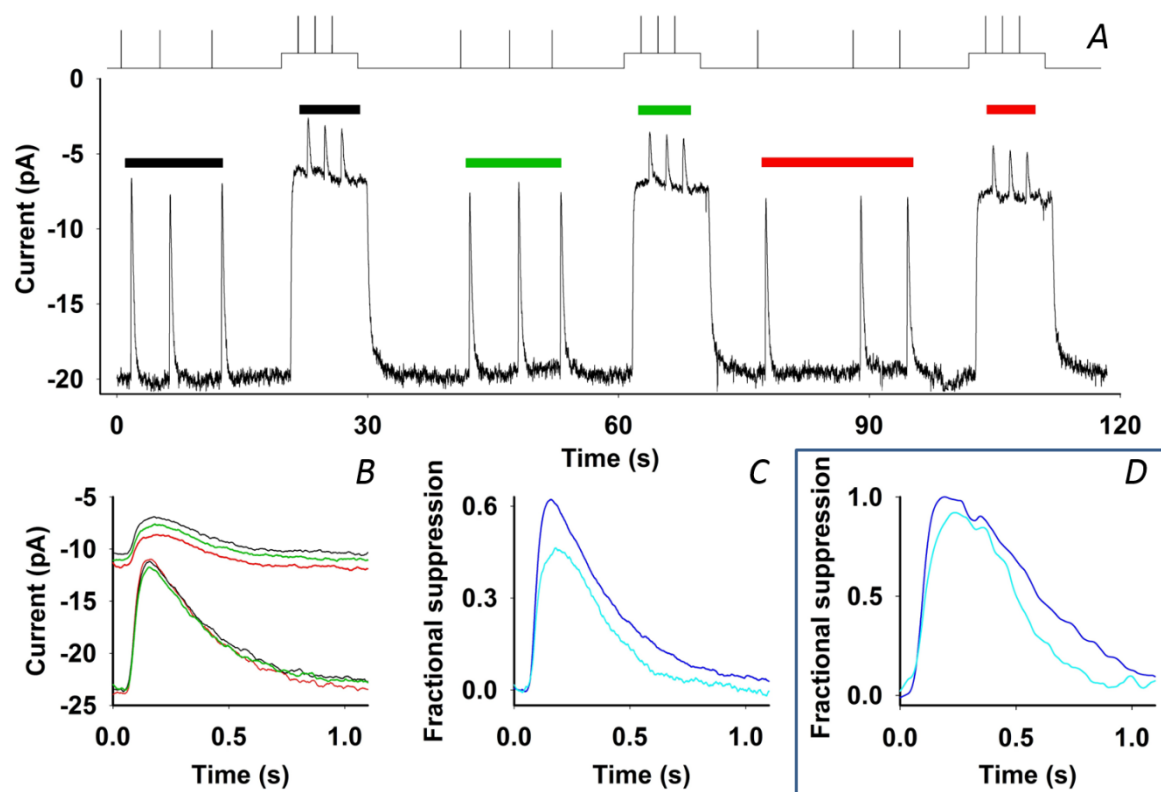
Figure 3.15 Stability of the light adaptation. *A*, *lower trace*, recording of the dark current; *upper trace*: timing of flashes and steps of light; the zero current corresponds to full suppression of the light-sensitive current. *B*, the average of 3 responses to the same flash ($4.49 \cdot 10^3$ photons/μm^2), delivered in the dark at the beginning (*black trace* and *black bar* in *A*, in the middle (*green*), and at the end (*red*) of the recording, is compared to the average of 3 responses to the same flash ($8.68 \cdot 10^3$ photons/μm^2) delivered on the 3 identical backgrounds of light ($1.3 \cdot 10^5$ photons/($\mu m^2 \cdot sec$). *C*, comparison between the average of the 9 flash responses in the dark of *B* (suppressing ~65% of the dark current, ~19.7 pA; *blue trace*), and the average of the 9 flash responses during the three light steps of *B* (suppressing ~45% of the residual dark current of each step, ~7.3 pA; *cyan trace*). *D*, comparison between the response to a $1.77 \cdot 10^4$ photons/μm^2 flash (*blue trace*) and the response to the same flash superimposed on the same background of *A* in another cell (*cyan trace*).

3.10 Modulation of zGCAP3 in Single Cone Cells

Based on the robustness and stability of the flash response and of some key features of light adaptation, it was concluded that the enlarged shank of the pressure-polished pipettes did not perturb the light-triggered enzyme cascade (i.e. it did not significantly wash out any molecule required for phototransduction). In order to provide insights on the role of zGCAP3 on the photoresponse, the effects of its cytosolic delivery or of its specific monoclonal antibody (to simulate the overexpression and down-regulation) were analysed according to the following protocol. Control photoresponses to flashes from very dim (to check the photoreceptor sensitivity) up to saturation (to measure the dark current amplitude) were collected over few minutes, to ensure that they were normal and reproducible. If not, it was usually possible to expel the cell with a strong pressure pulse applied to the pipette lumen, and gain the seal on another cell with the same pipette, by following the procedure described in Aquila et al., 2014. Once the cell healthiness was guaranteed, a positive pressure was applied to the pipette perfusion tube, long enough to expel a volume of solution containing the protein (~80 µl) that was at least three times of the volume of the control solution filling the patch pipette (i.e. ~25 µl). After at least 2 minutes (to allow the full cytosolic protein upload, see *Materials and Methods*), the light stimuli protocol used before the protein application was repeated.

3.10.1 Up-Regulation of zGCAP3

It was tested first purified recombinant zGCAP3, having high sensitivity to Ca^{2+} in the sub-micromolar range and strong activation of sensory GCs, being half-maximal at 30 nM free $[Ca^{2+}]$ (Fries et al., 2012). Concentrations of mammalian GCAP1 and GCAP2 have been estimated to be in the lower micromolar range (Hwang et al., 2003), therefore the zGCAP3 was perfused to a concentration of 40 µM, that was even above the value of 33 µM determined in carp cones (Takemoto et al., 2009). However, the cytosolic perfusion of 40 µM of zGCAP3 (dissolved in the intracellular solution, see *Materials and Methods*) did not alter significantly the photoresponse waveform of green sensitive cones (n = 7). In only two cells that had an unusual small dark current amplitude and slow flash response waveform, the application of zGCAP3 produced a slight falling phase acceleration and an amplitude reduction of
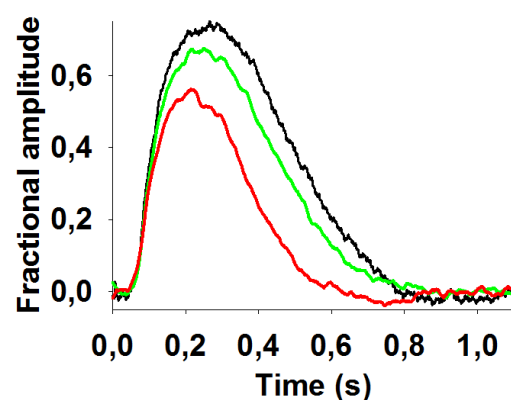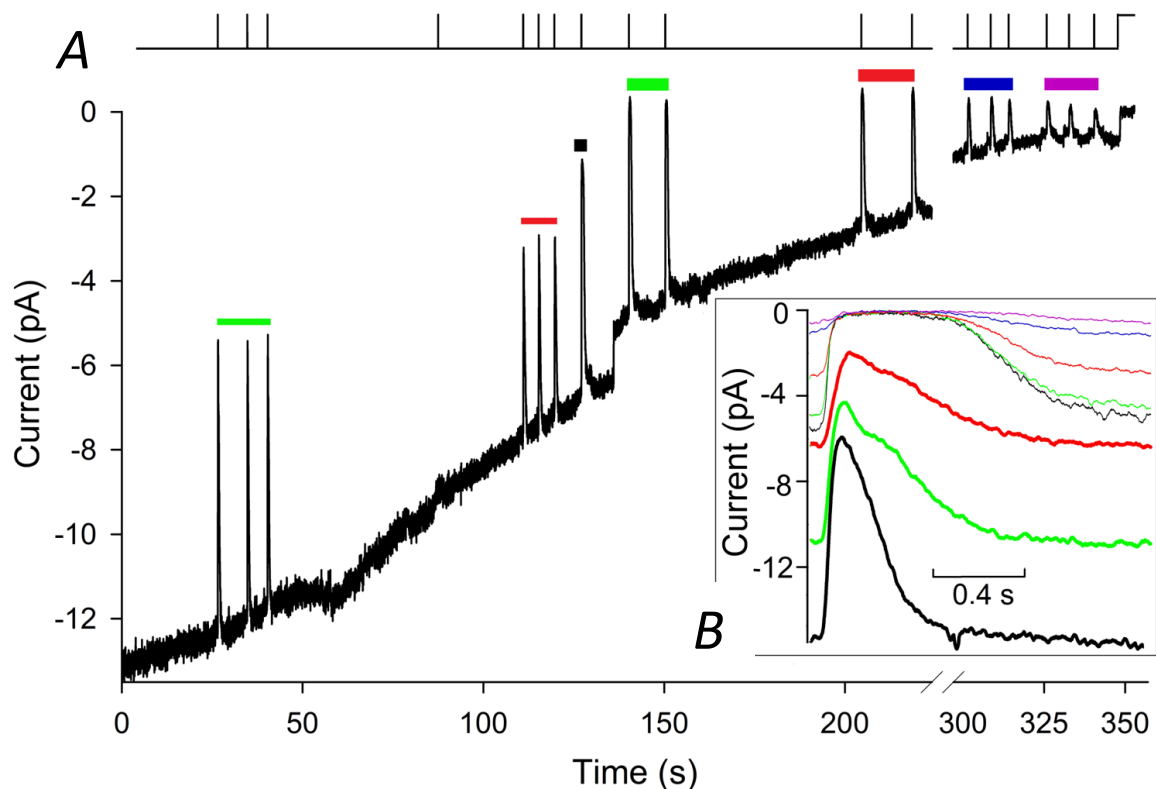
Figure 3.16 Effect of zGCAP3 intracellular delivery. Each one of the 3 traces are the average of 3 consecutive responses to the same flash ($4.49 \cdot 10^3$ photons/µm²) before (*black trace*), during (dashed trace) and after (*grey trace*) the application of 40 µM of purified zGCAP3 (average dark current ≈ 5.7

the flash response, that was substantially reversible (Figure 3.16); however, the dark current did not increase as the response accelerated.

3.10.2 Down-Regulation of zGCAP3

To perform the real-time down-regulation of zGCAP3, it was necessary first to identify a suitable antibody for the perfusion experiments: a monoclonal antibody named ZG3 7E6, purified by cation exchange chromatography, was chosen for its high specificity for zGCAP3 and lack of cross-reaction with other GCAP isoforms. When the ZG3 7E6 antibody (6.7 µM) was perfused into the cytosol of zebrafish cone cells, it caused a current fall, since there was a progressive fall of saturating flash response amplitude, with no changes in the zero level of dark current (n = 6, Figure 3.17A and B). Moreover, as expected by the progressively reduced Ca^{2+} sensitivity by GC, the flash response waveform progressively slowed down during the current fall (Figure 3.17B).

Figure 3.17 Effect of anti-zGCAP3 (ZG3 7E6) intracellular delivery.
A, recording of the dark current during the application of 6.7 µM of purified ZG3 7E6 dissolved in the intracellular solution; flashes of a $6.07 \cdot 10^3$ and $9.39 \cdot 10^4$ photons/µm^2 were delivered during the current fall; a step of light of $1.9 \cdot 10^7$ photons/(µm$^2 \cdot$sec) was delivered at the end of recording to check the residual dark current.
B, *thick traces*, average of 3 non-saturating responses to a $6.07 \cdot 10^3$ photons/µm^2 flash (to check the response waveform) delivered at the beginning of recording (*black*, not shown in *B*), at ~35 s (*green*), and at ~115 s (*red*). *Thin traces*, oversaturating responses to $9.39 \cdot 10^4$ photons/µm^2 (to check the zero light-sensitive current) at ~127 s (*black,* single response), ~145 s (*green*, 2 responses averaged), ~212 s (*red*, 2 responses averaged), ~310 s (*blue*, 3 responses averaged), and ~332 s (*magenta*, 3 responses averaged); all responses were aligned to the zero dark current.

3.11 Discussion

The data collected during whole-cell recordings from isolated zebrafish cones allow us to deeply investigate the mechanisms generating the light response. A peculiar feature of the recorded photoresponses was the fast kinetics of the rising phase at bright light intensities (Figure 3.13D), which reveals that within ~12 ms all the intracellular cGMP is hydrolysed. This could probably be due to the small volume of the cone outer segment (Pugh and Lamb, 2000) but it cannot be excluded that there are still less understood mechanisms that contribute to these fast kinetics. The frequency of interactions between rhodopsin (or cone opsin) and transducin, which diffuse freely on the disc membrane, has been considered a major factor in determining the slope of the rising phase and the cascade activation kinetics (Pugh and Lamb, 2000). Alternative studies suggested a different mechanism from the classical one based on collision coupling (Dell'Orco and Schmidt, 2008; Cangiano and Dell'Orco, 2013), suggesting that dimers of rhodopsin may interact with transducin in the dark by forming preassembled complexes (Dell'Orco and Koch, 2011). This mechanism could increase the probability of encounters between these proteins, resulting in the acceleration of photoresponse kinetics.

Another interesting feature of the response waveform is the change in the recovery phase (monotonic vs biphasic, Figure 3.13B) recorded in different cells. A monotonic recovery was observed in the responses to dim flashes or supersaturating flashes, while responses to flash from moderate (i.e. suppressing above 20% of dark current, Figure 3.13A, B) to just saturating intensities produced biphasic responses. This suggests that the biphasic recovery is elicited when the transient Ca^{2+} influx suppression is significant, but at the same time, the amount of light absorbed by the cone is low enough to allow a rapid inactivation of the PDE, so that the cascade is quickly stopped. This indicates that the difference between the two recovery phases originate by a different intracellular Ca^{2+} dynamics, which in fact regulates a plethora of Ca^{2+} sensor proteins regulating the phototransduction cascade at various levels (Nakatani et al., 2002; Kawamura and Tachibanaki, 2008; Scholten and Koch, 2011), collectively acting as a negative feedback.

Perfusion of zGCAP3 did not alter significantly the photoresponse; although its perfusion solution concentration was 40 μM, i.e. comparable or even higher in respect to its endogenous concentration (see *Materials and Methods*). Thus, lack of any zGCAP3 effect during perfusion suggests that the GC in double cone cells was already saturated under our measuring conditions, which is consistent with previous *in vitro* data on the half-maximal activation of GCs by zGCAP3 being at 0.7 μM (Scholten and Koch, 2011). Further, no displacement of another zGCAP seemed to occur, which could have caused a disturbance of the normal photoresponse. Collectively, the above results indicated that zGCAP3 is probably the only relevant regulator of the endogenous GC in green cone cells. The rapid fall of the dark current and the progressive slowdown of the response

waveform observed during intracellular perfusion of zGCAP3 antibody (Figure 3.16) reveal a rapid shutdown of the cGMP production, consistent with an inhibition of GC. Nevertheless, the complete shutdown of the dark current was surprising, suggesting that the antibody can cause non-specific disturbances inside the small volume of the cone OS, in particular during longer perfusion.

Conclusions

In the first project of this thesis, I investigated the mechanism of membrane perturbation of cell-penetrating and antimicrobial peptides using the patch-clamp technique. I found that CM_{18}-Tat_{11} produces a large and irreversible plasma membrane lysis, at concentration where CM_{18} and Tat_{11} gave instead a nearly reversible membrane permeabilization and no perturbation, respectively. Furthermore, using the same method, I studied the biophysical characteristic of another antimicrobial peptide, called CM_{12}, which sequence was obtained from the optimization of CM_{18} (Maccari et al., 2013). When applied on CHO, CM_{12} and CM_{18} produced voltage-independent membrane permeabilization, and no single-channel events were detected at low peptides concentration. These results indicate that both peptides form pores according to a toroidal model, in which the lipid layer bends continuously through the pore so that the core is formed by both lipid head groups and the peptides. Finally, I have studied the single channels properties generated by the pore-forming peptide alamethicin (Alm) F50/5 and its [L-Glu(OMe)^{7,18,19}] analog. It was confirmed that the hydrophilic Gln residues at positions 7, 18, and 19 of alamethicin F50/5 are not a key factor for pore formation, but the [L-Glu(OMe)^{7,18,19}] analogue produced larger pores, with a lower probability of formation than alamethicin F50/5. Moreover, the lipid-dependence of peptides activity was studied, comparing the single-channel recordings of the peptides applied on a natural membrane (frog OS) and in giant unilamellar vesicles (GUVs). Although the overall channel characteristics resulted comparable, both peptides generated larger events when inserted in GUVs. This indicates that tests on artificial membranes represent a valid starting point for the study of membrane-active peptide properties; nevertheless, they could not completely substitute the complexity of a living cell membrane.

In the second part, I focused my attention on the role of the Ca^{2+} sensor and regulator of the guanylate cyclase zGCAP3 in mechanically isolated zebrafish green-sensitive cones. Firstly, I performed whole-cell patch-clamp recordings from cone cells with pressure-polished pipettes and found that they were stable for several minutes, having reproducible sensitivity, waveform photoresponse kinetics and light adaptation. In particular, we found a cell-to-cell variability in the flash response recovery phase, suggesting that they are governed by different intracellular Ca^{2+} dynamics. Moreover, we observed that responses to supersaturating flashes presented a very fast rising phase, suggesting that opsin and transducin form preassembled complexes in the dark. These studies were followed by experiments in which the zGCAP3 or its monoclonal antibody were efficiently perfused inside the cone OS by positioning perfusion tubes very close to the pipette tip. The up-regulation of zGCAP3 did not altered significantly the light response, while the perfusion

with the antibody anti-zGCAP3 caused the progressive fall of the background current, together with the progressive slowing down of the flash response kinetics. The surprising lack of an effect of zGCAP3 incorporation, suggested that the endogenous number of zGCAP3 is saturating, therefore any further increase of this sensor is ineffective. However, the effects of the antibody can be explained as an inhibition of the target enzyme of zGCAP3, which is the guanylate cyclase (GC).

References

Adler, A.J., and Martin, K.J. 1982. Retinol-binding proteins in bovine interphotoreceptor matrix. Biochem Biophys Res Commun. 108:1601–8.

Aili, D., and Stevens, M.M. 2010. Bioresponsive peptide-inorganic hybrid nanomaterials. Chem Soc Rev. 39:3358–70.

Anderson, D.H., and Fisher, S.K. 1976. The photoreceptors of diurnal squirrels: outer segment structure, disc shedding, and protein renewal. J Ultrastruct Res. 55:119–41.

Anderson, D.H., Fisher, S.K., and Steinberg, R.H. 1978. Mammalian cones: disc shedding, phagocytosis, and renewal. Invest Ophthalmol Vis Sci. 17:117–33.

Andreu, D., Merrifield, R.B., Steiner, H., and Boman, H.G. 1985. N-terminal analogues of cecropin A: synthesis, antibacterial activity, and conformational properties. Biochemistry. 24:1683–8.

Andreu, D., Ubach, J., Boman, A., Wåhlin, B., Wade, D., Merrifield, R.B., and Boman, H.G. 1992. Shortened cecropin A-melittin hybrids Significant size reduction retains potent antibiotic activity. FEBS Lett. 296:190–194.

Angelova, M.I., and Dimitrov, D.S. 1986. Liposome electroformation. Faraday Discuss Chem Soc. 81:303.

Aoki, W., and Ueda, M. 2013. Characterization of Antimicrobial Peptides toward the Development of Novel Antibiotics. Pharmaceuticals (Basel). 6:1055–81.

Aquila, M., Benedusi, M., Fasoli, A., and Rispoli, G. 2014. Pressure-polished borosilicate pipettes are "universal sealer" yielding low access resistance and efficient intracellular perfusion. Methods Mol Biol. 1183:279–89.

Aquila, M., Benedusi, M., Koch, K.-W., Dell'Orco, D., and Rispoli, G. 2013. Divalent cations modulate membrane binding and pore formation of a potent antibiotic peptide analog of alamethicin. Cell Calcium. 53:180–6.

Astriab-Fisher, A., Sergueev, D., Fisher, M., Shaw, B.R., and Juliano, R.L. 2002. Conjugates of antisense oligonucleotides with the Tat and antennapedia cell-penetrating peptides: effects on cellular uptake, binding to target sequences, and biologic actions. Pharm Res. 19:744–54.

Ayoub, G.S., and Copenhagen, D.R. 1991. Application of a fluorometric method to measure glutamate release from single retinal photoreceptors. J Neurosci Methods. 37:7–14.

Bader, C.R., Bertrand, D., and Schwartz, E.A. 1982. Voltage-activated and calcium-activated currents studied in solitary rod inner segments from the salamander retina. J Physiol. 331:253–84.

Barinaga, M. 1990. Zebrafish: swimming into the development mainstream. Science. 250:34–5.

Barnes, S., and Hille, B. 1989. Ionic channels of the inner segment of tiger salamander cone photoreceptors. J Gen Physiol. 94:719–43.

Baumann, G., and Mueller, P. 1974. A molecular model of membrane excitability. J Supramol Struct. 2:538–57.

Baylor, D.A. 1987. Photoreceptor signals and vision. Proctor lecture. Invest Ophthalmol Vis Sci. 28:34–49.

Baylor, D.A., Lamb, T.D., and Yau, K.W. 1979. Responses of retinal rods to single photons. J Physiol. 288:613–34.

Bechara, C., and Sagan, S. 2013. Cell-penetrating peptides: 20 years later, where do we stand?. FEBS Lett. 587:1693–1702.

Bechinger, B. 1999. The structure, dynamics and orientation of antimicrobial peptides in membranes by multidimensional solid-state NMR spectroscopy. Biochim Biophys Acta. 1462:157–83.

Behnen, P., Scholten, A., Rätscho, N., and Koch, K.-W. 2009. The cone-specific calcium sensor guanylate cyclase activating protein 4 from the zebrafish retina. J Biol Inorg Chem. 14:89–99.

Berlose, J.P., Convert, O., Derossi, D., Brunissen, A., and Chassaing, G. 1996. Conformational and associative behaviours of the third helix of antennapedia homeodomain in membrane-mimetic environments. Eur J Biochem. 242:372–86.

Besharse, J.C., and Pfenninger, K.H. 1980. Membrane assembly in retinal photoreceptors I. Freeze-fracture analysis of cytoplasmic vesicles in relationship to disc assembly. J Cell Biol. 87:451–63.

Béven, L., Duval, D., Rebuffat, S., Riddell, F.G., Bodo, B., and Wróblewski, H. 1998. Membrane permeabilisation and antimycoplasmic activity of the 18-residue peptaibols, trichorzins PA. Biochim Biophys Acta. 1372:78–90.

Bi, X., Wang, C., Dong, W., Zhu, W., and Shang, D. 2014. Antimicrobial properties and interaction of two Trp-substituted cationic antimicrobial peptides with a lipid bilayer. J Antibiot (Tokyo). 67:361–8.

Bilotta, J., and Saszik, S. 2001. The zebrafish as a model visual system. Int J Dev Neurosci. 19:621–629.

Bok, D., and Young, R.W. 1972. The renewal of diffusely distributed protein in the outer segments of rods and cones. Vision Res. 12:161–8.

Boman, H.G., Wade, D., Boman, I.A., Wåhlin, B., and Merrifield, R.B. 1989. Antibacterial and antimalarial properties of peptides that are cecropin-melittin hybrids. FEBS Lett. 259:103–106.

Bowmaker, J.K. 1980. Birds see ultraviolet light. Nature. 284:306.

Bowmaker, J.K., and Dartnall, H.J. 1980. Visual pigments of rods and cones in a human retina. J Physiol. 298:501–11.

Bowmaker, J.K., Dartnall, H.J., Lythgoe, J.N., and Mollon, J.D. 1978. The visual pigments of rods and cones in the rhesus monkey, Macaca mulatta. J Physiol. 274:329–48.

Bowmaker, J.K., Dartnall, H.J., and Mollon, J.D. 1980. Microspectrophotometric demonstration of four classes of photoreceptor in an old world primate, Macaca fascicularis. J Physiol. 298:131–43.

Branchek, T., and Bremiller, R. 1984. The development of photoreceptors in the zebrafish, Brachydanio rerio. I. Structure. J Comp Neurol. 224:107–15.

Brogden, K.A. 2005. Antimicrobial peptides: pore formers or metabolic inhibitors in bacteria?. Nat Rev Microbiol. 3:238–50.

Brooks, H., Lebleu, B., and Vivès, E. 2005. Tat peptide-mediated cellular delivery: back to basics. Adv Drug Deliv Rev. 57:559–77.

Brown, P.K., and Wald, G. 1964. VISUAL PIGMENTS IN SINGLE RODS AND CONES OF THE HUMAN RETINA. DIRECT MEASUREMENTS REVEAL MECHANISMS OF HUMAN NIGHT AND COLOR VISION. Science (80-). 144:45–52.

Burgoyne, R.D. 2007. Neuronal calcium sensor proteins: generating diversity in neuronal Ca2+ signalling. Nat Rev Neurosci. 8:182–93.

Cajal, S.R. y. 1893. La rétine des vertébrés. Cellule. 9:119–257.

Cangiano, L., and Dell'Orco, D. 2013. Detecting single photons: a supramolecular matter?. FEBS Lett. 587:1–4.

Chader, G.J. 1989. Interphotoreceptor retinoid-binding protein (IRBP): a model protein for molecular biological and clinically relevant studies. Friedenwald lecture. Invest Ophthalmol Vis Sci. 30:7–22.

Choi, H., Yang, Z., and Weisshaar, J.C. 2015. Single-cell, real-time detection of oxidative stress induced in Escherichia coli by the antimicrobial peptide CM15. Proc Natl Acad Sci. 201417703.

Choi, Y., McCarthy, J.R., Weissleder, R., and Tung, C.-H. 2006. Conjugation of a photosensitizer to an oligoarginine-based cell-penetrating peptide increases the efficacy of photodynamic therapy. ChemMedChem. 1:458–63.

Cirillo, G., Hampel, S., Spizzirri, U.G., Parisi, O.I., Picci, N., and Iemma, F. 2014. Carbon nanotubes hybrid hydrogels in drug delivery: a perspective review. Biomed Res Int. 2014:825017.

Cohen, A.I. 1960. The ultrastructure of the rods of the mouse retina. Am J Anat. 107:23–48.

Cohen, A.I. 1964. SOME OBSERVATIONS ON THE FINE STRUCTURE OF THE RETINAL RECEPTORS OF THE AMERICAN GRAY SQUIRREL. Invest Ophthalmol. 3:198–216.

Conner, S., and Schmid, S. 2003. Regulated portals of entry into the cell. Nature. 422:37–44.

Copenhagen, D.R., and Jahr, C.E. 1989. Release of endogenous excitatory amino acids from turtle photoreceptors. Nature. 341:536–9.

Dell'Orco, D., and Koch, K.-W. 2011. A dynamic scaffolding mechanism for rhodopsin and transducin interaction in vertebrate vision. Biochem J. 440:263–71.

Dell'Orco, D., and Schmidt, H. 2008. Mesoscopic Monte Carlo simulations of stochastic encounters between photoactivated rhodopsin and transducin in disc membranes. J Phys Chem B. 112:4419–26.

Derossi, D., Calvet, S., Trembleau, A., Brunissen, A., Chassaing, G., and Prochiantz, A. 1996. Cell internalization of the third helix of the Antennapedia homeodomain is receptor-independent. J Biol Chem. 271:18188–93.

Derossi, D., Joliot, A.H., Chassaing, G., and Prochiantz, A. 1994. The third helix of the Antennapedia homeodomain translocates through biological membranes. J Biol Chem. 269:10444–50.

Deshayes, S., Morris, M.C., Divita, G., and Heitz, F. 2005. Cell-penetrating peptides: tools for intracellular delivery of therapeutics. Cell Mol Life Sci. 62:1839–49.

Dhople, V., Krukemeyer, A., and Ramamoorthy, A. 2006. The human beta-defensin-3, an antibacterial peptide with multiple biological functions. Biochim Biophys Acta. 1758:1499–512.

Dowling, J.E. 1970. Organization of the vertebrate retina. Nihon Seirigaku Zasshi. 32:546–547.

Dowling, J.E., and Boycott, B.B. 1966. Organization of the primate retina: electron microscopy. Proc R Soc Lond B Biol Sci. 166:80–111.

Driever, W., Stemple, D., Schier, A., and Solnica-Krezel, L. 1994. Zebrafish: genetic tools for studying vertebrate development. Trends Genet. 10:152–9.

Duchardt, F., Fotin-Mleczek, M., Schwarz, H., Fischer, R., and Brock, R. 2007. A comprehensive model for the cellular uptake of cationic cell-penetrating peptides. Traffic. 8:848–66.

Eiríksdóttir, E., Mäger, I., Lehto, T., Andaloussi, S. El, and Langel, Ü. 2010. Cellular internalization kinetics of (luciferin-)cell-penetrating peptide conjugates. Bioconjug Chem. 21:1662–72.

El-Sayed, A., Futaki, S., and Harashima, H. 2009. Delivery of macromolecules using arginine-rich cell-penetrating peptides: ways to overcome endosomal entrapment. AAPS J. 11:13–22.

Erazo-Oliveras, A., Muthukrishnan, N., Baker, R., Wang, T.-Y., and Pellois, J.-P. 2012. Improving the endosomal escape of cell-penetrating peptides and their cargos: strategies and challenges. Pharmaceuticals (Basel). 5:1177–209.

Ermilov, A.N., Olshevskaya, E. V, and Dizhoor, A.M. 2001. Instead of binding calcium, one of the EF-hand structures in guanylyl cyclase activating protein-2 is required for targeting photoreceptor guanylyl cyclase. J Biol Chem. 276:48143–8.

Estes, D.J., and Mayer, M. 2005. Electroformation of giant liposomes from spin-coated films of lipids. Colloids Surf B Biointerfaces. 42:115–23.

Fain, G.L., Matthews, H.R., Cornwall, M.C., and Koutalos, Y. 2001. Adaptation in vertebrate photoreceptors. Physiol Rev. 81:117–151.

Fernández-Carneado, J., Kogan, M.J., Pujals, S., and Giralt, E. 2004. Amphipathic peptides and drug delivery. Biopolymers. 76:196–203.

Fesenko, E.E., Kolesnikov, S.S., and Lyubarsky, A.L. 1985. Induction by cyclic GMP of cationic conductance in plasma membrane of retinal rod outer segment. Nature. 313:310–313.

Fittipaldi, A., Ferrari, A., Zoppé, M., Arcangeli, C., Pellegrini, V., Beltram, F., and Giacca, M. 2003. Cell membrane lipid rafts mediate caveolar endocytosis of HIV-1 Tat fusion proteins. J Biol Chem. 278:34141–9.

Fjell, C.D., Hiss, J.A., Hancock, R.E.W., and Schneider, G. 2012. Designing antimicrobial peptides: form follows function. Nat Rev Drug Discov. 11:37–51.

Fox, R.O., and Richards, F.M. 1982. A voltage-gated ion channel model inferred from the crystal structure of alamethicin at 1.5-A resolution. Nature. 300:325–30.

Frankel, A.D., and Pabo, C.O. 1988. Cellular uptake of the tat protein from human immunodeficiency virus. Cell. 55:1189–93.

Fries, R., Scholten, A., Säftel, W., and Koch, K.-W. 2012. Operation profile of zebrafish guanylate cyclase-activating protein 3. J Neurochem. 121:54–65.

Fries, R., Scholten, A., Säftel, W., and Koch, K.-W. 2013. Zebrafish guanylate cyclase type 3 signaling in cone photoreceptors. PLoS One. 8:e69656.

Frins, S., Bönigk, W., Müller, F., Kellner, R., and Koch, K.W. 1996. Functional characterization of a guanylyl cyclase-activating protein from vertebrate rods. Cloning, heterologous expression, and localization. J Biol Chem. 271:8022–7.

Futaki, S., Suzuki, T., Ohashi, W., Yagami, T., Tanaka, S., Ueda, K., and Sugiura, Y. 2001. Arginine-rich peptides. An abundant source of membrane-permeable peptides having potential as carriers for intracellular protein delivery. J Biol Chem. 276:5836–40.

Gorczyca, W.A., Gray-Keller, M.P., Detwiler, P.B., and Palczewski, K. 1994. Purification and physiological evaluation of a guanylate cyclase activating protein from retinal rods. Proc Natl Acad Sci U S A. 91:4014–8.

Green, M., and Loewenstein, P. 1988. Autonomous functional domains of chemically synthesized human immunodeficiency virus Tat Trans-Activator Protein. Cell. 55:1179–88.

Gros, E., Deshayes, S., Morris, M.C., Aldrian-Herrada, G., Depollier, J., Heitz, F., and Divita, G. 2006. A non-covalent peptide-based strategy for protein and peptide nucleic acid transduction. Biochim Biophys Acta. 1758:384–93.

Hagins, W.A., Penn, R.D., and Yoshikami, S. 1970. Dark current and photocurrent in retinal rods. Biophys J. 10:380–412.

Hamill, O.P., Marty, A., Neher, E., Sakmann, B., and Sigworth, F.J. 1981. Improved patch-clamp techniques for high-resolution current recording from cells and cell-free membrane patches. Pflugers Arch. 391:85–100.

Hassane, F.S., Ivanova, G.D., Bolewska-Pedyczak, E., Abes, R., Arzumanov, A.A., Gait, M.J., Lebleu, B., and Gariépy, J. 2009. A peptide-based dendrimer that enhances the splice-redirecting activity of PNA conjugates in cells. Bioconjug Chem. 20:1523–30.

Heffernan, C., Sumer, H., Guillemin, G.J., Manuelpillai, U., and Verma, P.J. 2012. Design and screening of a glial cell-specific, cell penetrating peptide for therapeutic applications in multiple sclerosis. PLoS One. 7:e45501.

Herce, H.D., and Garcia, A.E. 2007. Cell penetrating peptides: how do they do it?. J Biol Phys. 33:345–56.

Herce, H.D., Garcia, A.E., Litt, J., and Kane, R.S. 2009. Arginine-rich peptides destabilize the plasma membrane, consistent with a pore formation translocation mechanism of cell-penetrating peptides. Biophys J. 97:1917–25.

Hille, B. 2001. Ion Channels of Excitable Membranes.

Hisatomi, O., and Tokunaga, F. 2002. Molecular evolution of proteins involved in vertebrate phototransduction. Comp Biochem Physiol Part B Biochem Mol Biol. 133:509–522.

Holm, T., and Langel, Ü. 2005. Cell-penetrating peptides: mechanisms and applications. Curr Pharm Des. 11:3597–611.

Hoskin, D.W., and Ramamoorthy, A. 2008. Studies on anticancer activities of antimicrobial peptides. Biochim Biophys Acta. 1778:357–75.

Huttner, A., Harbarth, S., Carlet, J., Cosgrove, S., Goossens, H., Holmes, A., Jarlier, V., Voss, A., and Pittet, D. 2013. Antimicrobial resistance: a global view from the 2013 World Healthcare-Associated Infections Forum. Antimicrob Resist Infect Control. 2:31.

Imanishi, Y., Yang, L., Sokal, I., Filipek, S., Palczewski, K., and Baehr, W. 2004. Diversity of guanylate cyclase-activating proteins (GCAPs) in teleost fish: characterization of three novel GCAPs (GCAP4, GCAP5, GCAP7) from zebrafish (Danio rerio) and prediction of eight GCAPs (GCAP1-8) in pufferfish (Fugu rubripes). J Mol Evol. 59:204–17.

Järver, P., Mäger, I., and Langel, Ü. 2010. In vivo biodistribution and efficacy of peptide mediated delivery. Trends Pharmacol Sci. 31:528–35.

Jen, W.C., Jones, G.A., Brewer, D., Parkinson, V.O., and Taylor, A. 1987. The antibacterial activity of alamethicins and zervamicins. J Appl Bacteriol. 63:293–8.

Joliot, A., Pernelle, C., Deagostini-Bazin, H., and Prochiantz, A. 1991. Antennapedia homeobox peptide regulates neural morphogenesis. Proc Natl Acad Sci. 88:1864–1868.

Juliano, R., Alam, M.R., Dixit, V., and Kang, H. 2008. Mechanisms and strategies for effective delivery of antisense and siRNA oligonucleotides. Nucleic Acids Res. 36:4158–71.

Kalfa, V.C., Jia, H.P., Kunkle, R.A., McCray, P.B., Tack, B.F., and Brogden, K.A. 2001. Congeners of SMAP29 kill ovine pathogens and induce ultrastructural damage in bacterial cells. Antimicrob Agents Chemother. 45:3256–61.

Kaltofen, S., Li, C., Huang, P.-S., Serpell, L.C., Barth, A., and André, I. 2014. Computational de novo design of a self-assembling peptide with predefined structure. J Mol Biol. 427:550–62.

Kaplan, I.M., Wadia, J.S., and Dowdy, S.F. 2005. Cationic TAT peptide transduction domain enters cells by macropinocytosis. J Control Release. 102:247–53.

Kawamura, K.S., Sung, M., Bolewska-Pedyczak, E., and Gariépy, J. 2006. Probing the impact of valency on the routing of arginine-rich peptides into eukaryotic cells. Biochemistry. 45:1116–27.

Kawamura, S., and Tachibanaki, S. 2008. Rod and cone photoreceptors: molecular basis of the difference in their physiology. Comp Biochem Physiol A Mol Integr Physiol. 150:369–77.

Kersemans, V., Kersemans, K., and Cornelissen, B. 2008. Cell Penetrating Peptides for In Vivo Molecular Imaging Applications. Curr Pharm Des. 14:2415–2427.

Killian, J.A. 1992. Gramicidin and gramicidin-lipid interactions. Biochim Biophys Acta. 1113:391–425.

Kimmel, C.B. 1993. Patterning the brain of the zebrafish embryo. Annu Rev Neurosci. 16:707–32.

Koch, K.-W. 2013. The guanylate cyclase signaling system in zebrafish photoreceptors. FEBS Lett. 587:2055–9.

Koch, K.W., and Stryer, L. 1988. Highly cooperative feedback control of retinal rod guanylate cyclase by calcium ions. Nature. 334:64–6.

Kumar, S., Harrison, N., Richards-Kortum, R., and Sokolov, K. 2007. Plasmonic nanosensors for imaging intracellular biomarkers in live cells. Nano Lett. 7:1338–43.

Lamb, T.D. 2013. Evolution of phototransduction, vertebrate photoreceptors and retina. Prog Retin Eye Res. 36:52–119.

Lamb, T.D., and Pugh, E.N. 2004. Dark adaptation and the retinoid cycle of vision. Prog Retin Eye Res. 23:307–80.

Lee, J., and Lee, D.G. 2014. Antimicrobial Peptides (AMPs) with Dual Mechanisms: Membrane Disruption and Apoptosis. J Microbiol Biotechnol.

Lee, Y.-J., Datta, S., and Pellois, J.-P. 2008. Real-time fluorescence detection of protein transduction into live cells. J Am Chem Soc. 130:2398–9.

Lee, Y.-J., Johnson, G., Peltier, G.C., and Pellois, J.-P. 2011. A HA2-Fusion tag limits the endosomal release of its protein cargo despite causing endosomal lysis. Biochim Biophys Acta. 1810:752–8.

Leskov, I.B., Klenchin, V.A., Handy, J.W., Whitlock, G.G., Govardovskii, V.I., Bownds, M.D., Lamb, T.D., Pugh, E.N., and Arshavsky, V.Y. 2000. The gain of rod phototransduction: reconciliation of biochemical and electrophysiological measurements. Neuron. 27:525–37.

Li, X.-Z., and Nikaido, H. 2004. Efflux-mediated drug resistance in bacteria. Drugs. 64:159–204.

Liebman, P.A., and Granda, A.M. 1971. Microspectrophotometric measurements of visual pigments in two species of turtle, Pseudemys scripta and Chelonia mydas. Vision Res. 11:105–14.

Lindgren, M., Hällbrink, M., Prochiantz, A., and Langel, Ü. 2000. Cell-penetrating peptides. Trends Pharmacol Sci. 21:99–103.

Lolley, R.N., and Racz, E. 1982. Calcium modulation of cyclic GMP synthesis in rat visual cells. Vision Res. 22:1481–6.

Ludtke, S.J., He, K., Heller, W.T., Harroun, T.A., Yang, L., and Huang, H.W. 1996. Membrane pores induced by magainin. Biochemistry. 35:13723–8.

Lundberg, P., Andaloussi, S. El, Sütlü, T., Johansson, H., and Langel, Ü. 2007. Delivery of short interfering RNA using endosomolytic cell-penetrating peptides. FASEB J. 21:2664–71.

Lundin, P., Johansson, H., Guterstam, P., Holm, T., Hansen, M., Langel, Ü., and Andaloussi, S. El. 2008. Distinct uptake routes of cell-penetrating peptide conjugates. Bioconjug Chem. 19:2535–42.

Maccari, G., Luca, M. Di, and Nifosí, R. 2013. Antimicrobial peptides design by evolutionary multiobjective optimization. PLoS Comput …. 9:e1003212.

Maccari, G., Luca, M. Di, and Nifosì, R. 2015. In silico design of antimicrobial peptides. Methods Mol Biol. 1268:195–219.

MacLeod, D.I. 1972. Rods cancel cones in flicker. Nature. 235:173–4.

Madan, V., Sánchez-Martínez, S., Vedovato, N., Rispoli, G., Carrasco, L., and Nieva, J.L. 2007. Plasma membrane-porating domain in poliovirus 2B protein. A short peptide mimics viroporin activity. J Mol Biol. 374:951–64.

Mäe, M., and Langel, Ü. 2006. Cell-penetrating peptides as vectors for peptide, protein and oligonucleotide delivery. Curr Opin Pharmacol. 6:509–14.

Maiolo, J.R., Ferrer, M., and Ottinger, E.A. 2005. Effects of cargo molecules on the cellular uptake of arginine-rich cell-penetrating peptides. Biochim Biophys Acta. 1712:161–72.

Maiolo, J.R., Ottinger, E.A., and Ferrer, M. 2004. Specific redistribution of cell-penetrating peptides from endosomes to the cytoplasm and nucleus upon laser illumination. J Am Chem Soc. 126:15376–7.

Mallick, S., and Choi, J.S. 2014. Liposomes: versatile and biocompatible nanovesicles for efficient biomolecules delivery. J Nanosci Nanotechnol. 14:755–65.

Marion, D., Zasloff, M., and Bax, A. 1988. A two-dimensional NMR study of the antimicrobial peptide magainin 2. FEBS Lett. 227:21–6.

Marsh, D. 1996. Peptide models for membrane channels. Biochem J. 361:345–361.

Masland, R.H. 2012. The neuronal organization of the retina. Neuron. 76:266–80.

Mathew, M.K., and Balaram, P. 1983. Alamethicin and related membrane channel forming polypeptides. Mol Cell Biochem. 50:47–64.

Mathias, R.T., Cohen, I.S., and Oliva, C. 1990. Limitations of the whole cell patch clamp technique in the control of intracellular concentrations. Biophys J. 58:759–70.

Matsuzaki, K., Murase, O., Fujii, N., and Miyajima, K. 1996. An antimicrobial peptide, magainin 2, induced rapid flip-flop of phospholipids coupled with pore formation and peptide translocation. Biochemistry. 35:11361–8.

Mayor, S., and Pagano, R.E. 2007. Pathways of clathrin-independent endocytosis. Nat Rev Mol Cell Biol. 8:603–12.

Meade, B.R., and Dowdy, S.F. 2007. Exogenous siRNA delivery using peptide transduction domains/cell penetrating peptides. Adv Drug Deliv Rev. 59:134–40.

Mendez, A., and Chen, J. 2002. Mouse models to study GCAP functions in intact photoreceptors. Adv Exp Med Biol. 514:361–88.

Meyer, C.E., and Reusser, F. 1967. A polypeptide antibacterial agent isolated from Trichoderma viride. Experientia. 23:85–6.

Milani, A., Benedusi, M., Aquila, M., and Rispoli, G. 2009. Pore forming properties of cecropin-melittin hybrid peptide in a natural membrane. Molecules. 14:5179–5188.

Molle, G., Dugast, J.Y., Spach, G., and Duclohier, H. 1996. Ion channel stabilization of synthetic alamethicin analogs by rings of inter-helix H-bonds. Biophys J. 70:1669–75.

Morris, M.C., Depollier, J., Mery, Heitz, F., and Divita, G. 2001. A peptide carrier for the delivery of biologically active proteins into mammalian cells. Nat Biotechnol. 19:1173–6.

Münst, B., Patsch, C., and Edenhofer, F. 2009. Engineering cell-permeable protein. J Vis Exp.

Nakase, I., Hirose, H., Tanaka, G., Tadokoro, A., Kobayashi, S., Takeuchi, T., and Futaki, S. 2009. Cell-surface accumulation of flock house virus-derived peptide leads to efficient internalization via macropinocytosis. Mol Ther. 17:1868–76.

Nakatani, K., Chen, C., Yau, K.-W., and Koutalos, Y. 2002. Calcium and phototransduction. Adv Exp Med Biol. 514:1–20.

Neher, E., and Sakmann, B. 1976. Single-channel currents recorded from membrane of denervated frog muscle fibres. Nature. 260:799–802.

Neher, E., Sakmann, B., and Steinbach, J.H. 1978. The extracellular patch clamp: a method for resolving currents through individual open channels in biological membranes. Pflugers Arch. 375:219–28.

Noshiro, D., Asami, K., and Futaki, S. 2010. Metal-assisted channel stabilization: disposition of a single histidine on the N-terminus of alamethicin yields channels with extraordinarily long lifetimes. Biophys J. 98:1801–8.

Oehlke, J., Scheller, A., Wiesner, B., Krause, E., Beyermann, M., Klauschenz, E., Melzig, M., and Bienert, M. 1998. Cellular uptake of an alpha-helical amphipathic model peptide with the potential to deliver polar compounds into the cell interior non-endocytically. Biochim Biophys Acta. 1414:127–39.

Oliveira, S., Fretz, M.M., Høgset, A., Storm, G., and Schiffelers, R.M. 2007. Photochemical internalization enhances silencing of epidermal growth factor receptor through improved endosomal escape of siRNA. Biochim Biophys Acta. 1768:1211–7.

Orioni, B., Bocchinfuso, G., Kim, J.Y., Palleschi, A., Grande, G., Bobone, S., Park, Y., Kim, J. Il, Hahm, K., and Stella, L. 2009. Membrane perturbation by the antimicrobial peptide PMAP-23: a fluorescence and molecular dynamics study. Biochim Biophys Acta. 1788:1523–33.

Palczewski, K., Subbaraya, I., Gorczyca, W.A., Helekar, B.S., Ruiz, C.C., Ohguro, H., Huang, J., Zhao, X., Crabb, J.W., and Johnson, R.S. 1994. Molecular cloning and characterization of retinal photoreceptor guanylyl cyclase-activating protein. Neuron. 13:395–404.

Papo, N., and Shai, Y. 2005. Host defense peptides as new weapons in cancer treatment. Cell Mol Life Sci. 62:784–90.

Piantavigna, S., McCubbin, G. a, Boehnke, S., Graham, B., Spiccia, L., and Martin, L.L. 2011. A mechanistic investigation of cell-penetrating Tat peptides with supported lipid membranes. Biochim Biophys Acta. 1808:1811–7.

Pistolesi, S., Pogni, R., and Feix, J.B. 2007. Membrane insertion and bilayer perturbation by antimicrobial peptide CM15. Biophys J. 93:1651–1660.

Pooga, Hällbrink, M., Zorko, M., and Langel, Ü. 1998. Cell penetration by transportan. FASEB J. 12:67–77.

Pugh, E.N., and Lamb, T.D. 2000. Phototransduction in vertebrate rods and cones: Molecular mechanisms of amplification, recovery and light adaptation. Handb Biol Phys. 3:183–255.

Rätscho, N., Scholten, A., and Koch, K.-W. 2009. Expression profiles of three novel sensory guanylate cyclases and guanylate cyclase-activating proteins in the zebrafish retina. Biochim Biophys Acta. 1793:1110–4.

Reddy, K.V.R., Yedery, R.D., and Aranha, C. 2004. Antimicrobial peptides: premises and promises. Int J Antimicrob Agents. 24:536–47.

Reusser, F. 1967. Biosynthesis of antibiotic U-22,324, a cyclic polypeptide. J Biol Chem. 242:243–7.

Richard, J.P., Melikov, K., Brooks, H., Prevot, P., Lebleu, B., and Chernomordik, L. V. 2005. Cellular uptake of unconjugated TAT peptide involves clathrin-dependent endocytosis and heparan sulfate receptors. J Biol Chem. 280:15300–6.

Richard, J.P., Melikov, K., Vivès, E., Ramos, C., Verbeure, B., Gait, M.J., Chernomordik, L. V, and Lebleu, B. 2003. Cell-penetrating peptides. A reevaluation of the mechanism of cellular uptake. J Biol Chem. 278:585–90.

Rispoli, G. 1998. Calcium regulation of phototransduction in vertebrate rod outer segments. J Photochem Photobiol B Biol. 44:1–20.

Robinson, J., Schmitt, E.A., Hárosi, F.I., Reece, R.J., and Dowling, J.E. 1993. Zebrafish ultraviolet visual pigment: absorption spectrum, sequence, and localization. Proc Natl Acad Sci U S A. 90:6009–12.

Rossolini, G.M., Arena, F., Pecile, P., and Pollini, S. 2014. Update on the antibiotic resistance crisis. Curr Opin Pharmacol. 18C:56–60.

Rudolph, C., Schillinger, U., Ortiz, A., Tabatt, K., Plank, C., Müller, R.H., and Rosenecker, J. 2004. Application of novel solid lipid nanoparticle (SLN)-gene vector formulations based on a dimeric HIV-1 TAT-peptide in vitro and in vivo. Pharm Res. 21:1662–9.

Salomone, F., Cardarelli, F., and Luca, M. Di. 2012. A novel chimeric cell-penetrating peptide with membrane-disruptive properties for efficient endosomal escape. J Control Release. 163:293–303.

Salomone, F., Cardarelli, F., Signore, G., Boccardi, C., and Beltram, F. 2013. In vitro efficient transfection by CM_{18}-Tat_{11} hybrid peptide: a new tool for gene-delivery applications. PLoS One. 8:e70108.

Sarantis, M., Everett, K., and Attwell, D. 1988. A presynaptic action of glutamate at the cone output synapse. Nature. 332:451–3.

Schmid, S., Fuchs, R., Kielian, M., Helenius, A., and Mellman, I. 1989. Acidification of endosome subpopulations in wild-type Chinese hamster ovary cells and temperature-sensitive acidification-defective mutants. J Cell Biol. 108:1291–300.

Scholten, A., and Koch, K.-W. 2011. Differential calcium signaling by cone specific guanylate cyclase-activating proteins from the zebrafish retina. PLoS One. 6:e23117.

Schwarze, S.R., Ho, A., Vocero-Akbani, A., and Dowdy, S.F. 1999. In vivo protein transduction: delivery of a biologically active protein into the mouse. Science (80-). 285:1569–72.

Schweizer, F. 2009. Cationic amphiphilic peptides with cancer-selective toxicity. Eur J Pharmacol. 625:190–4.

Serresi, M., Bizzarri, R., Cardarelli, F., and Beltram, F. 2009. Real-time measurement of endosomal acidification by a novel genetically encoded biosensor. Anal Bioanal Chem. 393:1123–33.

Sheldon, K., Liu, D., Ferguson, J., and Gariépy, J. 1995. Loligomers: design of de novo peptide-based intracellular vehicles. Proc Natl Acad Sci U S A. 92:2056–60.

Sherry, D.M., Bui, D.D., and Degrip, W.J. 1998. Identification and distribution of photoreceptor subtypes in the neotenic tiger salamander retina. Vis Neurosci. 15:1175–87.

Simeoni, F., Morris, M.C., Heitz, F., and Divita, G. 2003. Insight into the mechanism of the peptide-based gene delivery system MPG: implications for delivery of siRNA into mammalian cells. Nucleic Acids Res. 31:2717–24.

Skarnes, R.C., and Watson, D.W. 1957. Antimicrobial factors of normal tissues and fluids. Bacteriol Rev. 21:273–94.

Skehel, J.J., Cross, K., Steinhauer, D., and Wiley, D.C. 2001. Influenza fusion peptides. Biochem Soc Trans. 29:623–6.

Snyder, E.L., and Dowdy, S.F. 2005. Recent advances in the use of protein transduction domains for the delivery of peptides, proteins and nucleic acids in vivo. Expert Opin Drug Deliv. 2:43–51.

Steinberg, R.H., Fisher, S.K., and Anderson, D.H. 1980. Disc morphogenesis in vertebrate photoreceptors. J Comp Neurol. 190:501–8.

Steiner, H., Hultmark, D., Engström, A., Bennich, H., and Boman, G. 1981. Sequence and specificity of two antibacterial proteins involved in insect immunity. Nature. 292:246–8.

Stephen, R., Bereta, G., Golczak, M., Palczewski, K., and Sousa, M.C. 2007. Stabilizing function for myristoyl group revealed by the crystal structure of a neuronal calcium sensor, guanylate cyclase-activating protein 1. Structure. 15:1392–402.

Stewart, K.M., Horton, K.L., and Kelley, S.O. 2008. Cell-penetrating peptides as delivery vehicles for biology and medicine. Org Biomol Chem. 6:2242–55.

Suarez-Carmona, M., Hubert, P., Delvenne, P., and Herfs, M. 2014. Defensins: "Simple" antimicrobial peptides or broad-spectrum molecules?. Cytokine Growth Factor Rev.

Subbaraya, I., Ruiz, C.C., Helekar, B.S., Zhao, X., Gorczyca, W.A., Pettenati, M.J., Rao, P.N., Palczewski, K., and Baehr, W. 1994. Molecular characterization of human and mouse photoreceptor guanylate cyclase-activating protein (GCAP) and chromosomal localization of the human gene. J Biol Chem. 269:31080–9.

Suzuki, T., Futaki, S., Niwa, M., Tanaka, S., Ueda, K., and Sugiura, Y. 2002. Possible existence of common internalization mechanisms among arginine-rich peptides. J Biol Chem. 277:2437–43.

Swanson, J.A., and Watts, C. 1995. Macropinocytosis. Trends Cell Biol. 5:424–8.

Takemoto, N., Tachibanaki, S., and Kawamura, S. 2009. High cGMP synthetic activity in carp cones. Proc Natl Acad Sci U S A. 106:11788–93.

Tünnemann, G., Martin, R.M., Haupt, S., Patsch, C., Edenhofer, F., and Cardoso, M.C. 2006. Cargo-dependent mode of uptake and bioavailability of TAT-containing proteins and peptides in living cells. FASEB J. 20:1775–84.

Tünnemann, G., Ter-Avetisyan, G., Martin, R.M., Stöckl, M., Herrmann, A., and Cardoso, M.C. 2008. Live-cell analysis of cell penetration ability and toxicity of oligo-arginines. J Pept Sci. 14:469–76.

Vedovato, N., Baldini, C., Toniolo, C., and Rispoli, G. 2007. Pore-forming properties of alamethicin F50/5 inserted in a biological membrane. Chem Biodivers. 4:1338–46.

Vedovato, N., and Rispoli, G. 2007. A novel technique to study pore-forming peptides in a natural membrane. Eur Biophys J. 36:771–8.

Veldhoen, S., Laufer, S.D., Trampe, A., and Restle, T. 2006. Cellular delivery of small interfering RNA by a non-covalently attached cell-penetrating peptide: quantitative analysis of uptake and biological effect. Nucleic Acids Res. 34:6561–73.

Vivès, E., Brodin, P., and Lebleu, B. 1997. A truncated HIV-1 Tat protein basic domain rapidly translocates through the plasma membrane and accumulates in the cell nucleus. J Biol Chem. 272:16010–7.

Wade, D., Andreu, D., Mitchell, S.A., Silveira, A.M., Boman, A., Boman, H.G., and Merrifield, R.B. 1992. Antibacterial peptides designed as analogs or hybrids of cecropins and melittin. Int J Pept Protein Res. 40:429–36.

Wadia, J.S., Stan, R. V, and Dowdy, S.F. 2004. Transducible TAT-HA fusogenic peptide enhances escape of TAT-fusion proteins after lipid raft macropinocytosis. Nat Med. 10:310–5.

Wallace, D.P., Tomich, J.M., Eppler, J.W., Iwamoto, T., Grantham, J.J., and Sullivan, L.P. 2000. A synthetic channel-forming peptide induces Cl(-) secretion: modulation by Ca(2+)-dependent K(+) channels. Biochim Biophys Acta. 1464:69–82.

Wang, Z., and Wang, G. 2004. APD: the Antimicrobial Peptide Database. Nucleic Acids Res. 32:D590–2.

Wilde, A.A.M. 2008. Channelopathies in children and adults. Pacing Clin Electrophysiol. 31 Suppl 1:S41–5.

Wilson, D.N. 2014. Ribosome-targeting antibiotics and mechanisms of bacterial resistance. Nat Rev Microbiol. 12:35–48.

Wright, G.D. 2005. Bacterial resistance to antibiotics: enzymatic degradation and modification. Adv Drug Deliv Rev. 57:1451–70.

Yau, K.W., and Nakatani, K. 1984. Electrogenic Na-Ca exchange in retinal rod outer segment. Nature. 311:661–663.

Yau, K.W., and Nakatani, K. 1985a. Light-induced reduction of cytoplasmic free calcium in retinal rod outer segment. Nature. 313:579–82.

Yau, K.W., and Nakatani, K. 1985b. Light-suppressible, cyclic GMP-sensitive conductance in the plasma membrane of a truncated rod outer segment. Nature. 317:252–255.

Yenugu, S., Hamil, K.G., French, F.S., and Hall, S.H. 2004. Antimicrobial actions of the human epididymis 2 (HE2) protein isoforms, HE2alpha, HE2beta1 and HE2beta2. Reprod Biol Endocrinol. 2:61.

Young, R.W. 1967. The renewal of photoreceptor cell outer segments. J Cell Biol. 33:61–72.

Young, R.W. 1971. The renewal of rod and cone outer segments in the rhesus monkey. J Cell Biol. 49:303–18.

Zasloff, M. 2002. Antimicrobial peptides of multicellular organisms. Nature. 415:389–95.

Zhao, J.-F., Chen, J.-Y., Mi, L., Wang, P.-N., and Peng, Q. 2011. Enhancement of intracellular delivery of anti-cancer drugs by the Tat peptide. Ultrastruct Pathol. 35:119–23.

Zorko, M., and Langel, Ü. 2005. Cell-penetrating peptides: mechanism and kinetics of cargo delivery. Adv Drug Deliv Rev. 57:529–45.

Zuckerman, R. 1973. Ionic analysis of photoreceptor membrane currents. J Physiol. 235:333–54.